CWP-437
December 2002

Fluid Substitution Theories and Multicomponent Seismic Characterization of Fractured Reservoirs

Reynaldo Cardona

— Doctoral Thesis —

Geophysics

Center for Wave Phenomena
Colorado School of Mines
Golden, Colorado 80401
303 273-3557

ABSTRACT

This work studies fluid substitution processes in anisotropic rocks and their influence on the elastic modeling and characterization of naturally fractured reservoirs. The results indicate that the linear slip theory may incur errors when modeling the anisotropic parameters of *fluid-saturated* rocks under conditions of equilibrated pore pressures. The errors originate from the fact that the total storage capacity of the pore system does not allow the decomposition of the rock's compliance tensor as formulated in the linear slip theory.

The concept of the total storage capacity links the theories of fluid substitution to the theory of pressure-transient experiments performed by well-test engineers. In elastically isotropic reservoirs, storage capacity estimates from pressure-transient data can be used directly in Gassmann's (1951) equations to predict the changes in the rock's bulk modulus with saturation. In fractured reservoirs, estimates of the ratio of the fracture- to total-storage capacity can be used to constrain the normal compliance of the fracture system estimated from seismic data.

When fluid substitution occurs in rocks with fractures of complex rheology the velocity of vertically propagating shear-waves may be dependent on fluid saturation. The shear-wave sensitivity to fluids originates from the effective symmetry of the rock, which has to be monoclinic or lower for vertical fractures. Analysis of time-lapse, multicomponent data acquired over a reservoir under CO_2 injection at Weyburn field, Canada, suggests there is a time-lapse variation of the shear splitting in areas where large amounts of CO_2 are injected. Furthermore, those areas coincide with zones in the reservoir that have symmetry lower than orthorhombic.

TABLE OF CONTENTS

NOTATION

"If you must analyze more than two phenomena in a single manuscript, make sure to add the hebrew alphabet to your notation"
Andrey A. Clondaro, 1994

$c \equiv$ compressibility
$C_{ij} \equiv$ stiffness matrix
$C \equiv$ wellbore storage
$D \equiv$ fluid influence factor
$\Delta_N \equiv$ normal weakness
$\Delta_T \equiv$ tangential weakness
$E \equiv$ Young's Modulus
$G \equiv$ shear modulus
$K \equiv$ bulk modulus
$\kappa \equiv$ permeability
$\mu \equiv$ viscosity
$L \equiv$ length
$M \equiv$ P-wave modulus
$p \equiv$ pressure
$q \equiv$ flow rate
$r \equiv$ radius
$s \equiv$ skin factor
$S_{ij} \equiv$ compliance matrix
$S_{ijkl} \equiv$ compliance matrix
$t \equiv$ time
$\theta \equiv$ crack dip
$v \equiv$ volume
$V_P \equiv$ P-wave velocity
$V_{S1} \equiv$ fast S-wave velocity
$V_{S2} \equiv$ slow S-wave velocity
$Z \equiv$ fracture compliance
$\alpha_c \equiv$ crack aspect ratio
$\beta \equiv$ NMO ellipse rotation
$\varepsilon_{ij} \equiv$ strain
$\phi \equiv$ porosity
$\Phi \equiv$ relative crack azimuth
$\lambda \equiv$ well-test parameter
$\eta_c \equiv$ crack/fracture density

$\nu \equiv$ Poisson's ratio
$\rho \equiv$ fluid density
$\sigma \equiv$ stress
$\omega \equiv$ storage capacity ratio

Subscripts
b bulk
c crack
d dry
f fluid
F fracture
i isotropic
s saturated
m mineral
p pore
w wellbore

ACKNOWLEDGMENTS

This work has benefited from my interaction with a large number of people that I wish to thank in this section. First of all, I am greatly indebted to my advisor Dr. Thomas Davis for his support and guidance during my Ph.D. studies. I am equally grateful to Dr. Ilya Tsvankin who has influenced my work and furthered my understanding of elastic anisotropy. Tom and Ilya gave me the opportunity to be a member of both the Center for Wave Phenomena (CWP) and the Reservoir Characterization Project (RCP), which has been an excellent learning experience.

I would like to acknowledge the guidance I received from my committee members: Dr. Michael Batzle, Dr. Neil Hurley and Dr. Erdal Ozkan. Mike has been a constant source of rock physics knowledge, insight and humor. To Neil I am grateful for my better understanding of carbonate geology and for his keen editorial corrections that have improved considerably some of my papers. I thank Erdal for helping me understand the links between geophysical and well-test methods.

I would like to express my gratitude to Dr. Vladimir Grechka, who always found time to answer my questions, and to Dr. Robert Benson for his help debugging the program for polarization analysis.

I have benefited from discussions with several students of the RCP and the members of the A(nisotropy)-team, especially: Marty Terrell, Luca Duranti, Gwenola Michaud, Ed Jenner, Andres Pech and Vinicio Sanchez. Marty has been my officemate for almost four years and I am thankful for all his corrections and suggestions that improved the quality of this thesis.

I would also like to acknowledge the help I have received from Kasper Van Wijk, Barbara McLenon, Andres Pech and Barbara Brockman who were instrumental for the successful formating and printing of this thesis.

My largest "thank you" goes to my beautiful wife, Silvana. Silvana brought me to Colorado giving me the opportunity to come to the Colorado School of Mines. I have always had her unconditional support, and when I was struggling with the final stages of this thesis, she worked, studied and took care of me, all at the same time. It would have been impossible to finish my studies without Silvana by my side.

Finally, I thank my parents and brother for motivating me to pursue my Ph.D. degree and supporting me throughout all my studies. I owe them much more than what could be written in just a few lines.

Para Silvana, Ricardo, Graciela y Raul

Chapter 1

INTRODUCTION

1.1 Motivation

Characterization of fractured reservoirs is an important area of research due to its economical impact. A large portion of the oil and natural gas in the world is trapped in tight reservoirs that require large permeabilities provided by natural fractures to produce reservoir fluids economically (Nelson, 1985). If the fractures have preferential orientation, the reservoir becomes anisotropic with respect to wave propagation, and by characterizing the seismic anisotropy we can obtain information about the properties of the fracture network.

The location of fluid migration paths through the fracture network is one of the most important inferences geophycisists hope to draw from seismic data. This can be achieved through the use of time-lapse seismic, in which several seismic experiments are performed with the intention of monitoring changes in the seismic signatures that are associated with fluid migration. Therefore, fractured reservoir characterization requires accurate theoretical descriptions of how the seismic signatures should be parameterized, and how the parameterization changes with variations in the reservoir fluids.

This thesis deals with several theoretical and practical issues regarding the characterization of fractured reservoirs in the "static" case, where no time-lapse data is available, and in the "dynamic" case, where a time-lapse experiment has been acquired. The topics addressed in each chapter have been motivated by the ongoing Weyburn field characterization project, in which a fractured carbonate reservoir under CO_2 injection is being monitored using multicomponent seismic data. Although each topic is applicable to Weyburn field, the implications of the results are valid for fractured reservoir characterization in general.

1.2 Thesis Layout

The thesis has been written to minimize cross-referencing between chapters. Hence, the chapters are as self-contained as possible allowing the reader to understand the results without having to read the whole manuscript. The first three chapters of the thesis are aimed at clarifying and improving our theoretical understanding of the fluid substitution process in elastically anisotropic rocks.

Chapter 2 develops from first principles two of the most common fluid substitution theories used in the rock physics community: the static-limit theory that results in Gassmann's (1951) and Brown and Korringa's (1975) formulations, and the squirt-limit theory that results in Mukerji and Mavko's (1994) formulation . This chapter is not just a review of facts already found in the literature, but rather an interpretation of the fundamental link that exists between the two formulations. Chapter 2 also clarifies some common misconceptions about the application and use of Gassmann's equation.

In Chapter 3, I show that the linear-slip parameterization of fractured rocks does not hold for all conditions of fluid saturation. The use of the linear-slip parameterization is suitable to calculate the compliances of saturated rocks in the high-frequency "squirt" limit, but may be in error for low frequency measurements.

Chapter 4 addresses the possibility of having shear-wave moduli and velocities that are sensitive to changes in the compressibility of the reservoir fluids. The implications of the chapter is that time-lapse analysis of shear-waves may be used in monitoring fluid movement in the reservoir and that the existence of time-lapse variation may help constrain the symmetry of the reservoir rocks.

Due to the complexities of naturally fractured rocks, the reservoir geophycisist is always in need of independent sources of information that can help him or her constrain the estimates derived from seismic data. A largely overlooked source of information lies in the results of pressure-transient analyses performed by reservoir engineers. Chapter 5 develops a theory that relates the estimates from pressure-transient tests to the normal compliance of the fracture network at the well location.

Chapters 6 and 7 are dedicated to a case study of fracture reservoir characterization at Weyburn field, Saskatchewan, Canada. Several of the concepts introduced in previous chapters are applied to the seismic characterization of the fractured reservoir. The results show that, in the survey area, the reservoir is divided in two major zones where the fractured rocks have different elastic properties. The "static" characterization and the time-lapse results suggest that the fracture network has a lower symmetry and is probably more complex in the southern part of the survey.

1.3 Weyburn Overview

Here a brief overview of Weyburn field and the enhanced recovery project will be given. A detailed geological background of Weyburn field and the Williston Basin can be found in Bunge (2000).

Weyburn field is located in the northern part of the Williston basin at Saskatchewan, Canada. The field produces from the fractured Midale beds of the Mississippian Charles Formation (Madison Group) at a depth of 1300 to 1500 meters (see Figure 1.1). The Midale beds are divided into an upper Marly zone and a lower Vuggy

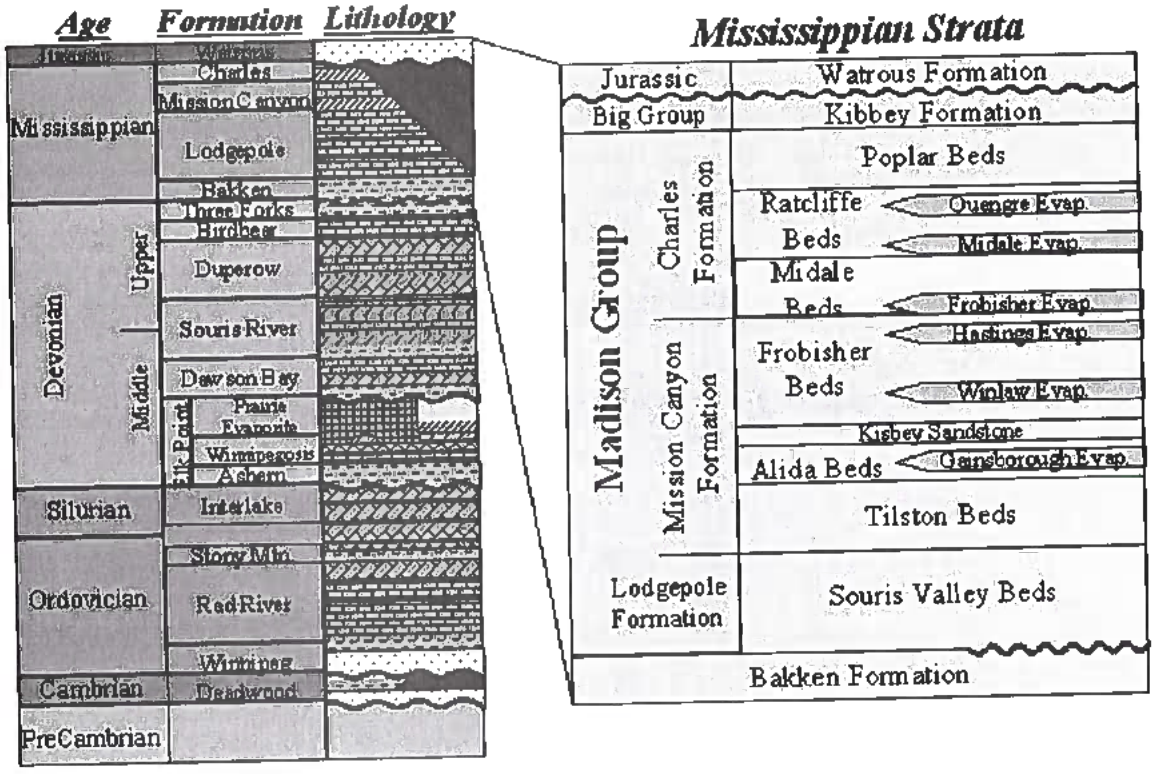

FIG. 1.1. Stratigraphic column indicating the Mississippian section and the reservoir highlighted in yellow.

zone. The Marly zone has high porosity but low permeability, whereas the Vuggy zone tends to have higher permeability and lower porosity. Hence, the Vuggy has been swept more extensively and it is expected that the Marly zone contains significant bypassed reserves.

The field produced under primary depletion until production peaked in 1964, when water flooding was initiated. Horizontal drilling began in 1991. Out of the estimated 1.1 billion barrels of oil in place, only 24% has been recovered after 46 years of production.

To increase production and improve the sweep of bypassed zones in the Marly interval, a large CO_2 injection project started in the year 2000. In the same year the Reservoir Characterization Project at the Colorado School of Mines started a time-lapse, nine-component seismic project that consisted on the acquisition of compressional, converted, and pure shear-waves from three surveys acquired on October 2000, October 2001 and October 2002, respectively. The case study presented in Chapters 6 and 7 analyzes the 2000 and 2001 surveys.

The importance of monitoring the injection process at Weyburn field is that there are at least two different fracture sets in the reservoir that may provide a direct pathway between injectors and producers. Because the objective of the CO_2 injection is to sweep zones of by-passed oil, if the CO_2 encounters a direct pathway to the producers the injection process will lose efficiency.

Chapter 2

THE LINK BETWEEN STATIC- AND SQUIRT-LIMIT FLUID SUBSTITUTION

2.1 Introduction

Fluid substitution theories address the problem of how to calculate changes in the compliance of a rock with changes in the compressibility of the fluid that fills its pores. Two of the most common classes of theories used in the rock physics community lie at opposite ends of practical application. The first class consists of theories that assume that the stresses applied to the rock are of a frequency low enough to allow pressure equilibrium throughout the pore space, and are called *static* limit theories. The second class assumes that the stresses are applied at a frequency high enough that fluids in pores of different shape are *not* allowed to equilibrate pressures among each other, and are called *squirt* limit theories.

Even though the two classes of theories defined above lie at opposite ends of the "frequency spectrum", they have much more in common than what would be expected from the extreme cases they treat. The detailed analysis presented below shows that in fact these are "sister" theories that avoid dealing with the problem of viscous flow in exactly the same manner. The similarities in the derivation of each theory results in final formulations that have similar forms, albeit yield different predictions. It is important to emphasize that when I say that the squirt-limit avoids the viscous flow problem I mean that in the high-frequency range the applied stresses cycle so fast that the fluids in narrow pores are *not* allowed to move at all.

The rock physics enthusiast is well aware that one of the major hurdles to overcome when comparing different fluid substitution formulations is literature with different notations and derivations. Hence, the objective of this chapter is to derive the fluid substitution theories in the high- and low-frequency limits under a single notation and formalism that highlights the similarities and differences between them. The derivations shown below borrow from the work and notations by Zimmerman (1991), Brown and Korringa (1975) and Mukerji and Mavko (1994) for the case of monomineralic rocks. Even though Brown and Korringa (1975) also developed a theory for multimineralic rocks, that formulation will not be considered in this thesis.

The reader will notice that the detailed derivations presented below would normally be found in appendices. However, in this case the similarities and differences between the theories are understood better when the whole formulation is laid out in

the main text. In all other chapters in this thesis, extensive derivations are relegated to appendices.

2.2 The Preamble to the Static and Squirt-limits

Let us assume that a rock can be described by a bounding surface that defines the bulk of the rock and by internal surfaces that define the pores in the rock. Let us also assume that we have a rock in which a general confining stress (σ^c_{kl}) and a pore stress (σ^p_{kl}) are applied to the outside and inside surface of the rock, respectively. Because there are two volumes in the rock (bulk and pore), two *average* volume strains can be defined as ε^b_{ij} and ε^p_{ij}, where the superscripts "b" and "p" refer to the bulk and pore volumes, respectively.

Because there are two different volume strains and two stresses applied to the rock, one can define four different compliance tensors as:

$$S^{bc}_{ijkl} \equiv -\left[\frac{\partial \varepsilon^b_{ij}}{\partial \sigma^c_{kl}}\right]_{\sigma^p}, \tag{2.1}$$

$$S^{bp}_{ijkl} \equiv \left[\frac{\partial \varepsilon^b_{ij}}{\partial \sigma^p_{kl}}\right]_{\sigma^c}, \tag{2.2}$$

$$S^{pc}_{ijkl} \equiv -\left[\frac{\partial \varepsilon^p_{ij}}{\partial \sigma^c_{kl}}\right]_{\sigma^p}, \tag{2.3}$$

$$S^{pp}_{ijkl} \equiv \left[\frac{\partial \varepsilon^p_{ij}}{\partial \sigma^p_{kl}}\right]_{\sigma^c}. \tag{2.4}$$

In this notation, the first superscript refers to the volume strain (bulk or pore) and the second superscript refers to the stress (confining or pore). Note that the sign convention in equations (2.1)-(2.4) is chosen such that a *positive confining stress* results in a volume contraction and a *negative strain*; whereas a *positive pore stress* results in a volume expansion and a *positive strain*. Hence, the negative signs in equations (2.1) and (2.3) assure that the volume compressibilities are positive.

Up to this point, and until further notice, the confining and pore stresses are considered as mathematically independent variables [this mathematical condition holds for "drained" conditions in which the confining stress does not induce changes in the pore stress (Zimmerman, 1991)]. Hence, an increment in the bulk and pore strains can be written as:

$$d\varepsilon^b_{ij} = \left[\frac{\partial \varepsilon^b_{ij}}{\partial \sigma^c_{kl}}\right]_{\sigma^p} d\sigma^c_{kl} + \left[\frac{\partial \varepsilon^b_{ij}}{\partial \sigma^p_{kl}}\right]_{\sigma^c} d\sigma^p_{kl}, \tag{2.5}$$

$$d\varepsilon_{ij}^{p} = \left[\frac{\partial \varepsilon_{ij}^{p}}{\partial \sigma_{kl}^{c}}\right]_{\sigma^{p}} d\sigma_{kl}^{c} + \left[\frac{\partial \varepsilon_{ij}^{p}}{\partial \sigma_{kl}^{p}}\right]_{\sigma^{c}} d\sigma_{kl}^{p}. \tag{2.6}$$

Then, using the definitions (2.1)-(2.4) we get:

$$d\varepsilon_{ij}^{b} = -S_{ijkl}^{bc} d\sigma_{kl}^{c} + S_{ijkl}^{bp} d\sigma_{kl}^{p}, \tag{2.7}$$

$$d\varepsilon_{ij}^{p} = -S_{ijkl}^{pc} d\sigma_{kl}^{c} + S_{ijkl}^{pp} d\sigma_{kl}^{p}. \tag{2.8}$$

Note that up to this point the differential pore stress is completely general and it may exert normal as well as tangential tractions of the pore walls. If we *assume* that the pore content is a fluid that exerts a hydrostatic pressure on the pore wall then the pore stress is:

$$d\sigma_{kl}^{p} = \delta_{kk} dp_{f} \tag{2.9}$$

where dp_f is the fluid pressure increment. Substituting (2.9) into equations (2.7) and (2.8) results in:

$$d\varepsilon_{ij}^{b} = -S_{ijkl}^{bc} d\sigma_{kl}^{c} + S_{ijkk}^{bp} dp_{f}, \tag{2.10}$$

$$d\varepsilon_{ij}^{p} = -S_{ijkl}^{pc} d\sigma_{kl}^{c} + S_{ijkk}^{pp} dp_{f}. \tag{2.11}$$

Expressions (2.10) and (2.11) can be called the *drained* equations of the porous rock because the fluid pressure (dp_f) is a variable independent of the applied confining stress ($d\sigma_{kl}^{c}$). If the rock is "undrained" and the fluids are trapped within the rock such that the fluid volume in the pore system is constant, we start dealing with the problem of fluid-saturated rocks.

In the "undrained" or fluid-saturated case, we assume we know the applied confining stress and that three unknowns remain: dp_f, $d\varepsilon_{ij}^{b}$ and $d\varepsilon_{ij}^{p}$. Because we have only equations (2.10) and (2.11) to work with, we need a *third* equation to solve for all three unknowns. The introduction of this third equation marks the crossroads that leads to the static theory of fluid substitution on one path and to the high frequency, squirt theory on the other.

The reason for the crossroads is that, at this point, we need to find an equation that relates the fluid pressure increment (dp_f) to the pore strain ($d\varepsilon_{ij}$); and we would like to do this avoiding the complications of viscous fluid flow. Two different approaches make the problem tractable. The first approach assumes that:
1) all the pore space is connected and 100% fluid-saturated
2) the experiment is static to ensure that there is *a single* fluid pressure throughout the whole pore space and that viscous fluid flow is not an issue.
This set of assumptions leads to Gassmann's (1951) and Brown and Korringa's (1975) static or "low frequency" results.

The second approach assumes that:
1) the experiment is done at frequencies high enough that the fluid in the narrowest

portions of the pore space will be trapped, unable to squirt out to more ample neighboring pores
2) the fluid entrapment results in different induced fluid pressures in pores of different "thinness"
3) all the pore space can be divided in subsets of pores with equal induced fluid pressure and equal strains.
This set of assumptions leads to the isolated crack models, which include Mukerji and Mavko's as the most general, and also Hudson's (1981) and Thomsen's (1995) high-frequency solutions, among others.

Notice that both approaches avoid the viscous flow problem by "pigeonholing" fluids into sets of pores with equal induced pressure, where in the simpler static case the whole pore space corresponds to a single set. It will be shown below that this similarity in the strategy of both approaches results in static and high-frequency formulations that are much more similar in the form of the resulting equations than what would be expected from the extreme cases they treat.

2.3 The Static limit

Following the first set of assumptions described above for the static limit, the pore volume (v_p) is equal to the fluid volume (v_f). Hence the pore volume strain can be written as:

$$\frac{dv_p}{v_p} = \frac{dv_f}{v_f} = -c_f dp_f, \tag{2.12}$$

where c_f is the fluid compressibility. Because by definition the volume strain is the double index contraction of the pore strain ($d\varepsilon_{ij}$), the third equation needed to solve the fluid substitution problem is:

$$d\varepsilon^p_{\alpha\alpha} = -c_f dp_f. \tag{2.13}$$

Doing the double index contraction of the pore strain in equation (2.11) and substituting that strain into equation (2.13) one can solve for the fluid pressure increment (dp_f) as

$$dp_f = \left[\frac{S^{pc}_{\alpha\alpha kl}}{c_f + S^{pp}_{\alpha\alpha\beta\beta}}\right] d\sigma^c_{kl}. \tag{2.14}$$

Note that $S^{pp}_{\alpha\alpha\beta\beta}$ is a scalar that represents the compressibility of the pore volume to a variation of the pore pressure. Hence the denominator of the term between straight brackets is the *total pore space compressibility* that is related to the *fluid storage capacity* of the rock, which is a parameter reservoir engineers use and estimate routinely (see Chapter 5).

The bulk strain of the saturated rock can be calculated substituting equation (2.14)

in the equation (2.10) where one gets

$$d\varepsilon_{ij}^{b,sat} = \left[-S_{ijkl}^{bc} + \frac{S_{\alpha\alpha ij}^{bp} S_{\alpha\alpha kl}^{pc}}{c_f + S_{\alpha\alpha\beta\beta}^{pp}} \right] d\sigma_{kl}^{c}. \tag{2.15}$$

Because in the fluid-saturated rock the only independent variable is the confining stress, from equation (2.15) we get

$$S_{ijkl}^{b,sat} \equiv -\frac{\partial \varepsilon_{ij}^{b,sat}}{\partial \sigma_{kl}^{c}} = -\frac{d\varepsilon_{ij}^{b,sat}}{d\sigma_{kl}^{c}} = S_{ijkl}^{bc} - \frac{S_{\alpha\alpha ij}^{bp} S_{\alpha\alpha kl}^{pc}}{c_f + S_{\alpha\alpha\beta\beta}^{pp}}. \tag{2.16}$$

From the definition of the compliance tensors (2.1)-(2.4) we see that $S_{\alpha\alpha kl}^{bc}$ is the compliance that relates the application of a confining stress at *constant* pore pressure to the resulting bulk strain. Therefore $S_{\alpha\alpha kl}^{bc}$ is the compliance of the *dry* rock, and from expression (2.16) we can finally write the equation for the change in the bulk compliance with saturation as:

$$S_{ijkl}^{b,dry} - S_{ijkl}^{b,sat} = \frac{S_{\alpha\alpha ij}^{bp} S_{\alpha\alpha kl}^{pc}}{c_f + S_{\alpha\alpha\beta\beta}^{pp}}. \tag{2.17}$$

Note that an important piece of information equation (2.17) provides is that the change in the bulk compliance with saturation is inversely proportional to the total pore space compressibility $c_f + S_{\alpha\alpha\beta\beta}^{pp}$. Therefore, substitution of a low compressibility fluid will generate a larger change in the compliance than the substitution of a very compressible fluid.

The final expression that results in Brown and Korringa's and Gassmann's equations requires that the compliances $S_{\alpha\alpha ij}^{bp}$, $S_{\alpha\alpha kl}^{pc}$ and $S_{\alpha\alpha\beta\beta}^{pp}$ be expressed as a function of the compliances of the dry rock and the mineral material. This can be achieved using the following three equations

$$\phi S_{ijkl}^{pc} = S_{ijkl}^{b,dry} - S_{ijkl}^{m}, \tag{2.18}$$

$$\phi S_{ijkl}^{pc} = S_{ijkl}^{bp}, \tag{2.19}$$

$$\phi S_{ijkl}^{pp} = S_{ijkl}^{bp} - \phi S_{ijkl}^{m}, \tag{2.20}$$

where S_{ijkl}^{m} is the compliance of the mineral material and ϕ is the porosity of the rock. Equations (2.18)-(2.20) are derived from the application of the Betti-Rayleigh reciprocity theorem (Walsh, 1965) in the same way Zimmerman (1991) did it to find equivalent expressions for the volume compressibilities. From equations (2.18)-(2.20) is straightforward to prove the pore space compressibility ($S_{\alpha\alpha\beta\beta}^{pp}$) in the denominator

of equation (2.17) is

$$S^{pp}_{\alpha\alpha\beta\beta} = \frac{S^{b,dry}_{\alpha\alpha\beta\beta} - S^{m}_{\alpha\alpha\beta\beta}}{\phi} - S^{m}_{\alpha\alpha\beta\beta}. \tag{2.21}$$

Finally, substituting equations (2.18), (2.19) and (2.21) into equation (2.17) we obtain Brown and Korringa's (1975) monomineralic equation:

$$S^{b,dry}_{ijkl} - S^{b,sat}_{ijkl} = \frac{(S^{b,dry}_{ij\alpha\alpha} - S^{m}_{ij\alpha\alpha})(S^{b,dry}_{kl\alpha\alpha} - S^{m}_{kl\alpha\alpha})}{(S^{b,dry}_{\alpha\alpha\beta\beta} - S^{m}_{\alpha\alpha\beta\beta}) + (c_f - S^{m}_{\alpha\alpha\beta\beta})\phi}, \tag{2.22}$$

Note that all the compliances in the denominator of equation (2.22) have double contracted indices and, therefore, are scalars that represent the bulk compressibilities of the mineral and the dry rock.

Gassmann's equation is obtained directly from Brown and Korringa's through the double contraction of the indices ij and kl. Because the bulk moduli of the rock are the inverse of the compressibilities, Brown and Korringa's equation transforms into Gassmann's equation as:

$$\frac{1}{K_{dry}} - \frac{1}{K_{sat}} = \frac{\left(\frac{1}{K_{dry}} - \frac{1}{K_{sat}}\right)^2}{\left(\frac{1}{K_{dry}} - \frac{1}{K_m}\right) + \left(\frac{1}{K_f} - \frac{1}{K_m}\right)\phi}. \tag{2.23}$$

At this point is important to rectify the common misconception that Gassmann's equation for the compressibility cannot be used for anisotropic rocks. Equation (2.22) and (2.23) make it obvious that Gassmann's equation for the bulk modulus is as valid as Brown and Korringa's. The caveat is that if the rock is anisotropic, Gassmann's equation becomes less useful because knowing how the bulk modulus changes with saturation is not enough to characterize the change of the whole compliance tensor.

The bulk compressibility of an anisotropic rock can always be defined as:

$$1/K_{sat} = S^{sat}_{\alpha\alpha\beta\beta}, \tag{2.24}$$

and its change with saturation will be determined by the Gassmann equation. However, the isotropic predictions for changes with saturation of the *shear moduli* of the rock will not always hold for anisotropic rocks.

2.4 The squirt-limit

To calculate the saturated compliance in the squirt-limit we assume that the high frequencies have effectively *isolated* some of the pores in the rock and the fluid substitution is done in two steps. The first step consists in estimating the change in

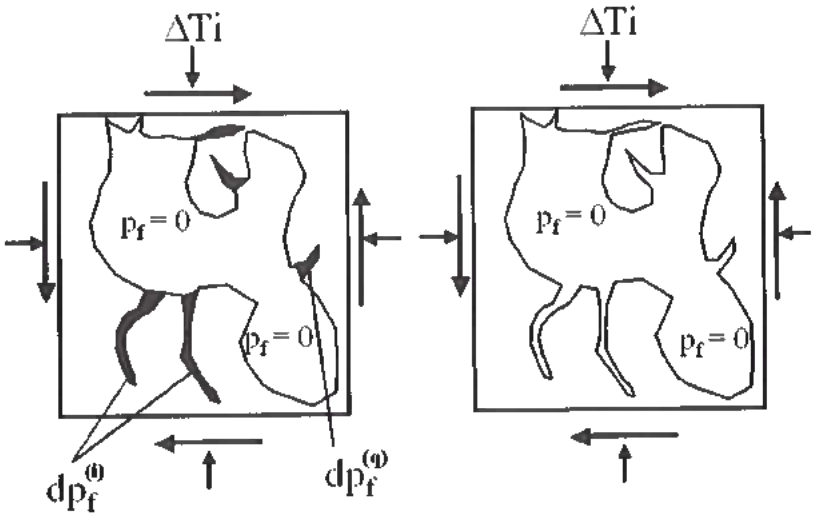

FIG. 2.1. Schematic representation of a rock subjected to two sets of tractions for the application of the reciprocity theorem (Mukerji and Mavko, 1994).

the bulk compliance due to the fluid trapped in the "thin" pores. Then the more ample pores that are not trapped can be substituted using Brown and Korringa's equation. Therefore, the treatment assumes that to all practical purposes the trapped fluids become part of the frame.

Figure 2.1 shows a schematic description of the problem. While the rock to the right is dry the rock to the left has fluids in the narrowest isolated pores, and the fluid exerts a pressure in those pores only. Application of the reciprocity theorem to both rocks gives a relation between the compliance of the dry rock and the compliance of the rock with the trapped fluids, which Mukerji and Mavko called "unrelaxed" frame compliance. Both rocks on Figure 2.1 have loads (ΔT_i) applied to the external surface. Because the rock on the right is dry it will deforms according to the dry compliance. However, the rock to the left also has internal pressures applied that are, up to this point, unknown. The reciprocity theorem states that the tractions of the rock on the left acting through the displacements of the rock on the right, will do the same work than the tractions of the right acting through the displacements on the left. Hence, using the dry compliance (S^{dry}_{ijkl}) and the unrelaxed frame compliance (S^{ur}_{ijkl}) we can write,

$$\underbrace{d\sigma^c_{ij}n_j}_{\Delta T_i}\underbrace{S^{dry}_{ijkl}d\sigma^c_{kl}v_b}_{\Delta U_{i,dry}} - \sum_n dp^{(n)}_f S^{pc,(n)}_{\alpha\alpha kl} d\sigma^c_{kl} v^{(n)}_p = \underbrace{d\sigma^c_{ij}n_j}_{\Delta T_i}\underbrace{S^{ur}_{ijkl}d\sigma^c_{kl}v_b}_{\Delta U_{i,ur}}, \tag{2.25}$$

where v_b is the bulk volume, $d\sigma^c_{ij}$ is the applied confining stress, and n_j are the normals to the surfaces. Note that the summations in the second term of the left side of the equation come from separating the isolated pores into several sets that have equal induced pore pressure. Hence, $v_p^{(n)}$, $p_f^{(n)}$ and $S^{pc,(n)}_{\alpha\alpha kl}$ are the volume, fluid pressure increment and compliance of the n-th set of the isolated pores (Mukerji and Mavko, 1994). Rearranging the terms of equation (2.25) one can obtain

$$S^{dry}_{ijkl} - S^{ur}_{ijkl} = \sum_n \phi^{(n)} S^{pc(n)}_{\alpha\alpha kl} \frac{dp_f^{(n)}}{d\sigma^c_{ij}} \tag{2.26}$$

At this point, it is necessary to substitute the ratio of the induced fluid pressure to the applied confining stress of the n-th pore in equation (2.26). Because it has been assumed that the fluid pressure increment is constant in each of the sets, we can use the ratio $dp_f^{(n)}/d\sigma^c_{ij}$ that has already been calculate for the static case [see equation (2.14)]. Therefore, we can substitute equation (2.14) into equation (2.26) to obtain

$$S^{dry}_{ijkl} - S^{ur}_{ijkl} = \sum_n \phi^{(n)} \frac{S^{pc,(n)}_{\alpha\alpha ij} S^{pc,(n)}_{\alpha\alpha kl}}{c_f + S^{pp}_{\alpha\alpha\beta\beta}}, \tag{2.27}$$

which is the equation presented by Mukerji and Mavko (1994).

2.5 Discussion

Now it is possible to observe the similarity between the static- and squirt-limit equations. If we copy the static limit equation (2.26) and make use of the fact that $\phi S^{pc}_{ijkl} = S^{bp}_{ijkl}$, then the static limit equation takes the form:

$$S^{b,dry}_{ijkl} - S^{b,sat}_{ijkl} = \phi \frac{S^{pc}_{\alpha\alpha ij} S^{pc}_{\alpha\alpha kl}}{c_f + S^{pp}_{\alpha\alpha\beta\beta}}. \tag{2.28}$$

Comparison of the right hand side of equations (2.27) and (2.28) shows they are identical for a given set of pores. Furthermore, we see that if the rock is composed by a *single set* of pores, the change between the dry and the "unrelaxed" compliance or the dry and saturated compliance is *identical*. Thomsen (1995) came to the same conclusion in his theory of fluid substitution in rocks with penny shaped cracks (see Chapter 3). However, the observation from equations (2.27) and (2.28) is much more general than Thomsen's because in the derivation presented above there is no restriction on the symmetry of the rock or the shape of the pores.

Finally, equations (2.27) and (2.28) show that in cases in which there are several isolated pores with different shapes or orientations, the change in the compliances is larger for the squirt-limit than the static limit. This is a well known effect that is

predicted by all theories of isolated cracks including Hudson's (1981) and Thomsen's (1995)

These results show that the fundamental link between the static- and squirt-limit is that both theories make the fluid substitution problem tractable by dividing the pore space into subsets of equal induced fluid pressure. Hence, both theories can be described under the same theoretical framework. These formulations will be used in several of the following chapters as tools for the characterization of fractured reservoirs and time-lapse monitoring.

Chapter 3

FLUID SUBSTITUTION IN POROUS ROCKS WITH ALIGNED CRACKS

3.1 Introduction

Knowledge of the correct theory for fluid substitution in anisotropic rocks is important for monitoring fluid migration in fractured reservoirs. The simplest model of fractured rocks is one in which vertical, penny-shaped (rotationally invariant) parallel fractures are embedded in an elastically isotropic background resulting in a transversely isotropic rock with a horizontal symmetry axis (HTI). This model will be treated in this chapter to analyze and compare three different fluid substitution theories .

Several different effective medium theories give equivalent descriptions of the elasticity of *dry* HTI rocks (O'Connell and Budiansky, 1974; Hudson, 1981; Schoenberg and Douma, 1988). For example, assuming non-interacting fractures, Hudson's (1981) model of aligned penny-shaped cracks is equivalent to the linear slip model of infinite parallel planes (Bakulin et al., 2000a). However, when the rock is fluid-saturated, predictions from different theories vary depending on the assumptions made about the pore space connectivity, fluid viscosity and the frequency of the applied stress.

Thomsen (1995) studied how the anisotropic parameters of a porous rock with aligned penny-shaped cracks vary with changes in the bulk modulus of the saturating fluid. He proved that the theory for saturated cracks developed by Hudson (1981) is only valid when the cracks are isolated from fluid flow, as in the case of crystalline rocks with negligible primary porosity. Under those conditions, a passing wave induces a large fluid pressure increase in the hydraulically disconnected cracks resulting in large changes in the anisotropic parameters with saturation. However, Thomsen argues that a correct theory for fluid substitution in fractured sedimentary rocks has to take into account the fluid pressure equilibration that takes place between hydraulically connected cracks and non-fracture pores. Hence, he proposes two formulations for the changes of the anisotropic parameters with saturation. The first is valid in the limit of slowly varying stresses (low frequency limit), in which pore fluid pressures are allowed to equilibrate. The second is valid in the limit of rapidly varying stresses ("moderately high-frequency" limit), in which cracks are effectively isolated from fluid flow.

One of the appealing features of Thomsen's (1995) work is that the elastic com-

pliance of the fractured rock has the same form for the dry and fluid-saturated cases, and for both frequency limits. If his formulation is correct, the linear slip model that can be used for dry rocks is also applicable to fluid-saturated rocks [Bakulin et al. (2000a)]. However, the work presented in this chapter suggests that Thomsen's (1995) calculation of the saturated rock compliance does not take into account the full effect of pressure equalization; and that the form of the dry rock compliance is different from the saturated rock compliance. Hence, use of linear slip theory is not always valid for fluid-saturated rocks, especially for those with large amounts of non-fracture porosity.

To support the point made in the previous paragraph, I compare Thomsen's formulation for idealized penny-shaped crack models with two more general theories of fluid substitution developed by Brown and Korringa (1975) and Mukerji and Mavko (1994), respectively. In contrast with Thomsen's (1995) work, these two theories make no assumptions about the strength of the anisotropy or the symmetry of the rock, nor they require information about the shape of the fractures. The result of the comparison between theories is that in the "moderately high frequency" limit Thomsen's formulation is equivalent to the more general theory developed by Mukerji and Mavko (1994). In the low frequency limit, however, the incomplete treatment of the pressure equalization in Thomsen's work results in predictions that differ from those obtained from the Brown and Korringa's formulation for rocks with high non-fracture porosity.

Brown and Korringa's theory is applicable at the low-frequency limit mentioned above. It assumes the rock is 100% fluid-saturated and that when the rock is stressed, either by a static load or a passing wave, the fluid pressure is equilibrated throughout the pore space. The latter condition can be satisfied in at least three cases:
1. There is a single pore of arbitrary shape in the rock.
2. The rock has a collection of disconnected pores with the *same* shape and orientation.
3. All pores, with arbitrary shape and orientation, are well connected and the fluid viscosity and frequency of the applied stresses are low enough to allow equilibration of any pressure differences.

In the first case, the pressure equilibration is trivial because there is only one pore in the rock. In the second case, the fluid pressure increase is the same everywhere because the pore strains are identical due to the equal shape and orientation of the pores. Case 2 would correspond to a rock with aligned penny-shaped cracks and no isotropic background porosity (e.g. cracked granite), and case 3 is the one most applicable to fractured sedimentary rocks.

Mukerji and Mavko's theory (called "anisotropic squirt theory"), is applicable at the "moderately high-frequency" limit stated by Thomsen (1995). This formulation recognizes that when rapidly varying stresses are applied to a saturated fractured

rock, fluids in the narrowest pores are isolated from flow from the rest of the pore space. The fluid pressure will be larger in the isolated pores, and the pressure gradient through the pore space results in a rock that is stiffer than the one obtained from a fluid substitution under low-frequency conditions. The term "moderately high" is meant to indicate that even though the frequency of a passing wave is high enough to generate pressure gradients in the pore space, the fracture dimensions are still much smaller than a wavelength.

In the following sections I start by describing Thomsen's (1995) formulation using the linear slip notation for both the low-frequency and "moderately high-frequency" limits. Next, I obtain the analytical expressions for the saturated compliances predicted by the more general theories developed by Brown and Korringa (1975) and Mukerji and Mavko (1994) and highlight the discrepancies with Thomsen's formulation in the low-frequency limit. Finally, the predictions from the different theories will be compared numerically for two models with different isotropic background properties; one modeled as a dilute collection of spherical pores and the other with the elastic properties of Weyburn field reservoir rocks.

3.2 Review of Thomsen's Model and the Linear Slip Model

The effective compliance of a fractured rock with non-interacting, rotationally invariant fractures can be obtained from two equivalent models: the *linear-slip* model and *penny-shaped crack* model. In linear slip theory fractures are treated, regardless of their shape or microstructure, as planes of weakness with non-welded boundary conditions (Schoenberg and Douma, 1988; Schoenberg and Sayers, 1995). When the fractures are embedded in an otherwise isotropic background, the effective compliance matrix ($\mathbf{S}$) is given by

$$\mathbf{S} = \mathbf{S}_B + \mathbf{S}_F, \tag{3.1}$$

where $\mathbf{S}_B$ is the compliance matrix of the isotropic background rock and $\mathbf{S}_F$ is the excess compliance associated with the fractures. Since the background rock is unfractured and isotropic, $\mathbf{S}_B$ can be written in terms of the Young's modulus (E), the shear modulus (G) and the Poisson's ratio (ν) of the background as

$$\mathbf{S}_B = \begin{pmatrix} \frac{1}{E} & -\frac{\nu}{E} & -\frac{\nu}{E} & 0 & 0 & 0 \\ -\frac{\nu}{E} & \frac{1}{E} & -\frac{\nu}{E} & 0 & 0 & 0 \\ -\frac{\nu}{E} & -\frac{\nu}{E} & \frac{1}{E} & 0 & 0 & 0 \\ 0 & 0 & 0 & \frac{1}{G} & 0 & 0 \\ 0 & 0 & 0 & 0 & \frac{1}{G} & 0 \\ 0 & 0 & 0 & 0 & 0 & \frac{1}{G} \end{pmatrix}. \tag{3.2}$$

When fractures are embedded in the isotropic background, the rock becomes

more compliant to stresses applied in certain directions. These direction are determined by the fracture type and orientation, and the excess compliance the fractures contribute is described by the non-zero elements of the ($\mathbf{S}_F$) matrix. If the fractures have a rotationally invariant microstructure (like penny-shaped cracks) and their normals are parallel to the X_1 direction, the excess fracture compliance is given by:

$$\mathbf{S}_F = \begin{pmatrix} Z_N & 0 & 0 & 0 & 0 & 0 \\ 0 & 0 & 0 & 0 & 0 & 0 \\ 0 & 0 & 0 & 0 & 0 & 0 \\ 0 & 0 & 0 & 0 & 0 & 0 \\ 0 & 0 & 0 & 0 & Z_T & 0 \\ 0 & 0 & 0 & 0 & 0 & Z_T \end{pmatrix}. \tag{3.3}$$

Here Z_N is the excess normal compliance that relates the fracture-normal displacements to the normal stresses applied to the fracture in the X_1 direction and Z_T is the excess tangential compliance that relates tangential displacements and stresses in the X_2 and X_3 directions.

Notice that equation (3.3) from linear slip theory does not include details about the microstructure of the fractures other than the fact that they are rotationally invariant. All information about fracture shape is implicit in the terms Z_N and Z_T. In contrast, penny-shaped crack models give explicit expressions for the excess compliance contributed by the fractures (Hudson, 1981; Schoenberg and Douma, 1988; Bakulin et al., 2000a).

"Penny-shaped" cracks are oblate spheroids characterized by their aspect ratios (α_c), defined as the ratio of the crack aperture (b) divided by the crack radius (a). The contribution of the cracks to the compliance of the rock depends on the crack density defined as $\eta_c = Na^3/V$, where N is the number of cracks and V is the total sample volume. In Appendix A it is shown that in a *dry* rock with vertical cracks the normal and tangential fracture compliances are, to first order in the crack density:

$$Z_N^d = \frac{16}{3}\frac{1}{E_d}\left(1-\nu_d^2\right)\eta_c, \tag{3.4}$$

and

$$Z_T^d = \frac{16}{3}\frac{1}{G_d}\left(\frac{1-\nu_d}{2-\nu_d}\right)\eta_c, \tag{3.5}$$

where E_d, G_d and ν_d are the Young's modulus, shear modulus and Poisson's ratio of the dry background isotropic rock, respectively. Thomsen (1995) obtained equivalent expressions for the case of penny-shaped cracks with normals in the X_3 direction [his equations (A26a)-(A28) when the fluid bulk modulus is set to zero]. Later, Bakulin et al. (2000a) derived equivalent expressions for the normal (Δ_N) and tangential (Δ_T)

fracture weaknesses, which are parameters that can be obtained from Z_N^d and Z_T^d as

$$\Delta_N \equiv \frac{Z_N M}{1 + Z_N M}, \tag{3.6}$$

and

$$\Delta_T \equiv \frac{Z_T G}{1 + Z_T G}. \tag{3.7}$$

where M is the P-wave modulus of the background rock.

Adding the dry background compliance and the excess fracture compliance, the effective compliance of the dry rock ($\mathbf{S}^d$) is given by:

$$\mathbf{S}^d = \begin{pmatrix} \frac{1}{E_d} + Z_N^d & -\frac{\nu_d}{E_d} & -\frac{\nu_d}{E_d} & 0 & 0 & 0 \\ -\frac{\nu_d}{E_d} & \frac{1}{E_d} & -\frac{\nu_d}{E_d} & 0 & 0 & 0 \\ -\frac{\nu_d}{E_d} & -\frac{\nu_d}{E_d} & \frac{1}{E_d} & 0 & 0 & 0 \\ 0 & 0 & 0 & \frac{1}{G} & 0 & 0 \\ 0 & 0 & 0 & 0 & \frac{1}{G} + Z_T^d & 0 \\ 0 & 0 & 0 & 0 & 0 & \frac{1}{G} + Z_T^d \end{pmatrix}. \tag{3.8}$$

Thomsen (1995) derived the compliance matrix of a fluid-saturated rock ($\mathbf{S}^s$) with the *implicit* assumption that the values of the compliance terms S_{22}^s, S_{33}^s and S_{12}^s, S_{13}^s, and S_{23}^s were identical to those on the fluid-saturated isotropic background (it will be shown below that this assumption is not well justified in the presence of equilibrated pore pressures in the rock). Hence, Thomsen's effective compliance of the saturated rock is given by:

$$\mathbf{S}^s = \begin{pmatrix} \frac{1}{E_s} + Z_N^s & -\frac{\nu_s}{E_s} & -\frac{\nu_s}{E_s} & 0 & 0 & 0 \\ -\frac{\nu_s}{E_s} & \frac{1}{E_s} & -\frac{\nu_s}{E_s} & 0 & 0 & 0 \\ -\frac{\nu_s}{E_s} & -\frac{\nu_s}{E_s} & \frac{1}{E_s} & 0 & 0 & 0 \\ 0 & 0 & 0 & \frac{1}{G} & 0 & 0 \\ 0 & 0 & 0 & 0 & \frac{1}{G} + Z_T^s & 0 \\ 0 & 0 & 0 & 0 & 0 & \frac{1}{G} + Z_T^s \end{pmatrix}, \tag{3.9}$$

where E_s and ν_s are the Young's modulus and Poisson's ratio of the fluid-saturated background, and Z_N^s and Z_T^s are the saturated normal and tangential fracture compliances. No distinction is made between the dry and saturated shear modulus of the isotropic background in equations (3.8) and (3.9) because it does not change with fluid saturation.

The fluid-saturated fracture compliances in equation (3.9) can be written as:

$$Z_N^s = Z_N^d \left(1 - \frac{K_f}{K_m}\right) D_{ci}(hi, lo), \tag{3.10}$$

and

$$Z_T^s = Z_T^d, \tag{3.11}$$

where K_f and K_m are the bulk moduli of the saturating fluid and mineral material respectively (see Appendix A). $D_{ci}(hi, lo)$ is the "fluid influence factor" that accounts for the pressure equilibration between cracks and matrix pores, and (hi, lo) indicates it has different values for the moderately high- and low-frequency limits, respectively.

In the low-frequency limit the fluid influence factor is given by

$$D_{ci}(lo) = \frac{1}{1 - \frac{K_f}{K_m} + \frac{K_f}{\phi_i + \phi_c}\left(\frac{1}{K_d} - \frac{1}{K_m} + Z_N^d\right)}, \tag{3.12}$$

where ϕ_c and ϕ_i are the crack and isotropic matrix porosity, respectively, and the subscript "ci" indicates that both isotropic matrix and crack porosity are included. In the moderately high-frequency limit the fluid influence factor is

$$D_{ci}(hi) = \frac{1}{1 - \frac{K_f}{K_m} + \frac{K_f}{\phi_c} Z_N^d}. \tag{3.13}$$

Notice that the fluid influence factor for the moderately high-frequency limit $[D_{ci}(hi)]$ does *not* depend on the isotropic porosity and is identical to $D_{ci}(lo)$ for a rock with *only* crack porosity. By setting $\phi_i = 0$ and $K_m = K_d$ in equation (3.12) one obtains

$$D_{ci}(lo) = D_{ci}(hi) = D_c = \frac{1}{1 - \frac{K_f}{K_m} + \frac{K_f}{\phi_c} Z_N^d}, \tag{3.14}$$

where the subscript "c" in D_c indicates that only cracks are included. Physically, this means that in the moderately-high frequency limit the fractures are effectively isolated from flow from the rest of the pores (ϕ_i is effectively zero). The rapidly varying stresses do not allow the fluid pressures to equilibrate throughout the pore space and, therefore, the isotropic porosity (ϕ_i) does not contribute to the change in the normal fracture compliance (Z_N) with saturation.

When fluid pressure equilibrium exists, the induced pressure variation that stiffens the cracks will depend on the total connected pore volume including the isotropic porosity. Hence, in the low-frequency limit a rock with a porous background ($\phi_i \neq 0$) has a normal fracture compliance that depends *explicitly* on the isotropic matrix porosity through the fluid influence factor (3.12).

Having summarized above Thomsen's formulation it is possible now to point out where it differs from the more general theory of Brown and Korringa (1975) that will be presented below. Even though Thomsen (1995) recognized that the condition of fluid pressure equilibrium implies that the normal *fracture* compliance should depend on the *isotropic* porosity, he did not recognize that by the same argument the *isotropic* pore compliances should depend on the *fracture* porosity. This line of reasoning suggests that the description of the fluid-saturated rock's compliance matrix (3.9) is incomplete, especially for the isotropic background terms S^s_{22}, S^s_{33}, S^s_{12}, S^s_{13}, and S^s_{23}.

3.3 Low-Frequency Limit: Brown and Korringa's Theory

Brown and Korringa (1975) generalized Gassmann's (1951) work by relaxing the assumptions of isotropy and monomineralic rock. In their formulation, Gassmann's scalar equations are replaced by equations that relate the compliance tensor of the dry and saturated rock. In this chapter only Brown and Korringa's (B&K's) formulation for the monomineralic case is considered, which can be written as

$$S^s_{ijkl} = S^d_{ijkl} - \frac{\left(S^d_{ij\alpha\alpha} - S^m_{ij\alpha\alpha}\right)\left(S^d_{kl\alpha\alpha} - S^m_{kl\alpha\alpha}\right)}{(c_d - c_m) + (c_f - c_m)\phi_t}. \tag{3.15}$$

Here S^d_{ijkl} and S^s_{ijkl} are the compliances of the dry and saturated rock, S^m_{ijkl} is the compliance of the mineral material, $\phi_t = \phi_i + \phi_c$ is the total connected porosity, and c_f, c_m and c_d are the fluid, mineral and dry rock compressibilities, respectively.

In order to be consistent with the notation used to define the fracture compliances above, B&K's equations can be written in the 6x6 matrix notation. The terms with contracted indices ($S_{ij\alpha\alpha}$) in the numerator of equation (4.1) are the sums of elements of the first three rows of the 6x6 compliance matrix. Therefore, by defining ψ_k as the sum of the first three elements of the k-th column of the compliance matrix, as shown in Figure 4.1, equation (4.1) can be rewritten as:

$$S^d_{IJ} - S^s_{IJ} = \frac{(\psi^d_I - \psi^m_I)(\psi^d_J - \psi^m_J)}{(c_d - c_m) + (c_f - c_m)(\phi_i + \phi_c)}. \tag{3.16}$$

Better understanding of the fluid substitution process can be achieved by rewriting equations (4.2) as

$$S^s_{IJ} = S^d_{IJ} - \left(\psi^d_I - \psi^m_I\right)\frac{\partial p_f}{\partial \sigma}, \tag{3.17}$$

where

$$\frac{\partial p_f}{\partial \sigma} = \frac{\psi^d_J - \psi^m_J}{(c_d - c_m) + (c_f - c_m)(\phi_i + \phi_c)}. \tag{3.18}$$

$$S_{ij} = \begin{array}{c|ccc|ccc} & \psi_1 & \psi_2 & \psi_3 & \psi_4 & \psi_5 & \psi_6 \\ \hline & S_{11} & S_{12} & S_{13} & S_{14} & S_{15} & S_{16} \\ & S_{12} & S_{22} & S_{23} & S_{24} & S_{25} & S_{26} \\ & S_{13} & S_{23} & S_{33} & S_{34} & S_{35} & S_{36} \\ \hline & S_{14} & S_{24} & S_{34} & S_{44} & S_{45} & S_{46} \\ & S_{15} & S_{25} & S_{35} & S_{45} & S_{55} & S_{56} \\ & S_{16} & S_{26} & S_{36} & S_{46} & S_{56} & S_{66} \end{array}$$

FIG. 3.1. Compliance matrix of general symmetry indicating elements that contribute to the sums ψ_k in equation (4.2).

Here $\partial p_f/\partial\sigma$ is the gradient of the fluid pressure (p_f) induced by the variation of the confining stress ($\Delta\sigma$) (Brown and Korringa, 1975).

If the rock pores are empty ($c_f \to \infty$), there will be no variation in the fluid pressure when a differential confining stress ($\Delta\sigma$) is applied. Hence, the term $\partial p_f/\partial\sigma$ in equation (3.18) is zero and the saturated compliance (S^s_{ijkl}) is equal to the dry compliance (S^d_{ijkl}). When the rock is fluid-saturated, the confining stress ($\Delta\sigma$) strains the pore volume inducing a fluid pressure change equal to $\partial p_f/\partial\sigma\Delta\sigma$ that reduces the compliance of the rock [see equation (3.17)].

3.3.1 Total storage capacity and the fluid influence factor

The change in fluid pressure depends on the denominator of equation (3.18), which is defined as the total storage capacity of the pore system. The total storage capacity relates the variations in pore fluid volume to variations in fluid pressure and is defined as the product of the total porosity (ϕ_t) and the total pore system compressibility (c_t) (see Appendix B). The induced pressure is inversely proportional to $\phi_t c_t$ because a rock with a large storage capacity can accommodate the fluid displaced by the pore volume change with only a small pressure variation.

In the case of the rock with isotropic background porosity (ϕ_i) and crack porosity (ϕ_c), the total storage capacity is the sum of the storage capacities of the isotropic pores and crack pores:

$$\phi_t c_t = \phi_i c_i + \phi_c c_c. \tag{3.19}$$

Using the compliance matrix of the dry fractured rock defined in equations (3.4)-(3.8),

it can be shown that the storage capacity of the isotropic porosity and penny-shaped cracks are given by:

$$\phi_i c_i = \left(\frac{1}{K_d} - \frac{1}{K_m}\right) + \left(\frac{1}{K_f} - \frac{1}{K_m}\right)\phi_i, \tag{3.20}$$

and

$$\phi_c c_c = Z_N^d + \left(\frac{1}{K_f} - \frac{1}{K_m}\right)\phi_c, \tag{3.21}$$

respectively (Appendix B).

From equations (H.1)-(3.21) it is straightforward to prove that the inverse of the total storage capacity is:

$$\frac{1}{\phi_t c_t} = \frac{\frac{K_f}{\phi_t}}{1 - \frac{K_f}{K_m} + \frac{K_f}{\phi_i+\phi_c}\left(\frac{1}{K_d} - \frac{1}{K_m} + \frac{K_d}{K_m} Z_N^d\right)}. \tag{3.22}$$

Comparison of the previous expression to equation (3.12), indicates that the inverse of the total storage capacity is approximately proportional to low-frequency fluid influence factor, i.e.

$$\frac{1}{\phi_t c_t} \approx D_{ci}(lo)\frac{K_f}{\phi_t}. \tag{3.23}$$

The approximate proportionality results from the extra $\frac{K_d}{K_m}$ term multiplied with the dry normal compliance (Z_N^d) in equation (3.22) that is not present in the expression of the fluid influence factor. For rocks with only crack porosity ($\phi_i = 0$), $\frac{K_d}{K_m} = 1$ and the approximate expression (3.24) becomes exact:

$$\frac{1}{\phi_c c_c} = D_c\frac{K_f}{\phi_c}. \tag{3.24}$$

Hence, equations (3.23) and (3.24) indicate that the fluid influence factor can be interpreted as the inverse of the normalized pore system compressibility ($\frac{1}{K_f c_t}$) or as being inversely proportional to the storage capacity of the pore system.

3.3.2 Saturated compliance for a rock with a non-porous background

For the case of a non-porous background matrix, substitution of the dry compliance (3.8) into B&K's equations indicates that only the S_{11}^d component of the dry rock compliance varies with saturation (see Appendix C). Since the background matrix is non-porous, the change with saturation is due exclusively to the change in the

fracture normal compliance. S^s_{11} is given by:

$$S^s_{11} = \frac{1}{E_m} + Z^s_N, \tag{3.25}$$

where E_m is the mineral Young's modulus, and

$$Z^s_N = \frac{Z^d_N \left(1 - \frac{K_f}{K_m}\right)}{1 - \frac{K_f}{K_m} + \frac{K_f}{\phi_c} Z^d_N} \equiv Z^d_N \left(1 - \frac{K_f}{K_m}\right) D_c. \tag{3.26}$$

Comparing the previous expression to equation (3.10) shows that Thomsen's (1995) saturated normal fracture compliance is identical to the one obtained from B&K, for the case of a cracked rock with *no isotropic porosity*. No discrepancy appears, so far, between the theories because the difference between them stems from the treatment of the pressure equilibration between cracks and the *isotropic pores* that have not been introduced yet.

3.3.3 Saturated compliance for a rock with a porous background

In a rock with isotropic background porosity, the induced fluid pressure variation will depend on the storage capacity of both the isotropic and crack pores. Therefore, by virtue of equations (3.17) and (3.18), *all* the elements of the compliance matrix that change with saturation will depend *explicitly* on both the crack and isotropic porosity. The expressions for the compliance elements that change with saturation are given by:

$$S^s_{11} = \underbrace{\frac{1}{E_d} - \frac{\frac{1}{9}\left(\frac{\phi_i}{K_{\phi_i}}\right)^2}{\phi_t c_t}}_{\approx \frac{1}{E_s}} + \frac{\left(1 - \frac{K_f}{K_m} + \frac{K_f}{3K_{\phi_i}}\frac{\phi_i}{\phi_t}\right) Z^d_N}{\frac{K_f}{\phi_t}\left(\phi_t c_t\right)}, \tag{3.27}$$

$$S^s_{12} = S^s_{13} = \underbrace{-\frac{\nu_d}{E_d} - \frac{\frac{1}{9}\left(\frac{\phi_i}{K_{\phi_i}}\right)^2}{\phi_t c_t}}_{\approx -\frac{\nu_s}{E_s}} - \frac{\frac{K_f}{3K_{\phi_i}}\frac{\phi_i}{\phi_t} Z^d_N}{\frac{K_f}{\phi_t}\left(\phi_t c_t\right)}, \tag{3.28}$$

$$S^s_{22} = S^s_{33} = \frac{1}{E_d} - \frac{\frac{1}{9}\left(\frac{\phi_i}{K_{\phi_i}}\right)^2}{\phi_t c_t} \approx \frac{1}{E_s}, \tag{3.29}$$

$$S^s_{23} = -\frac{\nu_d}{E_d} - \frac{\frac{1}{9}\left(\frac{\phi_i}{K_{\phi_i}}\right)^2}{\phi_t c_t} \approx -\frac{\nu_s}{E_s}, \tag{3.30}$$

where $1/K_{\phi_i}$ is the compaction compressibility of the isotropic background pores (see Appendix C).

Equations (3.27)-(3.30) indicate that in general it is not possible to express the saturated compliance of a cracked rock exactly as the sum of the *saturated* isotropic background and a saturated fracture compliance. At first one could expect that, because tractions applied parallel to the cracks do not compress them, the terms S^s_{22}, S^s_{33}, S^s_{12}, S^s_{13}, and S^s_{23} should not depend explicitly on the fracture parameters Z^d_N and ϕ_c. However, this expectation disregards the connectivity between cracks and isotropic pores. For example, if a traction parallel to the cracks (σ_{22}) is applied to the rock, the isotropic pores will compress expelling fluid towards the neighboring pores. The magnitude of the induced pressure increase will depend on how much fluid the cracks can accommodate, which is a function of Z^d_N and ϕ_c.

A simplification of equations (3.27)-(3.30) can be used for rocks in which the isotropic porosity is much larger than the fracture porosity. In this limit the storage capacity of the cracks ($\phi_c c_c$) is negligible with respect to the storage capacity of isotropic pores ($\phi_i c_i$); and the terms with the symbols "$\approx$" in equations (3.27)-(3.30) approach the background's saturated values (see Appendix C). Under this approximation the compliance matrix is

$$\mathbf{S}^s \approx \begin{pmatrix} S^s_{11} & S^s_{12} & S^s_{12} & 0 & 0 & 0 \\ S^s_{12} & \frac{1}{E_s} & -\frac{\nu_s}{E_s} & 0 & 0 & 0 \\ S^s_{12} & -\frac{\nu_s}{E_s} & \frac{1}{E_s} & 0 & 0 & 0 \\ 0 & 0 & 0 & \frac{1}{G} & 0 & 0 \\ 0 & 0 & 0 & 0 & \frac{1}{G}+Z^s_T & 0 \\ 0 & 0 & 0 & 0 & 0 & \frac{1}{G}+Z^s_T \end{pmatrix}, \tag{3.31}$$

where $Z^s_T = Z^d_T$ (no approximation). In the expression above S^s_{11} and S^s_{12} are:

$$S^s_{11} \approx \frac{1}{E_s} + Z^d_N \left(1 - \frac{K_f}{K_m}\right) D_p + \underbrace{\frac{1}{3}\left(1 - \frac{K_d}{K_m}\right)\frac{K_f}{K_d \phi_i} D_p Z^d_N}_{\chi}, \tag{3.32}$$

and

$$S^s_{12} \approx -\frac{\nu_s}{E_s} - \underbrace{\frac{1}{3}\left(1 - \frac{K_d}{K_m}\right)\frac{K_f}{K_d \phi_i} D_p Z^d_N}_{\chi}, \tag{3.33}$$

where D_p is the fluid influence factor without including the storage capacity contribution of the cracks.

Equations (3.31)-(3.33) indicate that when $\phi_c << \phi_i$ the saturated compliance resulting from B&K's equations is similar, but not identical to the one obtained by Thomsen (1995) [equations (3.9)-(3.12)]. The difference is that B&K's theory predicts

an extra term, χ, in the elements S^s_{12} and S^s_{13}. Only if the rock is dry ($K_f = 0$) or in the trivial case that it is not fractured ($Z^d_N = 0$), both theories are identical.

3.4 Moderately-High Frequency Limit: Anisotropic Squirt Theory

Mukerji and Mavko (1994) developed a fluid substitution theory valid for arbitrary anisotropy in the moderately-high frequency limit. The formulation, called anisotropic squirt theory (AST), works under the assumption that the rock is 100% fluid-saturated and monomineralic.

The AST recognizes that when rapidly varying stresses are applied to the rock, the narrowest portions of the pore space (crack porosity) tend to have higher fluid pressures and are effectively isolated from the rest of the pores (isotropic porosity). Hence, AST does the fluid substitution in two parts. First, fluid is substituted *only* into the cracks ("soft pores" in Mukerji and Mavko's paper) to obtain the compliance of the "unrelaxed" rock frame. Then the "unrelaxed" compliance tensor is substituted in Brown and Korringa's equation to substitute fluids in the rest of the pores.

In AST, the compliance of the unrelaxed frame for a rock with a single set of identical cracks is given by

$$S^{ur}_{ijkl} = S^d_{ijkl} - \frac{\left(S^d_{ij\alpha\alpha} - S^{hi-p}_{ij\alpha\alpha}\right)\left(S^d_{kl\alpha\alpha} - S^{hi-p}_{kl\alpha\alpha}\right)}{(c_d - c_{hi-p}) + (c_f - c_{hi-p})\phi_{soft}}, \tag{3.34}$$

where S^d_{ijkl} is the compliance tensor of the dry fractured rock, S^{ur}_{ijkl} is the compliance tensor of the "unrelaxed" frame, and c_f and c_d are the fluid and dry fractured rock compressibilities, respectively. $S^{hi-p}_{kl\alpha\alpha}$ and c_{hi-p}, represent the dry compliance tensor and bulk compressibility that would be measured if a rock sample is subjected to very large confining pressures. The porosity ϕ_{soft} represents the amount of "soft" pores that close under the application of the large confining pressure.

Mukerji and Mavko (1994) expressed equation (3.12) as a function of $S^{hi-p}_{kl\alpha\alpha}$ because they were interested in applying it to laboratory data in which measurements of the compliance tensor with pressure were available. For the purposes of the modeling presented here, $S^{hi-p}_{kl\alpha\alpha}$ is just the compliance tensor of the dry rock *without* cracks, i.e. the compliance tensor of the dry isotropic background; and the "soft" porosity (ϕ_{soft}) is the crack porosity, ϕ_c. Taking this into consideration, equation (3.12) can be re-written in 6x6 matrix notation as

$$S^{ur}_{IJ} = S^d_{IJ} - \frac{(\psi^d_I - \psi^{d,iso}_I)(\psi^d_J - \psi^{d,iso}_J)}{(c_d - c_{d,iso}) + (c_f - c_m)\phi_c}, \tag{3.35}$$

where the ψ_k's are defined in the same way as in equation (4.2) and the superscripts

and subscripts "d,iso" indicate the properties correspond to the dry isotropic background rock.

From the definition of the ψ_k's and the fact that the compliance matrix S^d_{IJ} is the sum of the isotropic background compliance and the excess fracture compliance [equation (3.8)], it is easy to see that the only non-zero $\psi^d_k - \psi^{d,iso}_k$ corresponds to $k = 1$. Hence, the only compliance matrix element that changes from its dry value to its "unrelaxed" value is S_{11}. Substituting the fractured rock's dry compliance (3.8) and the dry isotropic background compliance (3.2) in equation (3.35), it is straight forward to prove that

$$S^{ur}_{11} = \frac{1}{E_d} + Z^d_N - \frac{{Z^d_N}^2}{Z^d_N + \left(\frac{1}{K_f} - \frac{1}{K_m}\right)\phi_c}. \tag{3.36}$$

Rearranging the terms in the previous expression one obtains

$$S^{ur}_{11} = \frac{1}{E_d} + \underbrace{Z^d_N \left(1 - \frac{K_f}{K_m}\right) D_{ci}(hi)}_{\equiv Z^{ur}_N}. \tag{3.37}$$

Finally, the compliance of the "unrelaxed" fractured rock is

$$\mathbf{S}^{ur} = \begin{pmatrix} \frac{1}{E_d} + Z^{ur}_N & -\frac{\nu_d}{E_d} & -\frac{\nu_d}{E_d} & 0 & 0 & 0 \\ -\frac{\nu_d}{E_d} & \frac{1}{E_d} & -\frac{\nu_d}{E_d} & 0 & 0 & 0 \\ -\frac{\nu_d}{E_d} & -\frac{\nu_d}{E_d} & \frac{1}{E_d} & 0 & 0 & 0 \\ 0 & 0 & 0 & \frac{1}{G} & 0 & 0 \\ 0 & 0 & 0 & 0 & \frac{1}{G} + Z^d_T & 0 \\ 0 & 0 & 0 & 0 & 0 & \frac{1}{G} + Z^d_T \end{pmatrix}, \tag{3.38}$$

where Z^{ur}_N is the second term in equation (3.37).

Comparing equation (3.38) to equations (3.9)-(3.11) we notice that the "unrelaxed" compliance matrix has the same form of the moderately high-frequency compliance proposed by Thomsen (1995). The only difference is that Thomsen directly includes the saturated values of the background compliances ($1/E_s$ and ν_s/E_s), whereas in AST $\mathbf{S}^{ur}$ is now input in B&K's equation to do the fluid substitution in the background isotropic pores. Hence, Thomsen's (1995) moderately high-frequency formulation for penny shaped cracks is equivalent to anisotropic squirt theory.

3.5 Numerical Results

In the previous two sections I have shown that Thomsen's (1995) formulation is equivalent to the anisotropic squirt theory in the moderately high-frequency limit, but *different* from Brown and Korringa's theory in the low-frequency limit. The practical question, however, is whether the discrepancies in the low-frequency regime could result in "substantial" differences in the prediction of the anisotropic parameters of the fractured rock. Because Brown and Korringa's theory is a more general treatment of fluid substitution than the one developed by Thomsen's (1995), B&K will be used as the "standard" against which Thomsen's results are tested in the following numerical examples.

Wave propagation in an HTI medium (a rock with aligned vertical penny-shaped cracks) is most conveniently described by the vertical P- and S-wave velocities and three anisotropic coefficients defined as:

$$\epsilon^{(V)} \equiv \frac{C_{11} - C_{33}}{2C_{33}}, \tag{3.39}$$

$$\delta^{(V)} \equiv \frac{(C_{13} + C_{55})^2 - (C_{33} - C_{55})^2}{2C_{33}(C_{33} - C_{55})}, \tag{3.40}$$

$$\gamma^{(V)} \equiv \frac{C_{66} - C_{44}}{2C_{44}}, \tag{3.41}$$

where C_{ij} are the elements of the 6x6 stiffness matrix (**C**) Tsvankin (1997b).

The numerical comparison between the different fluid substitution theories is done by calculating the $\epsilon^{(V)}$ and $\delta^{(V)}$ parameters as a function of the bulk modulus of the saturating fluid (K_f). Since the $\gamma^{(V)}$ coefficient does not change with saturation for HTI rocks (see Chapter 4), it is not included in this comparison.

The procedure to obtain $\epsilon^{(V)}$ vs. K_f and $\delta^{(V)}$ vs. K_f curves is as follows:
1. Model the **dry** isotropic background compliance ($\mathbf{S}_B$) for a given mineral and an isotropic porosity (ϕ_i).
2. Add the excess fracture compliances of the **dry** penny-shaped cracks ($\mathbf{S}_F$).
3. Apply a fluid substitution theory to obtain the saturated rock compliance ($\mathbf{S}^s$).
4. Invert the saturated compliance matrix to obtain the saturated stiffness matrix ($\mathbf{C}^s$).
5. Calculate $\epsilon^{(V)}$ and $\delta^{(V)}$ from the stiffness of the fluid-saturated rock ($\mathbf{C}^s$).

Figures 3.2-3.5 show $\epsilon^{(V)}$ and $\delta^{(V)}$ as a function of K_f for several combinations of isotropic porosity (ϕ_i), crack porosity (ϕ_c) and crack aspect ratio (α_c). For these figures the background isotropic rock was modeled as a collection of non-interacting spherical pores, an assumption generally valid for low isotropic porosity ($\phi_i < 0.1$).

Numerical analysis indicates that the variation of $\epsilon^{(V)}$ and $\delta^{(V)}$ with K_f for both

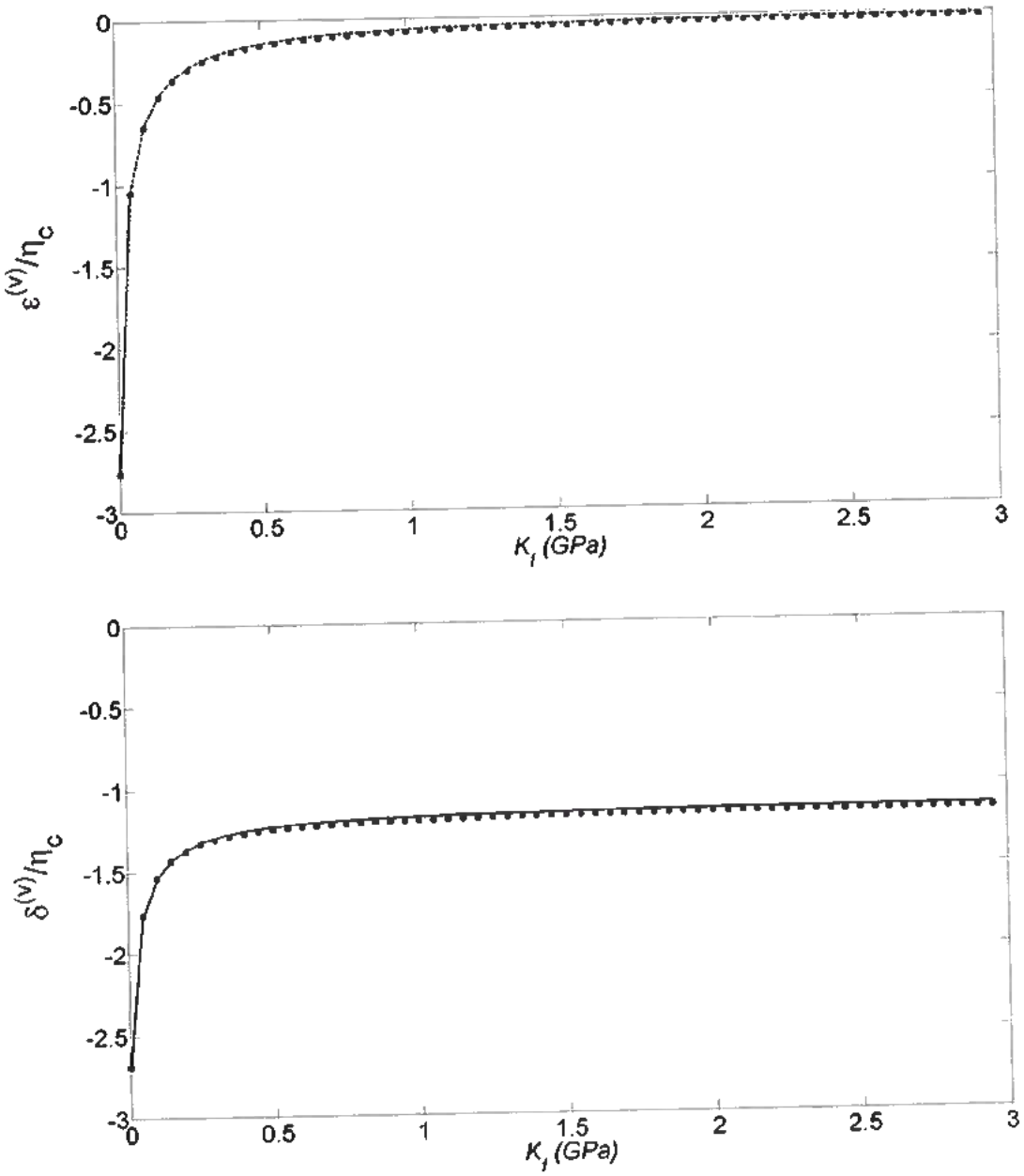

FIG. 3.2. Moderately high-frequency curves of $\epsilon^{(V)}$ and $\delta^{(V)}$ as a function of K_f for a calcite matrix with $\phi_i = 0.05$, $\phi_c = 10^{-4}$, $\eta_c = 0.05$ and $\alpha_c = 4\text{x}10^{-4}$. Note an almost perfect overlap of the predictions from Thomsen's (squares), Hudson's (1981) (crosses) and AST's (dotted line).

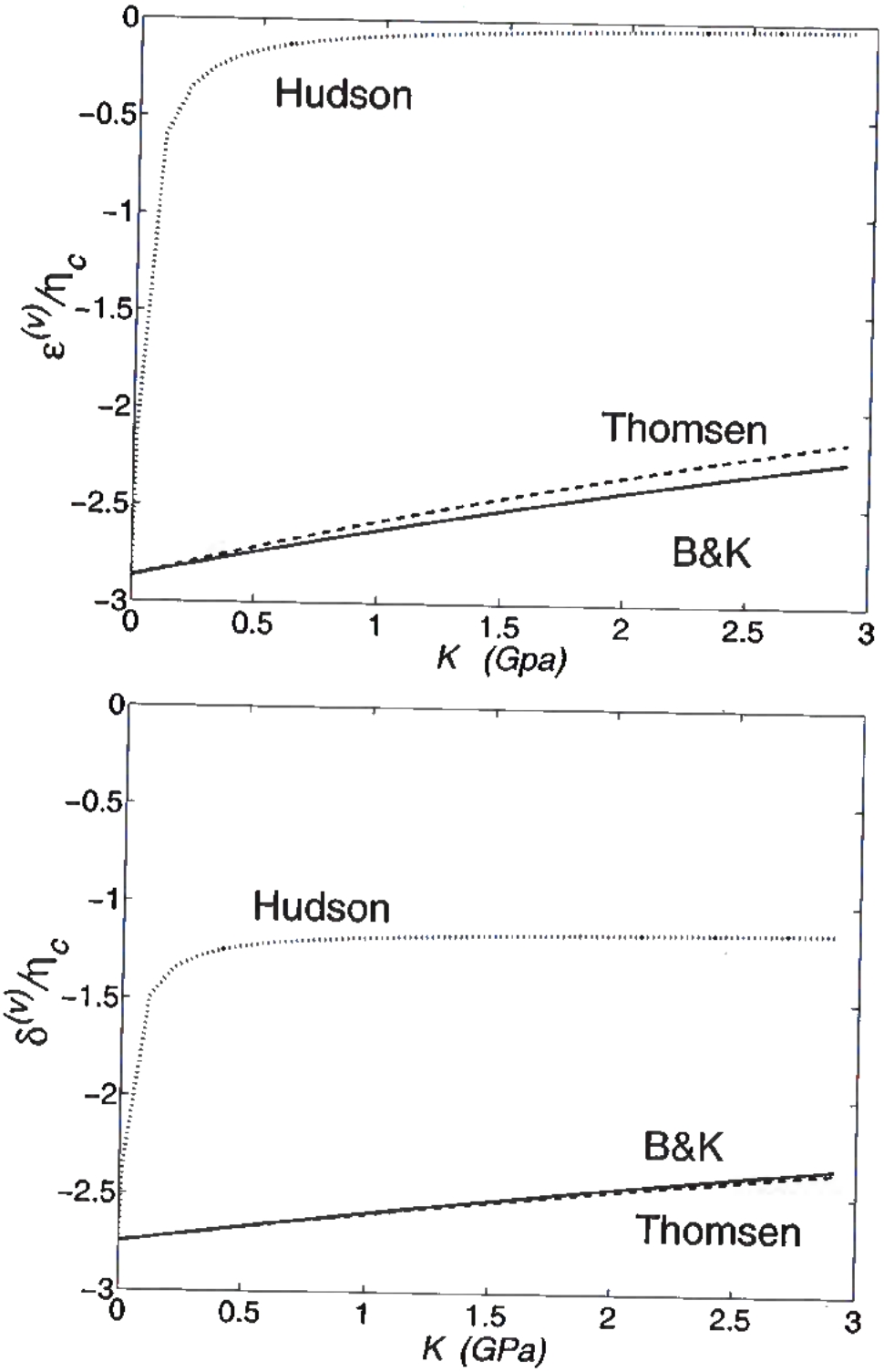

FIG. 3.3. $\epsilon^{(V)}$ and $\delta^{(V)}$ as a function of K_f for a calcite matrix with $\phi_i = 0.05$, $\phi_c = 10^{-4}$, $\eta_c = 0.05$ and $\alpha_c = 4\text{x}10^{-4}$.

the high- and low-frequency limit, depends weakly on the elastic properties of the mineral materials that compose typical sedimentary rocks. Feldspars, limestones and dolomites with Poisson's ratio varying between 0.25 and 0.35 have almost identical $\epsilon^{(V)}$ vs. K_f and $\delta^{(V)}$ vs. K_f dependence. Hence, the results shown in Figures 3.2-3.5 below assume a fixed isotropic limestone matrix with bulk and shear moduli of $K_m = 77\ GPa$ and $G_m = 32\ GPa$, respectively.

In the moderately high-frequency limit, Figure 3.2 shows that there is an almost perfect match between the predictions by Thomsen's (squares), Hudson's (1981) (crosses) and the anisotropic squirt theory (dotted line). This was expected from the analytical equivalence of the anisotropic squirt theory and Thomsen's moderately high-frequency formulation. As pointed out by Mukerji and Mavko (1994), the result shown in Figure 3.2 indicates that Hudson's (1981) theory is suitable for modeling fluid substitution in the high-frequency limit.

Figure 3.3 shows the change with saturation of the $\epsilon^{(V)}$ and $\delta^{(V)}$ parameters for the low-frequency limit, normalized by the crack density . These results are for a cracked limestone with an isotropic porosity of $\phi_i = 0.05$, a crack porosity of $\phi_c = 10^{-4}$, and a crack density and aspect ratio of $\eta_c = 0.05$ and $\alpha_c = 4x10^{-4}$, respectively. Hudson's (1981) prediction is also provided for comparison.

As expected from the condition of equilibrated pore pressure, both Thomsen's and B&K theory predict smaller changes with saturation in the anisotropies than Hudson's (1981) theory. Thomsen's low-frequency formulation overstates the changes of the $\epsilon^{(V)}$ and $\delta^{(V)}$ parameters with saturation. However, Figure 3.3 indicates that the discrepancy for an isotropic porosity of $\phi_i = 0.05$ is small for $\epsilon^{(V)}$ and almost null for the $\delta^{(V)}$ parameter.

Thomsen (1995) noted that under conditions of equilibrated pore pressures the fluid variation of the anisotropies is not sensitive to changes in the aspect ratio of the cracks. This is consistent with the B&K's results shown in Figure 3.4 where there is almost no variation in the $\epsilon^{(V)}$ vs. K_f or $\delta^{(V)}$ vs. K_f curves when the aspect ratio varies three orders of magnitude.

Figure 3.5 indicates that the numerical differences between Thomsen's low-frequency formulation and Brown and Korringa's theory are small for an isotropic background of dilute spherical pores ($\phi_i < 0.1$). The small discrepancy in this example results from the low value of the isotropic porosity and the low compaction compressibility ($1/K_{\phi_i}$) of the spherical inclusions. As mentioned in section 3.3.3, Thomsen's low-frequency formulation disregards that the isotropic pores expel fluids towards the neighboring cracks when tractions parallel to the cracks are applied, which results in "isotropic background" compliances that depend on the fracture parameters. If the isotropic pores are very stiff (small $1/K_{\phi_i}$), the fluid transfer towards the cracks due to the applied traction will be small and the discrepancy between the two formulations will be small as well.

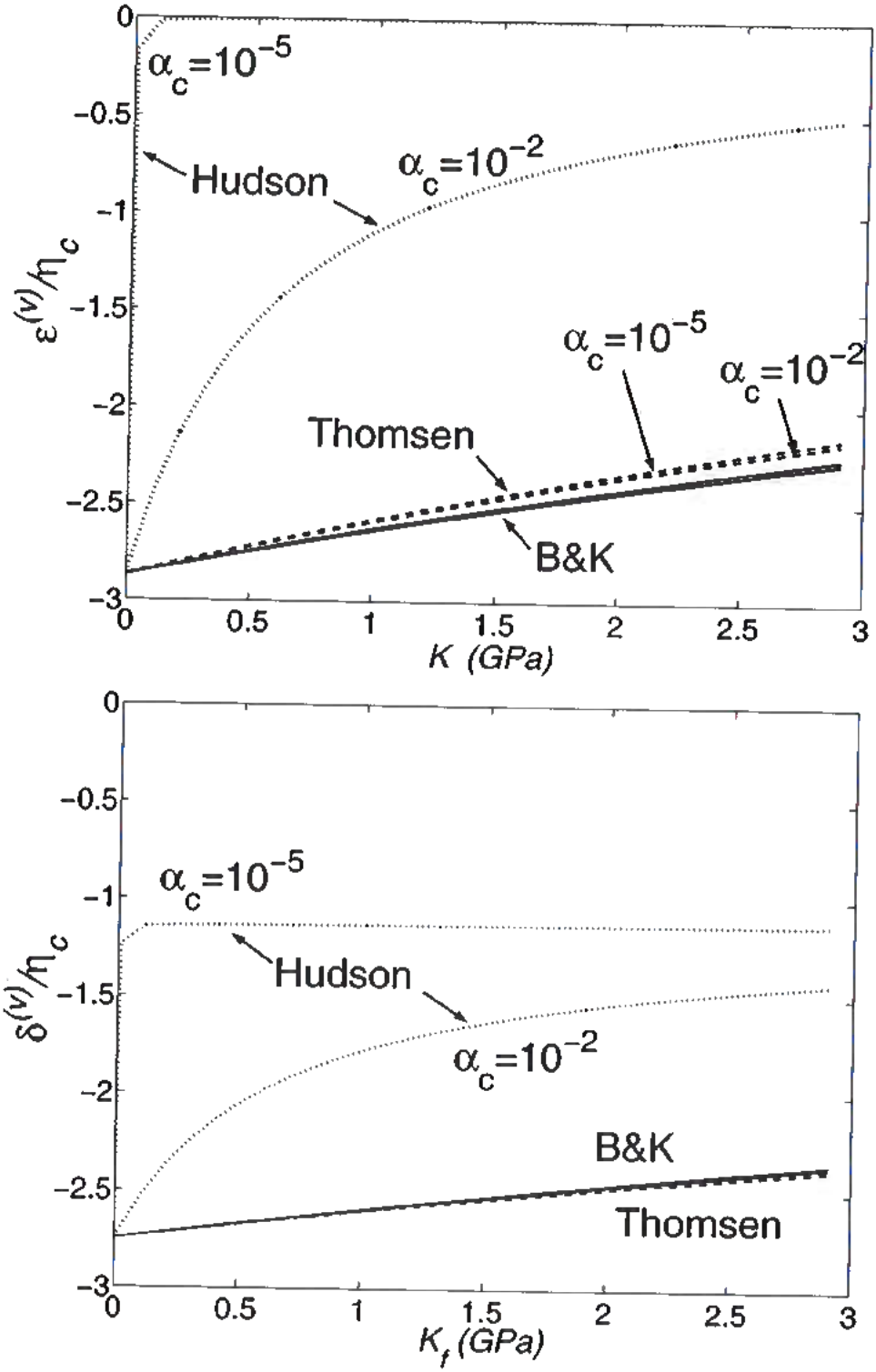

FIG. 3.4. Sensitivity of $\epsilon^{(V)}$ and $\delta^{(V)}$ to the crack aspect ratio for a calcite matrix with $\phi_i = 0.05$ and $\eta_c = 0.05$. $\alpha_c = 10^{-5}$ corresponds to $\phi_c = 2.1\text{x}10^{-6}$ and $\alpha_c = 10^{-2}$ corresponds to $\phi_c = 2.1\text{x}10^{-3}$.

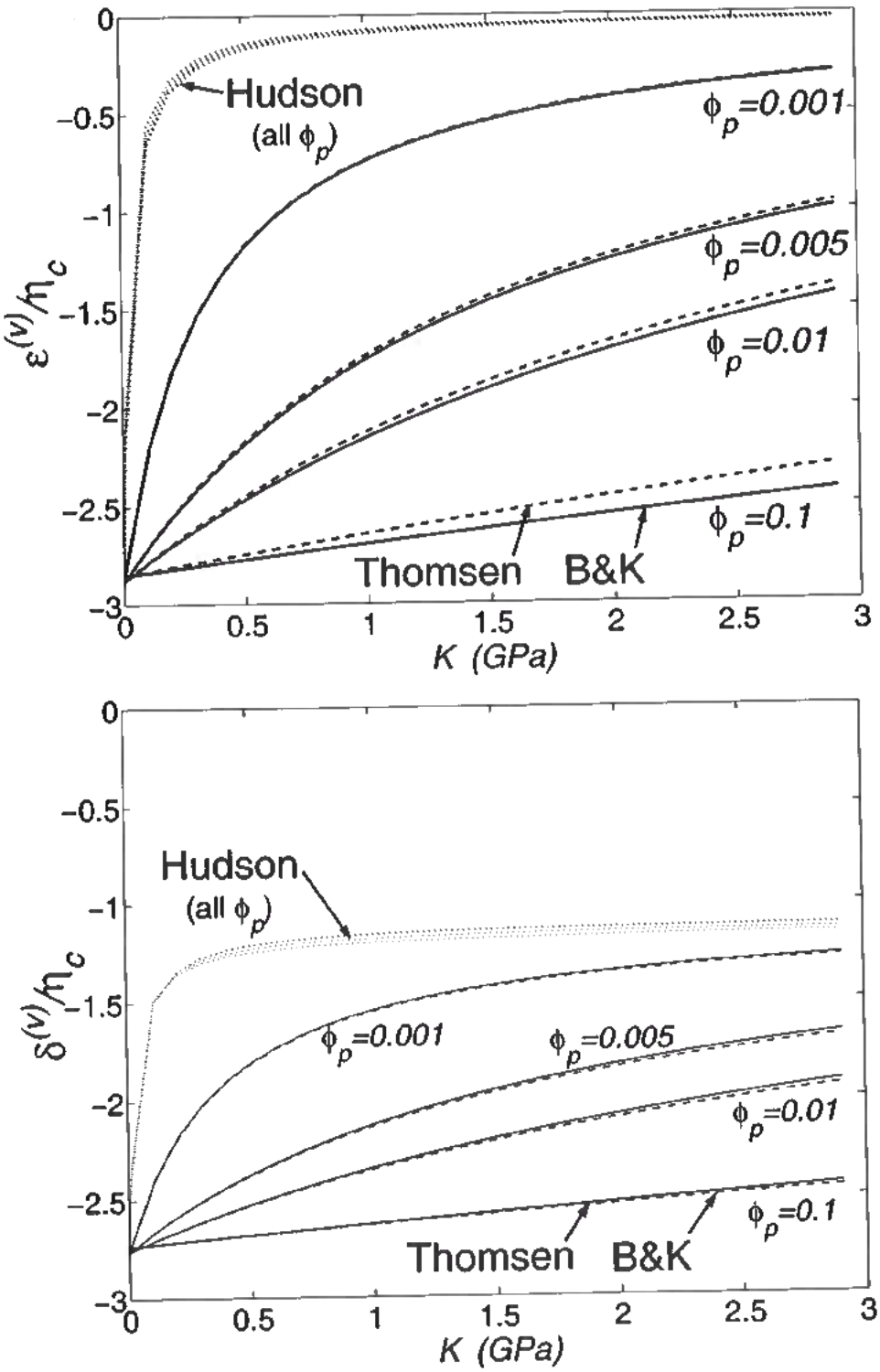

FIG. 3.5. $\epsilon^{(V)}$ and $\delta^{(V)}$ as a function of K_f for several values of the isotropic porosity. Curves are calculated for a calcite matrix with $\eta_c = 0.05$ and $\alpha_c = 4\text{x}10^{-4}$.

In order to have a better idea of the discrepancies that can be expected in real rocks that do not have spherical pores, linear fits of $1/K_d$ vs. ϕ_i and $1/\mu_d$ vs. ϕ_i derived for Weyburn field reservoir were used to model the isotropic background rock. Figure 3.6 shows plots of $1/K_d$ and $1/\mu_d$ as a function of isotropic porosity calculated from dipole sonic log measurements in the Midale reservoir interval (Reasnor, 2001). Even though four different facies of limestone and dolomite have been identified from the well, a single linear fit was applied to all the data points to obtain "average" estimates of $1/K_m$ and $1/K_{\phi_i}$. If the rock is approximately homogeneous the dry compressibility is given by:

$$\frac{1}{K_d} = \frac{1}{K_m} + \frac{\phi_i}{K_{\phi_i}}. \tag{3.42}$$

Hence, from the linear fit in Figure 3.6, the "average" rock can be modeled has having a mineral compressibility $1/K_m \approx 0.018$ and a compaction compressibility $1/K_{\phi_i} \approx 0.22$. Notice that for figures 3.3-3.5 the compaction compressibility is $1/K_{\phi_i} = 0.03$, which indicates that the spherical pores are almost 10 times less compressible than the "average" pore in the Midale interval.

Figure 3.7 shows the $\epsilon^{(V)}$ and $\delta^{(V)}$ parameters as a function of the isotropic porosity for a background isotropic rock modeled with the fits obtained for Weyburn rocks. The curves are calculated assuming the fracture density $\eta_c = 0.05$, crack aspect ratio $\alpha_c = 4.7 \text{ x } 10^{-4}$, crack porosity $\phi_c = 10^{-4}$ and bulk modulus of the fluid $K_f = 10^{-4}$.

Thomsen's low-frequency prediction overestimates the change with saturation for both the $\epsilon^{(V)}$ and $\delta^{(V)}$ parameters. At large porosity, the difference between the values of $\epsilon^{(V)}$ for dry and saturated rocks is almost twice as large as the one predicted by B&K's theory. For the $\delta^{(V)}$ parameter, Thomsen's formulation can overestimate the change with saturation for about one third of the B&K prediction. This indicates that discrepancies between the theories may not be negligible in rocks with large isotropic porosity ($\phi_p > 0.1$).

3.6 Discussion and Conclusions

This work compares the fluid substitution theories formulated by Thomsen (1995), Brown and Korringa (1975) and Mukerji and Mavko (1994). In the moderately high-frequency limit Thomsen's (1995) formulation is equivalent to the anisotropic squirt theory developed by Mukerji and Mavko. Hence, for high-frequency experiments the elastic compliance of a fractured rock can be modeled as the sum of the fluid-saturated compliance of the isotropic background and the fluid-saturated excess fracture compliance as described by Thomsen (1995).

In the low-frequency limit, Thomsen's (1995) formulation does not account for the full pressure equalization that occurs between the isotropic pores and the cracks.

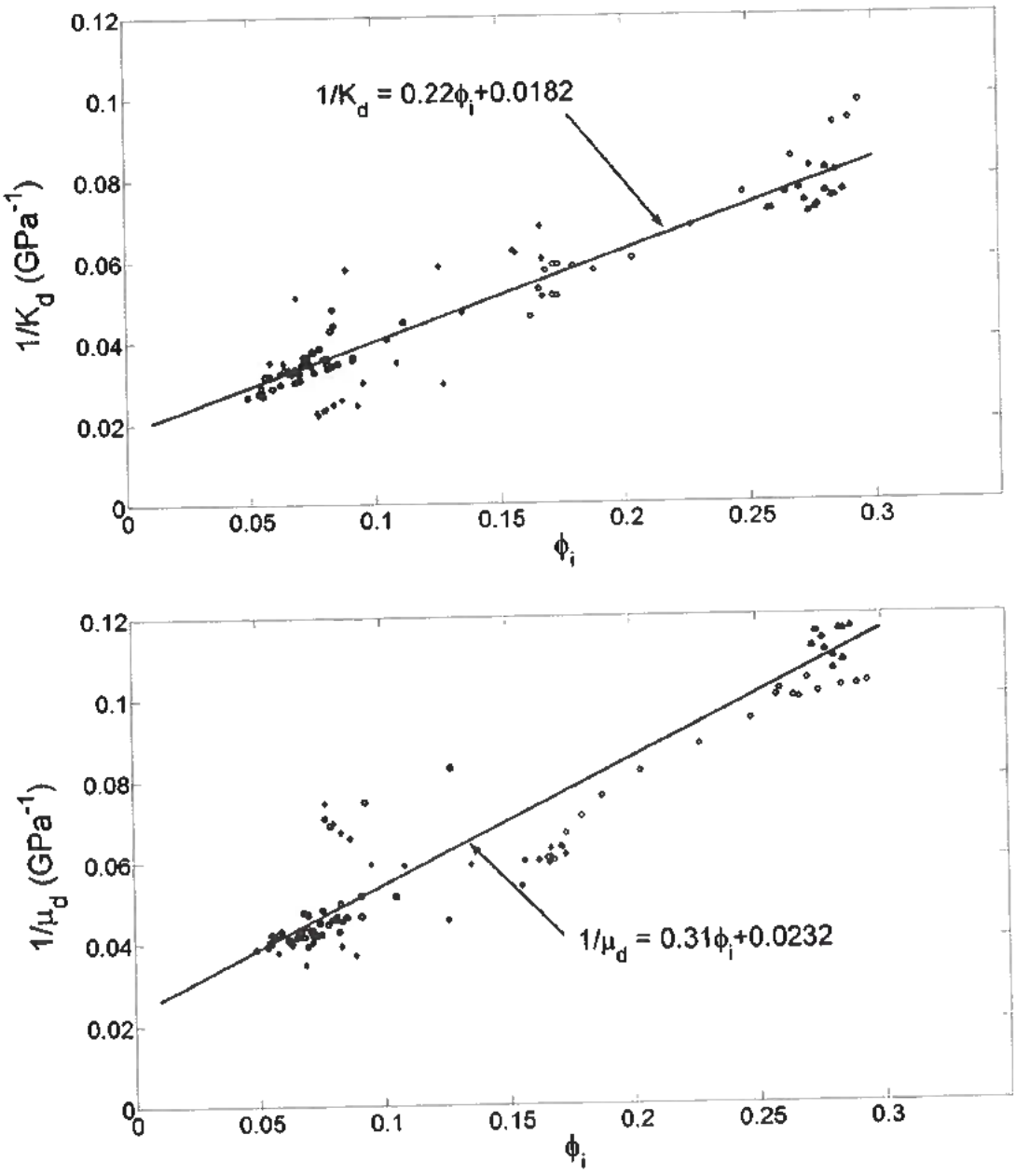

FIG. 3.6. $1/K_d$ and $1/\mu_d$ as a function of isotropic porosity calculated from dipole sonic log measurements in the Midale reservoir interval (Reasnor, 2001). Four different reservoir facies are identified: "porous" marly (triangles), "tight" marly (circles), inter-shoal vuggy (diamonds) and shoal vuggy (squares).

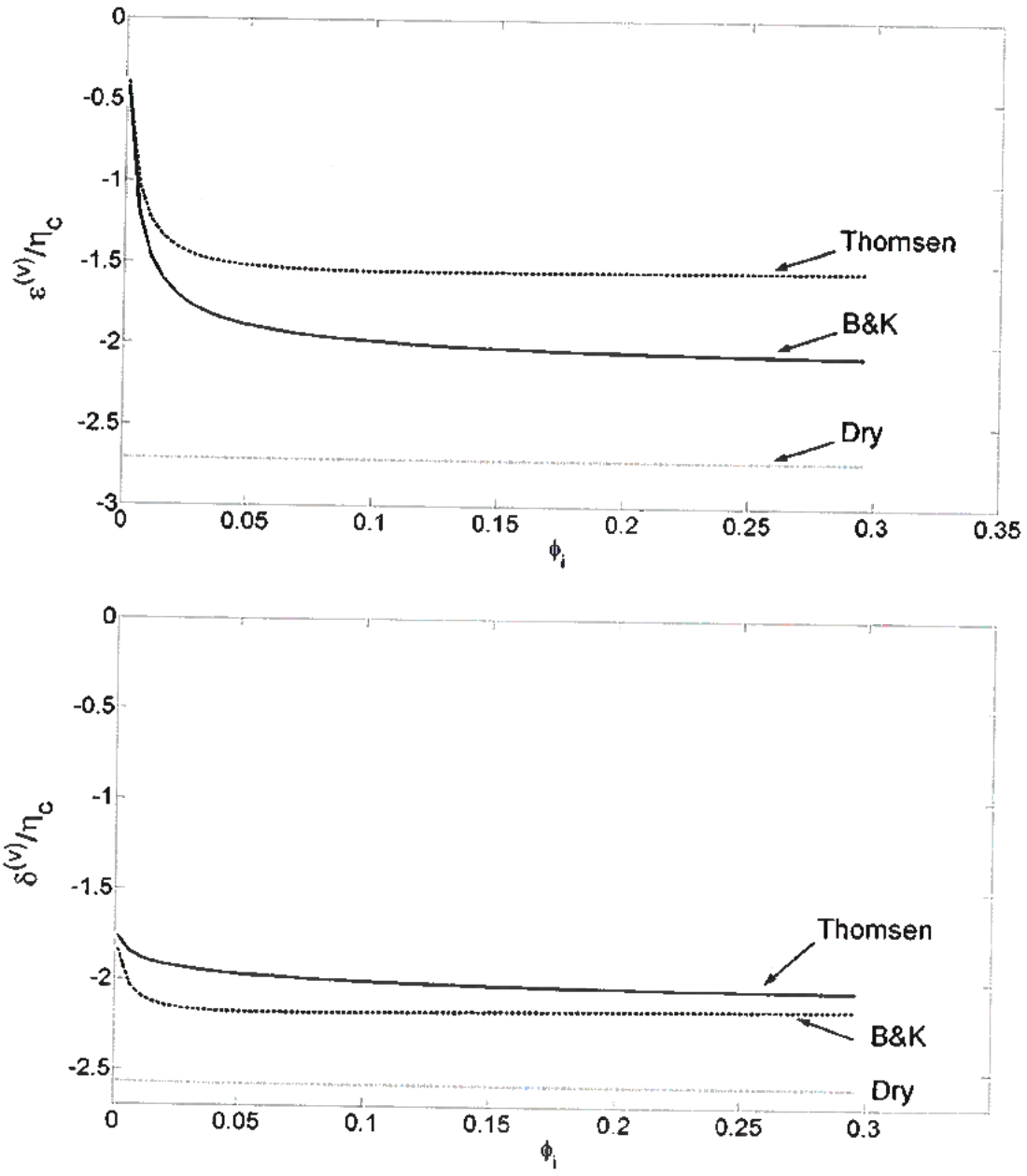

FIG. 3.7. $\epsilon^{(V)}$ and $\delta^{(V)}$ parameters as a function of the isotropic porosity. The curves are calculated with a fracture density $\eta_c = 0.05$, a crack aspect ratio $\alpha_c = 4.7 \text{ x } 10^{-4}$, a crack porosity $\phi_c = 10^{-4}$ and a bulk modulus of the fluid $K_f = 10^{-4}$. The isotropic background rock is modeled with the fits obtained for Weyburn rocks in Figure 3.6.

This results in an overestimation of the change of the $\epsilon^{(V)}$ and $\delta^{(V)}$ parameters with saturation for rocks with large isotropic porosity. The main implication from these results is that the decomposition of the compliance matrix that has been used traditionally in linear slip theory [equation (3.9)], is not always valid in the presence of fluid pressure equilibrium.

The results presented in this chapter prove that the fluid influence factor that determines the magnitude of the change of the normal fracture compliance with saturation, can be re-interpreted as being inversely proportional to the total storage capacity of the rock. Since the total storage capacity is a parameter estimated regularly by well test engineers from pressure-transient experiments, it can provide information on how sensitive the normal fracture compliance is to changes in fluid saturation. When the isotropic porosity is small, the reduced storage capacity results in a large fluid influence factor and large changes in the normal fracture compliance with saturation.

Even through there are cases in which Brown and Korringa's and Thomsen's low-frequency formulations are numerically close, B&K has the advantage of being a more general theory. Brown and Korringa's equations are valid for arbitrary symmetry and arbitrary strength of anisotropy. No assumptions about the detailed structure of the fractures are required and it could apply to rocks with an arbitrary number of fracture sets as long as the fluid pressure is equilibrated throughout the pore space. Therefore, a more general approach to modeling the elasticity of fractured rocks is to model the dry rock with any appropriate theory (e.g. the linear slip theory) and then calculate the fluid-saturated values from Brown and Korringa's equations.

The linear slip theory is convenient for modeling dry rocks because it does not require detailed information about the microstructure of the fractures and is valid for several non-interacting fracture sets. The condition of non-interacting fractures can be met assuming the fracture volume density is small. When the rock is fluid-saturated, all interactions between pores due to the condition of equilibrated pore pressures is taken into account through Brown and Korringa's equations.

For naturally fractured rocks it may be argued that the non-interacting fracture condition is in conflict with the condition of equilibrated pore pressures since pressure equilibrium requires hydraulic connectivity between all pores. This argument can be countered assuming that the non-interacting fractures are connected through the background pores or assuming that every *real* dry rock has a linear slip equivalent that can be used to model it. Ultimately it will be the application of the theory to real data that will determine its validity.

Chapter 4

SHEAR-WAVE VELOCITY DEPENDENCE ON FLUID SATURATION

4.1 Introduction

Characterization of fractured reservoirs is an important area of research. If the fractures have preferential orientations, the reservoir may become anisotropic with respect to wave propagation and fluid flow. By characterizing this anisotropy we can obtain information about the properties of the fracture network. The migration of fluids through the fractured reservoir is information that can be obtained from time-lapse seismic measurements.

Traditionally, the reservoir geophysics community has favored the use of time-lapse, compressional waves for monitoring fluid movement in the reservoir. Even though it has long been recognized that the shear-wave moduli are sensitive to the changes of pressure that accompany fluid movement, the idea that shear-wave moduli may vary due to the fluid content is still not well accepted.

Gassmann (1951) provided a theory of fluid substitution that allows us to obtain the bulk and shear moduli of the fluid-saturated rock from the dry rock compliance, rock porosity, mineral and fluid compressibility. This can be done under the assumptions that the rock is (1) isotropic, (2) monomineralic, and (3) that the pressure is equilibrated throughout the pore space. This theory predicts that the rock's bulk modulus (K) changes with saturation but the shear modulus (G) remains fixed. Hence, arises the commonly accepted notion that P-waves are sensitive to pore fluids while, except for density effects, S-waves are not.

However, the interpretation of recent multicomponent data has suggested that the slow shear-wave modulus of vertically propagating shear-waves, may decrease in the presence of high compressibility fluids (Guest et al., 1998; Duranti et al., 2000). The apparent contradiction of these results with the generally accepted view that shear waves are insensitive to fluids relies in that the assumption of elastic isotropy is violated when aligned sets of fractures make the rock anisotropic. Chapters 6 and 7 will also show that the time-lapse analysis performed at Weyburn field, Canada suggests that the vertically propagating shear-waves are sensitive to changes in the fluid compressibility.

Fluid substitution theories for rocks with penny shaped cracks, suggest that the S-wave modulus will only be sensitive to fluid saturation when waves propagate at oblique angles with respect to the crack plane, because in those cases the shear stresses

will have a component normal to the crack face. However, S-waves travelling parallel to the crack plane will not be fluid-sensitive in models with rotationally invariant fractures.

Through a heuristic explanation, Bakulin et al. (2000c) suggested that changes with saturation in the shear modulus of vertically propagating shear waves are possible in a rock with monoclinic symmetry, generated by one set of micro-corrugated fractures in an isotropic background. This model has a vertical symmetry plane perpendicular to the fractures. In such fracture system, the normal displacements, which are sensitive to the fluid content, are coupled to the tangential tractions along the fracture faces which determine shear-wave splitting.

Using Brown and Korringa (1975) theory, I show that under conditions of equilibrated pore pressures, rocks with symmetry lower or equal to monoclinic have "shear moduli" that are sensitive to pore fluids. Therefore, the model of micro-corrugated fractures proposed by Bakulin et al. (2000c) belongs to a larger group of rocks for which Brown and Korringa's theory predicts changes of shear-wave velocities with saturation.

The shear-wave sensitivity to fluids originates from the effective symmetry of the fractured rock but it is influenced by the "isotropic" porosity, the mineralogy of the rock and the bulk modulus of the saturating fluid. Under conditions of equilibrated pore pressures, transversely isotropic (TI) and orthorhombic symmetry rocks will only show changes with saturation of vertical shear-waves when the symmetry planes of the rock are tilted with respect to the vertical direction.

This chapter concentrates on monoclinic symmetry rocks. The changes in the rock compliances with saturation are quantified for the cases of: (i) one set of vertical, micro-corrugated fractures in an isotropic background (ii) one set of dipping, rotationally invariant fractures in a transversely isotropic background with a vertical symmetry axis, and (iii) two vertical sets of non-orthogonal penny-shaped cracks in an isotropic background.

The results for the cases of micro-corrugated fractures and dipping, rotationally invariant fractures indicate that the shear-wave splitting parameter increases with the compressibility of the saturating fluid. In the case of the model with two sets of vertical, non-orthogonal, penny-shaped cracks in an isotropic background, vertically propagating shear waves do not change with saturation. However, the azimuthal variation of the normal-moveout (NMO) velocities of the P, S_1 and S_2 modes is sensitive to pore fluids with the S_1-wave being the most sensitive.

4.2 Fluid Substitution Theory

Brown and Korringa (B&K) generalized Gassmann's work by relaxing the conditions of isotropy and monomineralic rock. In this way, Gassmann's scalar equations

that relate the bulk and shear moduli of the dry and fluid-saturated cases, are replaced by a tensor equation that relates the compliances of the dry and saturated rock. Since the complications related to multimineralic rocks are beyond the scope of the work presented in this chapter, only the B&K formulation for the monomineralic case will be used.

Brown and Korringa's equation can be written as:

$$S^d_{ijkl} - S^s_{ijkl} = \frac{(S^d_{ij\alpha\alpha} - S^m_{ij\alpha\alpha})(S^d_{kl\alpha\alpha} - S^m_{kl\alpha\alpha})}{(S^d_{\alpha\alpha\beta\beta} - S^m_{\alpha\alpha\beta\beta}) + (c_f - S^m_{\alpha\alpha\beta\beta})\phi_t}, \tag{4.1}$$

where S^d_{ijkl} and S^s_{ijkl} are the compliances of the dry and fluid-saturated rock, S^m_{ijkl} is the compliance of the mineral material, c_f is the compressibility of the fluid, and ϕ_t is the total connected porosity. The quantities $S^d_{\alpha\alpha\beta\beta}$ and $S^m_{\alpha\alpha\beta\beta}$ in the denominator are the compressibilities of the dry rock and mineral material, respectively. Due to the double index contraction both quantities are scalars and they can be defined as $S^d_{\alpha\alpha\beta\beta} \equiv c_d$ and $S^m_{\alpha\alpha\beta\beta} \equiv c_m$.

Equation (4.1) assumes the rock is subjected to slowly varying stresses such that the pressure is equilibrated throughout the pore space. This condition can be satisfied when the fluid substitution occurs in a well connected pore space. However, the effect of fluids in disconnected cavities could be included in equation (4.1) as part of the "solid" through effective mineral (c_m) and dry (c_d) compressibilities.

Greater intuition into the meaning of Brown and Korringa's equation can be achieved by rewriting equation (4.1) in the conventional (2-subscript) 6x6 matrix notation. By doing this, it is clear that the terms with contracted indices ($S_{ij\alpha\alpha}$) in the numerator of equation (4.1) represent the sums of elements of the first three rows of the 6x6 compliance matrix. Therefore, by defining ψ_K as the sum of the first three elements of the K-th column of the compliance matrix, as shown in Figure 4.1a, B&K's equation can be rewritten as:

$$S^d_{IJ} - S^s_{IJ} = \frac{(\psi^d_I - \psi^0_I)(\psi^d_J - \psi^0_J)}{(c_d - c_m) + (c_f - c_m)\phi_t}. \tag{4.2}$$

Although equations (4.1) and (4.2) are equivalent, now it is easier to see when changes in vertical shear-wave velocities may be expected with saturation based on the symmetry of the rock. Figure 4.1a shows a compliance matrix of general symmetry subdivided into four blocks, two diagonal and two off-diagonal. For symmetries in which the off-diagonal blocks of the compliance matrix are zero, vertical shear-wave velocities will depend only on the S_{44} and S_{55} compliances. Since in these cases the sums ψ_4 and ψ_5 are zero (see Figure 4.1b), from equation (4.2) we see that $S^d_{kk} = S^s_{kk}$ for $k = 4, 5$. This means that for these symmetries the vertically propagating shear waves do not depend on fluid saturation.

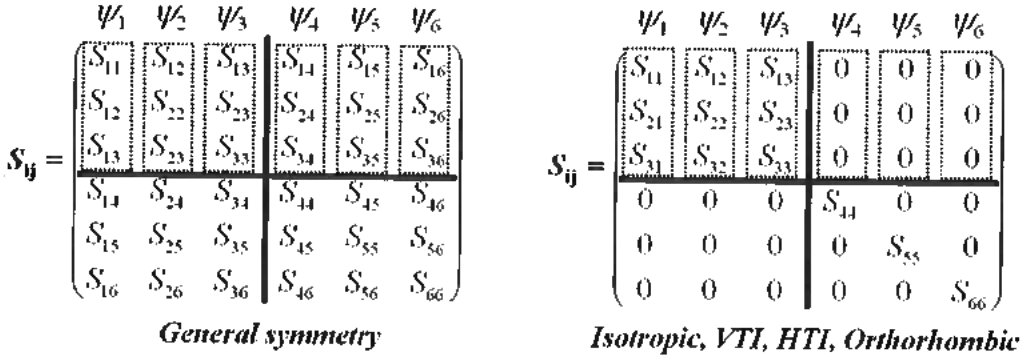

FIG. 4.1. Illustration of how the symmetry of the rock determines changes in the shear compliances with saturation. (a) Compliance matrix of general symmetry indicating elements that contribute to the sums ψ_K in equation (4.2). (b) The change with saturation of the components S_{44}, S_{55} and S_{66} depends on the sum of the elements in columns ψ_4, ψ_5 and ψ_6, which vanish for isotropic, VTI, HTI and non-tilted orthorhombic media. In monoclinic rocks the sums ψ_4, ψ_5 and ψ_6 may be non-zero resulting in fluid dependent shear compliances.

For isotropic rocks, the off-diagonal blocks of the compliance matrix are zero and $1/G = S_{44} = S_{55}$, where G is the shear modulus. Therefore, from the above explanation, Gassmann's result that states that the shear modulus does not depend on fluid saturation is obtained immediately. In the case of transverse isotropy and orthorhombic symmetry rocks whose symmetry planes are *not* tilted with respect to the vertical axis, the off-diagonal compliance blocks are also zero and the vertical shear waves are not sensitive to saturation (see Figure 4.1b).

If an anisotropic rock has a symmetry lower than orthorhombic (e.g. monoclinic) in which the sums ψ_4 and/or ψ_5 are non-zero, the vertically propagating shear waves may be sensitive to the pore fluids. This will occur because either S_{44} or S_{55} will be fluid sensitive and also because the S-wave velocities will depend on other compliances besides S_{44} and S_{55}.

The arguments above have been stated under the assumption that the symmetry planes of the anisotropic rock are not tilted with respect to the vertical propagation axis. If tilt is allowed, even a transversely isotropic rock may present fluid sensitive, vertical shear waves. This can be understood considering the compliance matrix of a horizontal transversely isotropic rock (HTI), with symmetry axis in the X_1 direction, that has been rotated by an angle θ around the X_2 axis according to the so called

Bond transformation. The rotated compliance is calculated as $S_{rot} = N(\theta)S^{X_1}N^T(\theta)$, where S^{X_1} is the HTI compliance and $N(\theta)$ is the rotation matrix [$N(\theta)$ can be found explicitly in Mavko et al. (1999)].

After rotation, the tilted HTI compliance has the following non-zero terms,

$$S_{rot} = \begin{pmatrix} S_{11} & S_{12} & S_{13} & 0 & S_{15} & 0 \\ S_{12} & S_{22} & S_{23} & 0 & 0 & 0 \\ S_{13} & S_{23} & S_{33} & 0 & S_{35} & 0 \\ 0 & 0 & 0 & S_{44} & 0 & S_{46} \\ S_{15} & 0 & S_{35} & 0 & S_{55} & 0 \\ 0 & 0 & 0 & S_{46} & 0 & S_{66} \end{pmatrix}. \tag{4.3}$$

By the arguments stated previously it is clear that the S_{55} component and one of the vertically propagating shear-wave velocities will change with saturation. This observation indicates that vertical shear waves that are sensitive to pore fluids may be a common phenomenon. The fact that it has seldom been reported from surface seismic experiments is probably due to the small number of multicomponent, time-lapse experiments that have been acquired.

The next sections will treat the case of fractured rocks with monoclinic symmetry which will show changes in shear-wave velocities with saturation even when the symmetry planes are not tilted with respect to the vertical propagation direction.

4.3 Methodology

The results presented in the following sections compare the rock compliances and vertical shear-wave velocities of the dry and fluid-saturated rock. First the compliance and compressibility of the mineral material and the dry rock are modeled. Then equation (4.2) is used to calculate the compliance of the 100% brine saturated rock and compare the results for both saturations. It is assumed that for all the models the compliance matrix of the dry, fractured rock can be calculated using Schoenberg's linear slip theory (Schoenberg and Muir, 1989; Schoenberg and Sayers, 1995), as the sum of a background compliance and an excess fracture system compliance matrix:

$$S^d = S^d_{back} + S^d_{frac}.$$

If the background is isotropic, S^d_{back} is calculated from empirical relations of $V^d_P(\phi_i)$, $V^d_S(\phi_i)$ and density $\rho^d(\phi_i)$, all functions of the isotropic porosity ϕ_i. The total porosity of the rock is $\phi_t = \phi_i + \phi_c$, where ϕ_c is the crack (fracture) porosity that only influences the fracture system compliance S^d_{frac}.

In all the models considered in this chapter the mineral material of the background rock is isotropic. The calculations are done for quartz, calcite, and dolomite.

Mineral material	K (GPa)	G (GPa)
Quartz	36.5	45.6
Calcite	70.2	29.0
Dolomite	94.9	45.0

Table 4.1. Moduli of background mineral material [from Mavko et al. (1999)].

The values of the bulk (K) and shear modulus (G) are taken from Mavko et al. (1999) (see Table 4.1).

The calculations have been done for a fluid substitution that occurs throughout the entire pore space including all the isotropic and fracture porosity. Since the permeability of the isotropic background is typically smaller than the permeability of the fractures, it is assumed that sufficient time is allowed to have a complete fluid substitution in the background matrix.

4.4 One Set of Micro-corrugated Fractures in an Isotropic Background

Using Schoenberg's linear slip theory, Bakulin et al. (2000c) have studied the anisotropy produced by one system of micro-corrugated fractures embedded in an isotropic background, with the normals in the X_1 direction. By micro-corrugated it is meant that the fracture surfaces are irregular at a scale much smaller than a seismic wavelength. The irregularity can be idealized as saw-tooth profiles that are offset from one fracture surface to the other as shown in Figure 4.2. In this idealization the "roughness" of the fracture surface in the X_3 direction causes a coupling between normal tractions and tangential displacements when the fracture is stressed.

The symmetry of this effective medium is monoclinic with a vertical symmetry plane, and its compliance matrix can be written as the sum of the isotropic compliance of the background plus the fracture-system compliance,

$$S_{rock} = S_{iso} + \begin{pmatrix} Z_N & 0 & 0 & 0 & Z_{NV} & 0 \\ 0 & 0 & 0 & 0 & 0 & 0 \\ 0 & 0 & 0 & 0 & 0 & 0 \\ 0 & 0 & 0 & 0 & 0 & 0 \\ Z_{NV} & 0 & 0 & 0 & Z_V & 0 \\ 0 & 0 & 0 & 0 & 0 & Z_H \end{pmatrix}. \tag{4.4}$$

Here Z_N is the normal compliance of the fractures that relates the normal displacements to the normal stresses applied to the fracture in the X_1 direction. The Z_V and Z_H elements are the tangential compliances that relate tangential displacements and stresses in the X_2 and X_3 directions, respectively. The Z_{NV} compliance is responsible

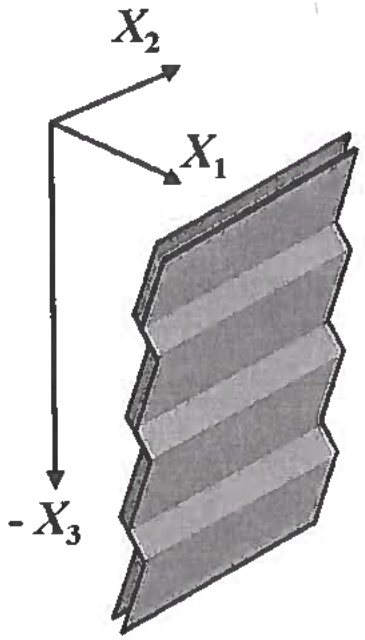

FIG. 4.2. Vertical fracture with rough structure that causes coupling between the normal and tangential displacements.

for the coupling of normal displacements to tangential applied stresses, or conversely, the coupling of tangential displacements to applied normal stresses (see Figure 4.2).

From equation (4.2) and (4.4) it is clear that the S_{44} and S_{66} shear compliances of the fractured rock will not change with saturation because the sums ψ_4 and ψ_6 of S_{rock} in equation (4.2) are zero. However, S_{55} will change with saturation because $\psi_5 = Z_{NV}$ and the right side of equation (4.2) will be non-zero. From this analysis we see that, under the assumption that the background rock is isotropic, Brown and Korringa's equation requires that the term Z_{NV} of the dry rock be non-zero to have changes in the S_{55} shear compliance. This result stands in contrast with the heuristic proposal by Bakulin et al. (2000c) in which they suggest that the reason why shear-wave velocities change with saturation is that the term Z_{NV} is zero for dry rocks and non-zero for saturated rocks.

To obtain more information on how the compliance terms Z_{NV} and Z_V change with saturation, I have explicitly derived relations between the compliances of the dry and saturated rocks using equations (4.2) and (4.4) (See Appendix D). The difference between the dry and saturated values of the compliances is a function of

the mineral and fluid compressibility, the total rock porosity and the values of the dry-rock normal and coupling compliances (Z_N^d and Z_{NV}^d). Even though there is no micro-structural theory that predicts the values of the fracture compliances for this model, reasonable bounds can be obtained from the stability condition of the compliance matrix. Because the compliance matrix must be positive definite, physically realizable compliances, Z_N, Z_V and Z_{NV} must satisfy the inequality, $Z_N Z_V \geq Z_{NV}^2$.

The changes in the compliances with fluid saturation have a weak dependence on the compressibility of the mineral material. This can be understood in light of equations (D.6) and (D.7), where the contribution of the mineral compressibility is small if the compressibility of the fluid is much larger than that of the mineral.

Figure 4.3 shows the difference between the dry and saturated values of Z_{NV} and Z_V for a porous, fractured limestone (calcite matrix) that is 100% saturated with brine ($c_f \approx 0.44\ GPa^{-1}$). These curves are calculated using the equations derived in Appendix D assuming that the background is an isotropic, porous limestone matrix that can be modeled as dilute collection of spherical pores with a porosity $\phi_i \leq 0.1$.

From Figure 4.3 it is clear that the change with saturation of the compliances Z_{NV} and Z_V is strongly dependent on the value of Z_{NV}^d. As mentioned before, if $Z_{NV}^d = 0$ the symmetry of the rock is no longer monoclinic, and Z_{NV} and Z_V are not sensitive to the change of saturation.

An important observation is that if the coupling term is weakly dependent on the isotropic porosity (ϕ_i), larger changes in Z_{NV} and Z_V should be expected with saturation for smaller values of ϕ_i. As it will be shown below, the previous observation implies that changes in the shear-wave splitting with saturation are larger for rocks with small isotropic porosity.

The shear-wave splitting parameter for this monoclinic rock can be written in terms of the vertical velocities V_{S_1} and V_{S_2} of split shear-waves as:

$$\gamma \equiv \frac{V_{S_1}^2 - V_{S_2}^2}{2V_{S_2}^2}, \tag{4.5}$$

where V_{S_1} and V_{S_2} are given by

$$V_{S_1}^2 = \frac{G}{\rho}, \tag{4.6}$$

and

$$V_{S_2}^2 = \frac{G}{\rho} \frac{C_{33}C_{55} - c_{35}^2}{C_{33} + C_{55} + \sqrt{(C_{33} - C_{55})^2 + 4c_{35}^2}}, \tag{4.7}$$

and G is the shear modulus of the background isotropic rock. Bakulin et al. (2000c) have shown that equation (4.5) can be written to second order in the fracture com-

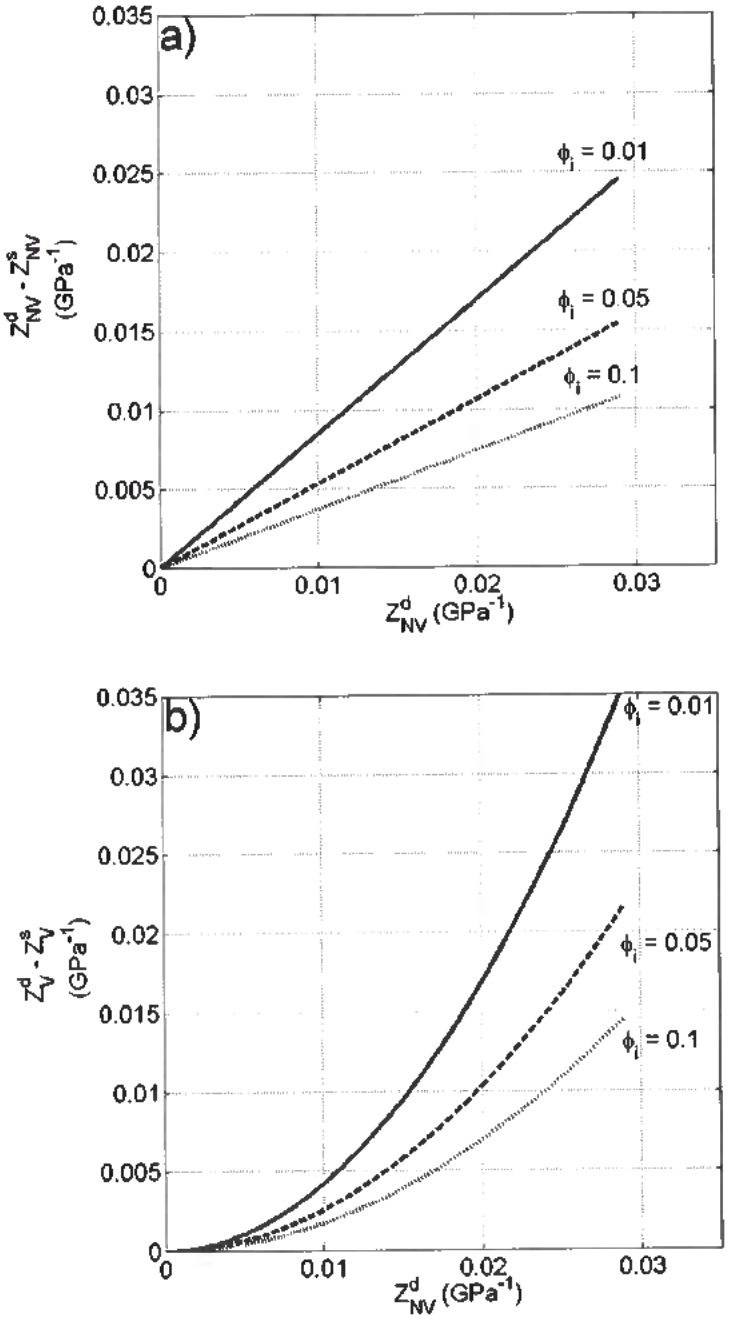

FIG. 4.3. Difference between the dry and saturated values of (a) the fracture coupling compliance, Z_{NV}, and (b) the fracture tangential compliance, Z_V, as a function of Z^d_{NV}. The curves are calculated using the equations derived in Appendix D for a fractured, porous limestone with values $Z^d_N = 0.02\ GPa^{-1}$ and $c_f = 0.44\ GPa^{-1}$.

pliances as:

$$\gamma \approx Z_V \frac{G}{2} - Z_{NV}^2 \frac{G^2 M^2 g(3-4g)}{2(1-g)}, \tag{4.8}$$

where M is the P-wave modulus. From equations (4.6) and (4.7) it is clear that the velocity of the S_1-wave will not change with fluid content since it depends only on the shear modulus of the isotropic background rock, whereas the velocity of the S_2-wave will change due to its dependence on the C_{33}, C_{55} and C_{35}. The shear-wave splitting, γ, will vary with saturation due to its dependence on Z_{NV} and Z_V, which vary with fluid content as shown in Figure 4.3.

To model the variation of the shear splitting with saturation, the compliance matrix of the brine saturated rock is calculated using equation (4.2). Then, the stiffness matrix is obtained from the inverse of the compliance, and equations (4.5)-(4.7) are used to compare the shear-wave splitting parameter of the dry and brine-saturated rock.

Figure 4.4 shows the dry-rock splitting parameter and the change after saturation as a function of the compliance Z_{NV}^d for a rock with an isotropic porosity $\phi_i = 0.15$. The calculations show that the velocity of the S_2-wave is larger for the brine-saturated rock than for the dry rock. Therefore, because the S_1 velocity is the same for the dry and saturated case, the shear-wave splitting parameter is smaller for the brine-saturated rock and larger for the dry rock (Figure 4.4b).

Even though all the combinations of parameters shown in Figure 4.4b satisfy the condition of positive definite compliance matrix, numerical calculations done by Nakagawa et al. (1999) suggest that the conditions, $Z_N^d \approx Z_V^d$ and $Z_N^d \geq Z_{NV}^d$ are the ones that hold for micro-corrugated fractures. Furthermore, they show that if the jagged sections of the micro-corrugated fracture are less than 30 degrees from the vertical, Z_N^d and Z_V^d are approximately equal to the normal and tangential compliances of a penny-shaped crack.

The combination of dry fracture compliances that seems more reasonable according to the range of values reported by Nakagawa et al. (1999), is the one represented by the diamonds in Figure 4.4 ($Z_{NV}^d \leq Z_N^d$, $Z_N^d \approx Z_V^d$). Taking this as a representative example of what can be expected from experimental data, the changes in γ can be as large as 0.01 for a shear splitting $\gamma^d = 0.1$. Although this represents a 10% change in the shear splitting it might not be a large enough change to be measured from seismic data. However, Figures 4.4 were calculated for a relatively high value of the isotropic porosity $\phi_i = 0.15$, and as seen from Figures 4.3 the variation in shear splitting with saturation is expected to be larger for small isotropic porosities. Figure 4.5 shows that for an isotropic porosity $\phi_i = 0.01$ the decrease in the shear-splitting from the dry- to brine-saturated state can be as large 0.08 for a shear-splitting $\gamma^d \approx 0.12$, which would be easier to measure from seismic data. The fact that the change in shear-splitting is larger for decreasing ϕ_i may seem counter-intuitive. However, this can be understood

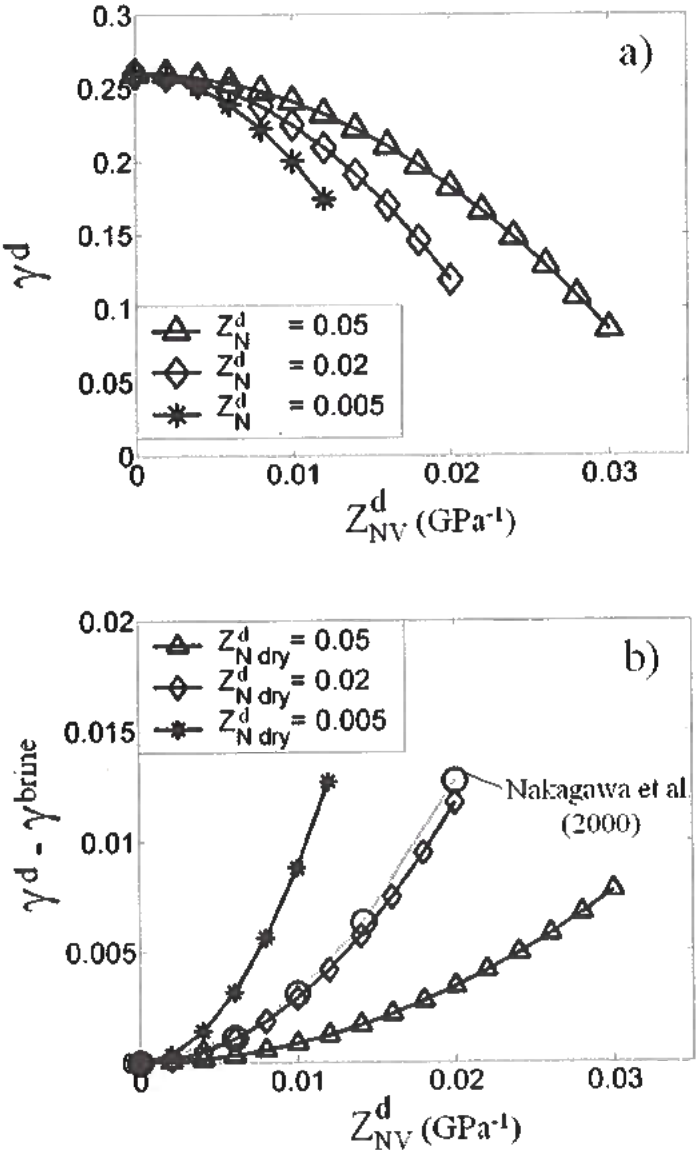

FIG. 4.4. Difference between dry and saturated splitting parameter as a function of Z^d_{NV} for several values of the normal compliance Z_N of the dry rock. (a) Shear-wave splitting for the dry rock. (b) Change in shear-wave splitting between the dry and brine-saturated rock. Calculations are done for a porous calcite matrix with a modeled isotropic porosity of 0.15 and a fixed value of $Z^d_V = 0.02\ GPa^{-1}$.

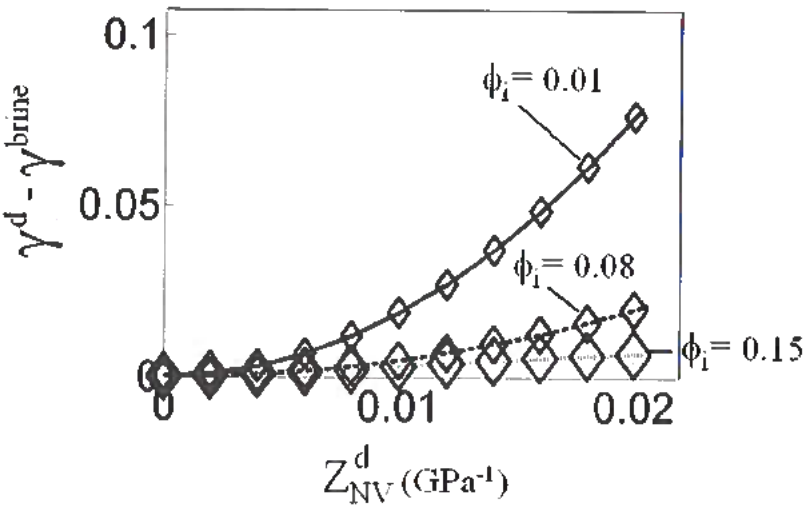

FIG. 4.5. Change in shear splitting for three values of the background isotropic porosity. Calculations are done for a calcite matrix with a fixed crack porosity $\phi_c = 10^{-4}$ and with fracture compliances that match Nakagawa's et al. condition in Figure 4.4 (diamonds).

by recalling the role of the storage capacity in the fluid substitution process that was presented in Chapter 3. When a stress is applied to the crack and the rock has a large isotropic porosity, its fluid storage capacity is large enough to accommodate fluids displaced from the cracks with only a small fluid pressure increase. If the porosity is small, the reduced storage capacity results in a larger fluid pressure increase that "stiffens" the crack more, reducing further the shear splitting of the brine-saturated rock.

Figure 4.6 shows the change in shear-splitting between the dry rock and a rock saturated with brine, oil and CO_2, calculated for $\phi_i = 0.01$. Due to the similar values of the compressibility of oil and brine compared to CO_2 it would be easier to distinguish a change from brine to CO_2 than from brine to oil.

From this modeling we may conclude that, for a rock with micro-corrugated fractures in an isotropic background, the vertical shear-wave splitting should increase if a low-compressibility fluid is replaced with a high-compressibility fluid (e.g. gas at low differential pressures that displaces oil or water). This result is qualitatively consistent with the findings of Guest et al. (1998) in which the splitting parameter increased due to a decrease in the S_2-wave velocity in areas believed to be saturated with highly compressible gas. This observation was done from interpretation of a

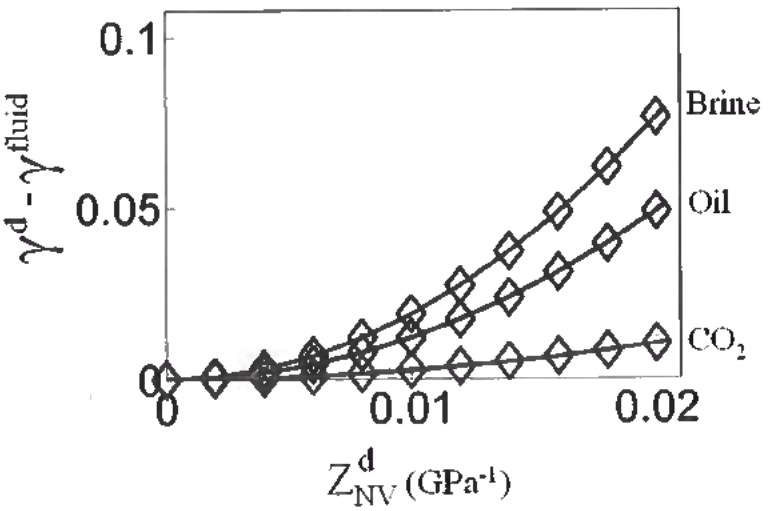

FIG. 4.6. Change in shear splitting between dry rock and rock saturated with CO_2, oil and brine for the same model considered in Figure 4.5.

single multicomponent survey in which the increase in γ was very well correlated with the known gas cap of the reservoir.

From time-lapse multicomponent data, Duranti et al. (1999) have also reported changes in γ that have been attributed to varying pore fluid compressibility during a CO_2 injection process. However, they observe changes on both S_1- and S_2-waves that result in a decrease of shear-wave splitting in CO_2-saturated regions instead of the increase shown in Figure 4.4b. The fact that they measure changes with saturation in the S_1-wave may indicate a more complex fluid substitution process than the one resulting from a single set of micro-corrugated fractures. In Chapter 7 it will be seen that the analysis of the S-wave data in Weyburn field, Canada, also suggests changes in the shear-wave splitting occurs after a CO_2 injection process.

4.5 One Set of Dipping, Rotationally Invariant Cracks in a VTI Background

Grechka and Tsvankin (2001) proved that a single set of dipping, rotationally invariant fractures embedded in a VTI background results in a monoclinic rock with vertical symmetry plane. Figure 4.7 illustrates the model in which the rotationally invariant cracks, originally with their normals in the X_1 direction, are rotated by the angle θ about the X_2 axis. After the rotation, the crack planes no longer contain the

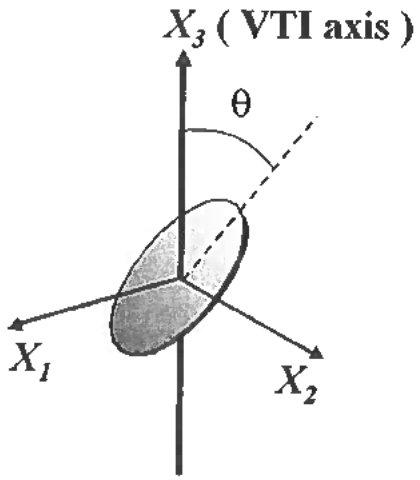

FIG. 4.7. Representation of a dipping, rotationally invariant crack in a VTI background.

symmetry axis of the background and the effective medium becomes monoclinic.

Schoenberg and Sayers (1995) have shown that the excess fracture compliance for a set of rotationally invariant fractures with their normals in the X_1 direction can be written as

$$S_f^{X_1} = \begin{pmatrix} Z_N & 0 & 0 & 0 & 0 & 0 \\ 0 & 0 & 0 & 0 & 0 & 0 \\ 0 & 0 & 0 & 0 & 0 & 0 \\ 0 & 0 & 0 & 0 & 0 & 0 \\ 0 & 0 & 0 & 0 & Z_T & 0 \\ 0 & 0 & 0 & 0 & 0 & Z_T \end{pmatrix}, \tag{4.9}$$

where Z_N and Z_T are the normal and tangential fracture compliances, respectively. To obtain the expression for dipping fractures, matrix (4.9) is rotated by the angle θ around the X_2 axis according to the Bond transformation represented by $S_f^\theta = N(\theta) S_f^{X_1} N^T(\theta)$. After the rotation of the fractures, the effective compliance of the monoclinic rock can be written as $S_{rock} = S_{VTI} + S_f^\theta$, where S_f^θ has the following non-zero terms:

$$S_f^\theta = \begin{pmatrix} S_{11} & 0 & S_{13} & 0 & S_{15} & 0 \\ 0 & 0 & 0 & 0 & 0 & 0 \\ S_{13} & 0 & S_{33} & 0 & S_{35} & 0 \\ 0 & 0 & 0 & S_{44} & 0 & S_{46} \\ S_{15} & 0 & S_{35} & 0 & S_{55} & 0 \\ 0 & 0 & 0 & S_{46} & 0 & S_{66} \end{pmatrix}. \tag{4.10}$$

Equation (4.10), shows that the effective compliance of the monoclinic rock has non-zero elements in the off-diagonal blocks defined in Figure 4.1a. Therefore, according to the arguments given above, the shear compliances will be sensitive to fluid saturation. Since this model is also monoclinic with a vertical symmetry plane, equations (4.5)-(4.7) are used to calculate the shear-wave splitting for the dry and brine-saturated cases.

To model the dry rock, VTI parameters measured on 18% porosity Berea sandstone are used for the background (Sarkar and Kranz, personal communication) and values of Z_N and Z_T that are consistent with Hudson's theory of penny-shaped cracks are considered. The parameters of the background rock are: $\epsilon = 0.07$, $\delta = 0.04$, $\gamma = 0.09$, $Vp_0 = 2.3$ Km/s and $Vs_0 = 1.62$ Km/s. For the crack compliances, it is assumed $Z_N \approx Z_T$ with $0 \leq Z_N \leq 0.02$.

Figure 4.8 shows that the changes in γ with saturation are larger with increasing dip angle of the cracks. If the dip is zero, the effective symmetry of the rock becomes orthorhombic and, since the off-diagonal block elements are zero, there is no change in γ with saturation. Also, when Z_N and $Z_T \to 0$ (limit of no cracks) the medium has the VTI symmetry of the background, and $\gamma = 0$. Note that the changes are larger when the normal compliance of the cracks increases, which indicates that larger S-wave sensitivity to fluids should be expected with increasing crack density.

For this model the same conclusion obtained for the micro-corrugated fractures holds: the splitting parameter increases with the compressibility of the saturating fluid. However, Figure 4.8 suggest that it would be hard to measure the changes in shear-splitting in the Berea sample. Similar to the case of the micro-corrugated fractures, a rock with large porosity ($\phi_i = 0.18$) will present meager changes in shear-splitting with saturation due to the influence of the large storage capacity.

Sayers (2002) has argued that a rock with two conjugate sets of dipping cracks in an isotropic background can present fluid dependent shear-wave splitting even if the rock is of orthorhombic symmetry. In the model proposed by Sayers, the rock is forced to be orthorhombic assuming that the cracks have identical fracture densities and that they are dipping exactly in opposite directions. However, Sayers' model implicitly disregards the pressure equilibrium between fracture sets, which violates the condition set by Brown and Korringa's theory. Two cracks that dip in opposite directions experience pore strains that are opposite in sign (Kachanov, 1992). This

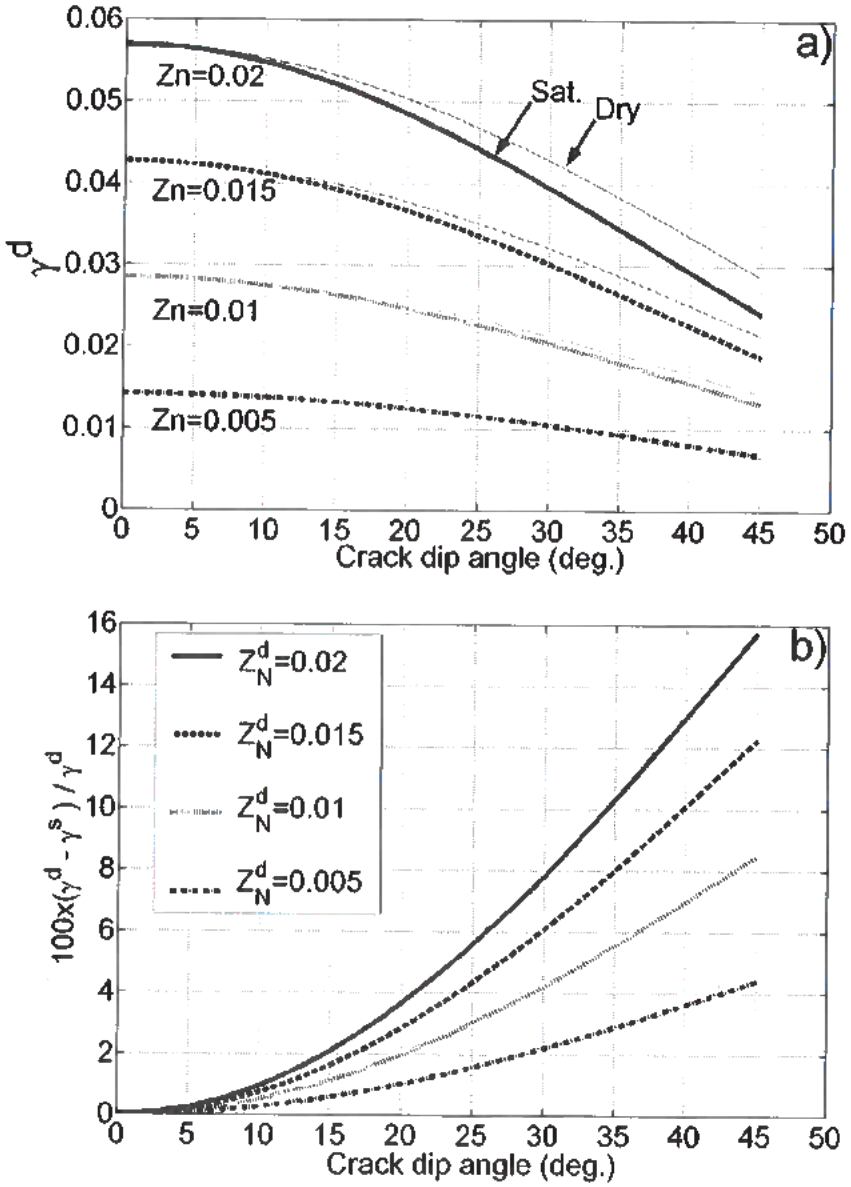

FIG. 4.8. Change of the splitting parameter with saturation as a function of the dip of the fractures for different values of the normal compliance of the dry fractures. (a) γ for dry (thin lines) and brine-saturated (thick lines) cases. Note that for all values of the normal compliance $\gamma^d > \gamma^s$. (b) Percent change in γ with saturation as a function of dip angle of cracks. Z_N is expressed in GPa^{-1}.

means that when a traction is applied to the rock, a crack dipping an angle θ from the vertical expands, while a crack dipping an angle $-\theta$ contracts by the same amount. If the cracks are connected, there is no effective change in the pore volume and, if the experiment is quasi-static, the fluids will move from one crack to the other without an increase in the pore pressure. Hence, no fluid effect will be observed in the shear-splitting for Sayers' (2002) orthorhombic rock *under conditions of pressure equilibrium.*

4.6 Two Vertical Sets of Non-Orthogonal Penny-Shaped Cracks in an Isotropic Background

The compliance matrix of a fractured rock composed of two sets of non-orthogonal, vertical fractures can be obtained in the same way as before by summing the compliances of the background and the fracture systems. Bakulin et al. (2000c) show that the effective symmetry of the medium is monoclinic with a horizontal symmetry plane and depends on eight parameters. These parameters are: the background velocities V_P and V_S, the compliances Z_N and Z_T of each fracture set, the angle χ between the sets and the azimuth of one of the sets (Figure 4.9).

Grechka et al. (2000) showed that the most convenient coordinate system to study this type of media is the one defined by the polarization directions of vertically traveling S_1- and S_2-waves. In this coordinate system, a generally monoclinic rock is characterized by nine anisotropic parameters defined in the same way as those for orthorhombic media plus three parameters that control the rotation of the P-, S_1- and S_2-wave NMO ellipses with respect to the coordinate axes. Therefore, a "diagnostic" feature of this type of fractured rocks is that the direction of polarization of the fast shear wave does not coincide with either axis of the NMO ellipses of P-, S_1- and S_2-waves.

For symmetries in which the off-diagonal block of the stiffness (and compliance) matrix is zero (HTI, VTI and orthorhombic) one of the axes of the NMO ellipses coincides with the polarization direction of the fast shear waves at vertical incidence. Non-zero elements in the off-diagonal block are responsible for the three extra parameters that are related to the three rotation angles β_P, β_{S_1} and β_{S_2} of the axes of the NMO ellipses with respect to the fast shear-wave polarization vector. From the discussion above it is clear that these rotation angles, which depend on terms in the off-diagonal stiffness (and compliance) blocks, should be sensitive to pore fluids.

The model is constructed by embedding two sets of penny-shaped cracks in the isotropic background. Then the rotation angles of the ellipses are calculated as a function of the angle between the sets, crack-density ratio and isotropic porosity. The calculations are performed for porous quartz, calcite and dolomite backgrounds.

Figure 4.10 shows the rotation angles of the NMO ellipses as a function of the

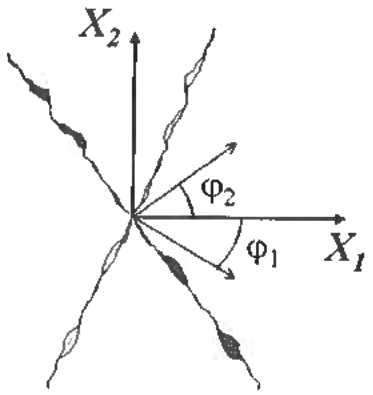

FIG. 4.9. Two sets of vertical fractures with the normals making the angles Φ_1 and Φ_2 with the X_1 direction. The angle between fracture sets is $\chi = \Phi_2 - \Phi_1$.

angle between the fracture sets (χ) for different lithologies, and its change when the rock is saturated with brine. In this case the isotropic porosity (ϕ_i) is fixed at 15% and the crack density ratio of the two sets is $\eta_{c2}/\eta_{c1} = 1/3$ with the dominating set's crack density $\eta_{c1} = 0.09$. In Figure 4.10a, when the angle between fracture sets is zero, the model becomes HTI and the angles β_i between the S_1 polarization direction and the axes of the NMO ellipses vanish. If the angle between sets is 90°, the model is orthorhombic and the β_i's again go to zero.

From Figure 4.10a it is clear that the largest change with saturation occurs for the orientation of the S_1-wave ellipse, while β_P and β_{S_2} remain almost unchanged. Therefore, Figure 4.10b shows the change in the S_1 mode alone; note that for the "softer", more compressible quartz matrix, the changes are larger than those for the stiffer dolomite.

Figure 4.11 shows the results for fixed isotropic porosity ($\phi_i = 0.15$), fixed angle between crack sets ($\chi = 55°$) and varying crack ratio η_{c2}/η_{c1}. In one extreme case, $\eta_{c2}/\eta_{c1} \to 0$, the crack density η_{c1} is dominant and the medium becomes HTI with all β_i's equal to zero. In the other extreme case, $\eta_{c2}/\eta_{c1} \to 1$, both fracture sets have the same crack density and the medium becomes orthorhombic with all β_i's equal to zero (Figure 4.11a).

The maximum value of the rotation angles and their largest change with saturation seems to occur when the dominant fracture set has approximately twice the

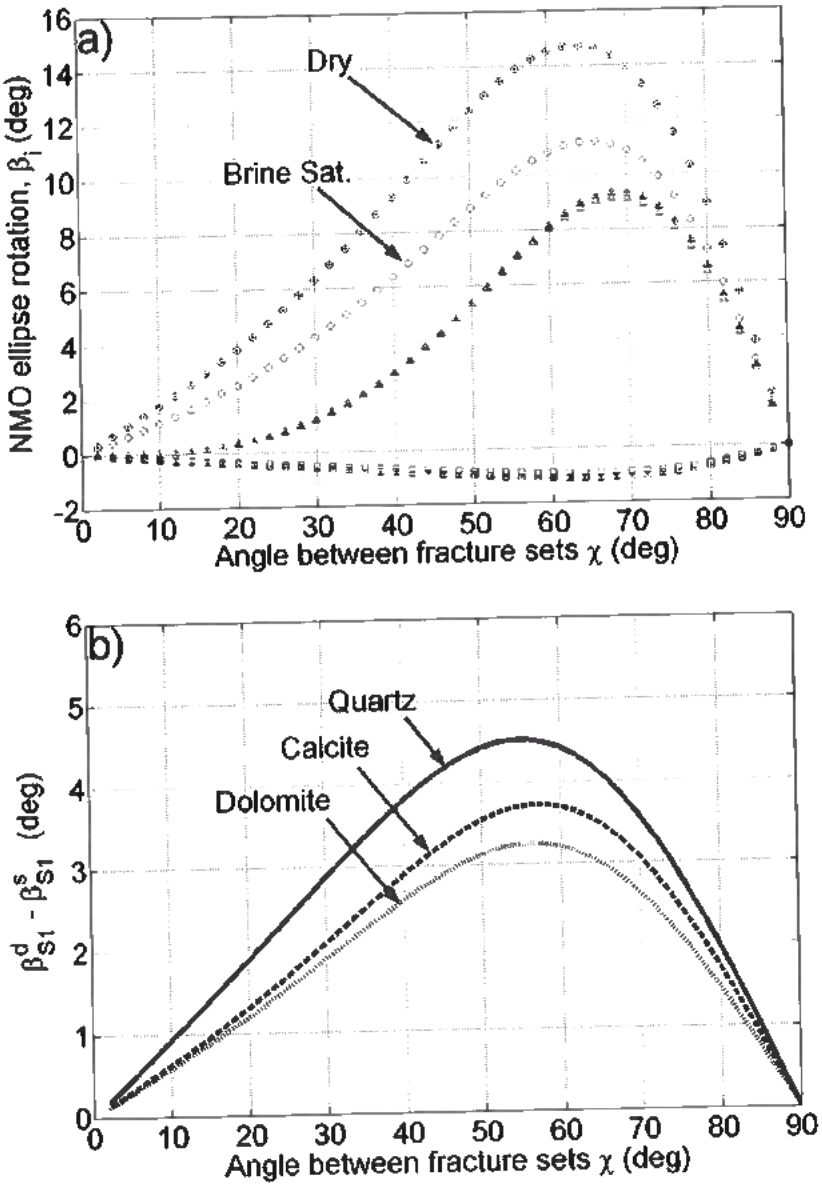

FIG. 4.10. (a) Rotation angles of the NMO ellipses for P waves (squares), S_1-waves (circles), and S_2-waves (triangles) as a function of the angle between the fracture sets (χ) for calcite background. Values for the dry rock are marked by a dot in the middle of the corresponding symbol. (b) Change in the rotation angle (β_{S_1}) of the S_1 NMO ellipse for quartz, calcite and dolomite backgrounds.

crack density of the weaker set. Again, the largest change with saturation occurs for the S_1-wave NMO ellipse (Figure 4.11a) and for the more compressible mineral material (Figure 4.11b).

In Figure 4.12, the change of the β_i's with saturation is computed as a function of the isotropic porosity (ϕ_i) of the background. The computation is done for a fixed angle between fracture sets ($\chi = 55°$) and a fixed crack-density ratio $\eta_{c2}/\eta_{c1} = 1/2$ with $\eta_{c1} = 0.09$.

Figure 4.12b shows that when ϕ_i decreases, the change of β_{S_1} with saturation decreases slightly and then increases as $\phi_i \rightarrow 0.01$. The increase at low values of ϕ_i seems counter-intuitive since one would expect to see smaller changes as the pore space available for fluid substitution decreases. However, this effect is due to the transition from a fluid substitution process dominated by the isotropic porosity to a process dominated by the crack porosity.

Bakulin et al. (2000c) have shown that β_P, β_{S_1} and β_{S_2} depend on the normal compliances (Z_N's) of both sets of penny-shaped cracks. Therefore, large changes in the normal compliances should produce large changes in the β_i's.

In Appendix E equation (4.2) is used to obtain an expression for the change of Z_N with saturation. This expression proves that as ϕ_i goes to zero (leaving only the crack porosity, ϕ_c), the combination of parameters governing the change in Z_N is $\frac{\phi_c}{K_f Z_N^d}$, where K_f is the bulk modulus of the fluid. If this ratio is small compared to unity the changes in Z_N are large. For reasonable values of the crack porosity, normal compliance and fluid bulk modulus this combination of parameters may be considerably smaller than one. For example, if $K_f = 2.25\ GPa$, $\phi_c = 10^{-3}$ and $Z_N^d = 0.02$, then $\frac{\phi_c}{K_f Z_N^d} = 0.022$. However, an important caveat is that this calculation applies to the changes one would expect from a dry rock to a 100% brine-saturated rock. More realistic fluid substitution processes will not occur between such extremes and the changes could be smaller.

4.7 Discussion and Conclusions

Under conditions of equilibrated pore pressures, I have shown that VTI, HTI, and non-tilted orthorhombic symmetry rocks have shear compliances (S_{44}, S_{55} and S_{66}) that are not dependent on fluid saturation. However, fractured rocks with monoclinic or lower symmetry have fluid-sensitive shear compliances. This conclusion is obvious when Brown and Korringa's equation is rewritten in two-index notation. Changes in the shear components only occur if off-diagonal elements of the compliance matrix in rows 4, 5 and 6 are non-zero.

Three different models of fractured rocks with monoclinic symmetry have been studied. Two of the monoclinic models have a vertical symmetry plane and they present vertical shear-wave splitting that is dependent on fluid saturation. The mon-

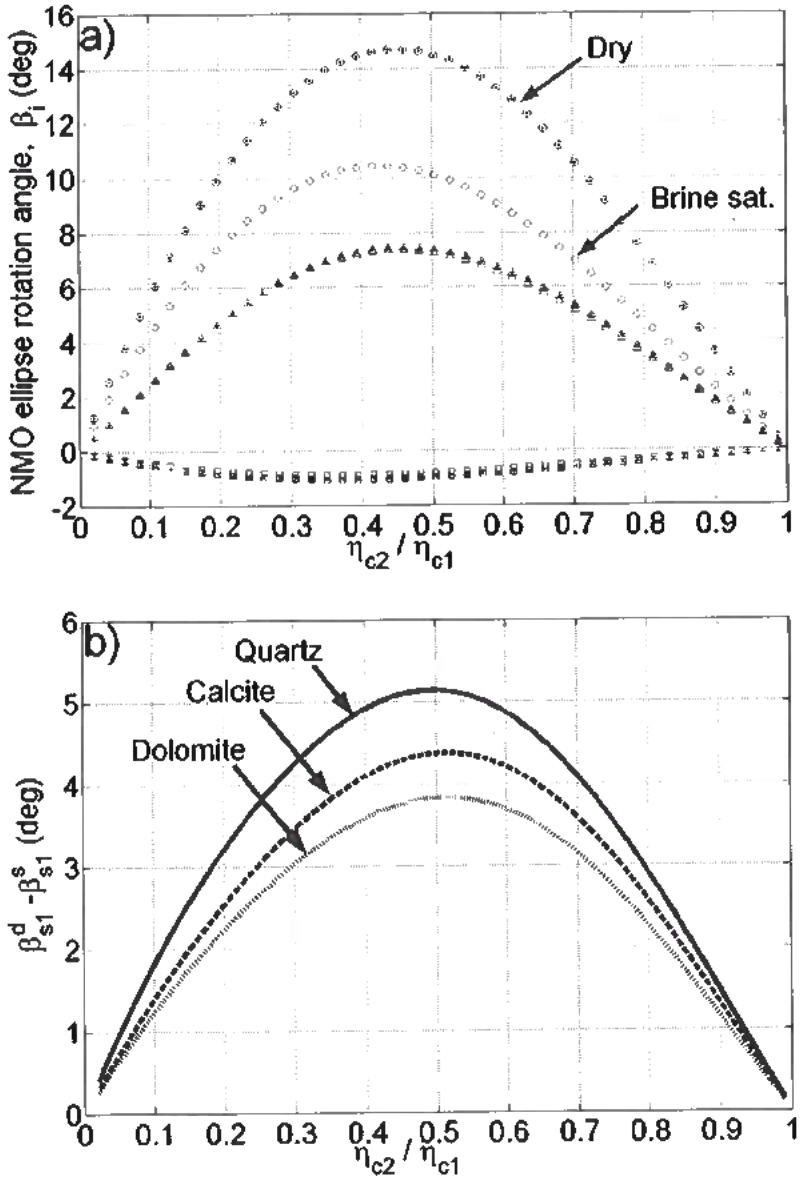

FIG. 4.11. (a) Rotation angles of the NMO ellipses for P waves (squares), S_1-waves (circles), and S_2-waves (triangles) as a function of the crack density ratio η_{c2}/η_{c1} for calcite background. Values for the dry rock are marked by a dot in the middle of the corresponding symbol. (b) Change in the rotation angle (β_{S_1}) of the S_1 NMO ellipse for quartz, calcite and dolomite backgrounds.

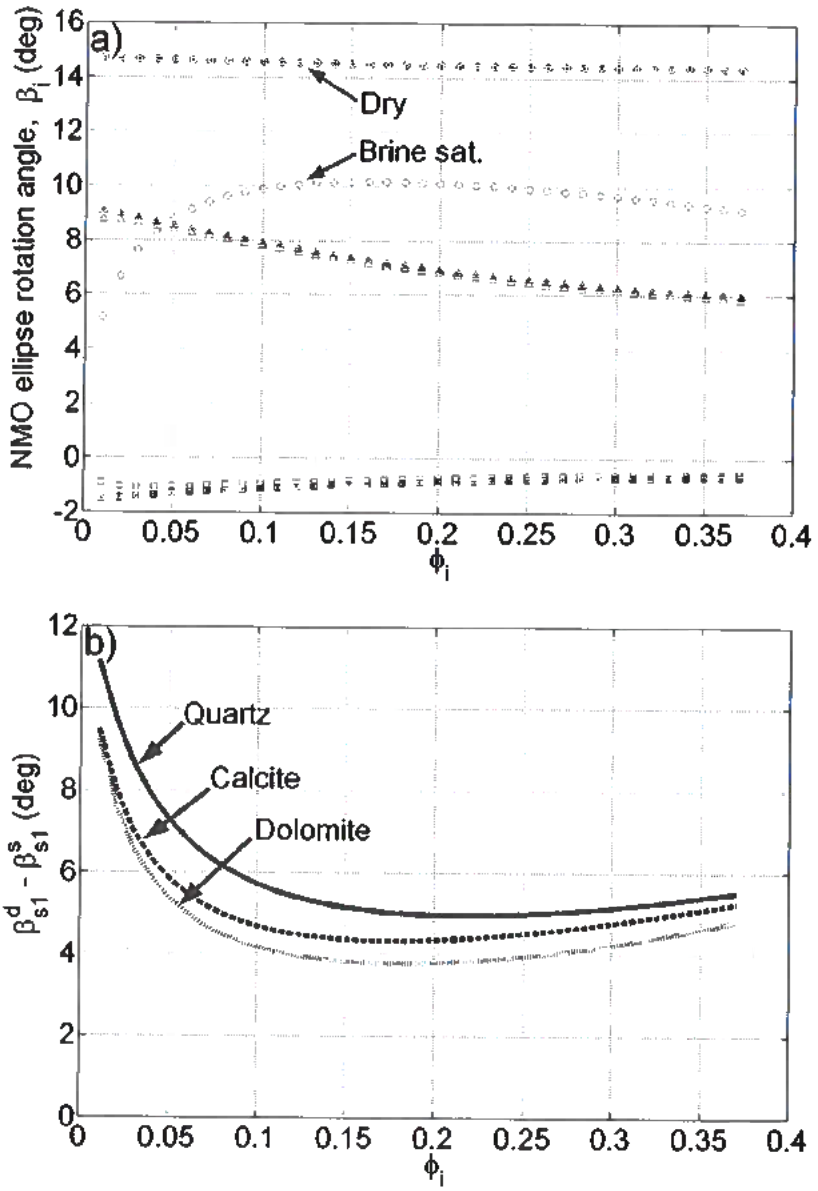

FIG. 4.12. (a) Rotation angles of the NMO ellipses for P waves (squares), S_1-waves (circles), and S_2-waves (triangles) as a function of the isotropic porosity ϕ_i (calcite background). Values for the dry rock are marked by a dot in the middle of the corresponding symbol. (b) Change in the rotation angle (β_{S_1}) of the S_1 NMO ellipse for quartz, calcite and dolomite backgrounds.

oclinic model with a horizontal symmetry plane does not exhibit fluid dependent splitting but the orientation of the S-wave NMO ellipses changes with saturation.

The two models with vertical symmetry planes contained a single set of parallel micro-corrugated fractures and a set of dipping cracks in a VTI background, respectively. Both models support the conclusion that the splitting of vertically traveling S-waves increases with the compressibility of the saturating fluid. These variations may be observed after gas injection into water- or oil-saturated sections of the reservoir, or after water encroachment due to production in a zone originally saturated with gas.

The monoclinic rock with a horizontal symmetry plane contained two sets of non-orthogonal penny-shaped cracks in an isotropic background. For this model, except for density effects, vertically traveling shear waves are not sensitive to saturation changes. However, the NMO ellipses of the three pure modes (P, S_1 and S_2), in particular S_1, are sensitive to the pore-fluid content. Analysis for different lithologies indicates that larger changes in the orientation of the S_1-wave NMO ellipse with saturation should be expected for fractured rocks with a softer background matrix (e.g., quartz instead of dolomite).

An important point is whether it is possible to measure from seismic data the changes with saturation in splitting parameter that have been modeled in this chapter. The results presented here indicate that the changes should be larger in rocks with small isotropic porosity. An important caveat, however, is that in the models presented above the isotropic porosity refers to the pores that are actually connected in the rock. In real rocks it is possible to have sections of the pore space that are effectively disconnected from the portion of the pores where the fluid substitution occurs. In these cases the total porosity measured from a wireline tool maybe much larger than the actual connected porosity that accounts for the pressure equilibrium. Hence, if the *connected* isotropic porosity is small, most of the fluid substitution will occur in the fractures and the variations in splitting parameter will be larger (i.e. $\phi_i \rightarrow 0$ in equation (4.2)).

Equations (D.8), (D.9) and (E.3) indicate that if $\phi_i = 0$ the magnitude of the changes in the fracture compliances is determined by $\frac{\phi_c}{K_f Z_N^d}$. If this combination of parameters is small compared to unity larger changes with saturation can be expected in the fracture compliances and in the shear-splitting parameter . Using reasonable values of the crack porosity, normal compliance and the bulk modulus of water (i.e. $\phi_c = 10^{-3}$, $Z_N^d = 0.02$, and $K_f = 2.25\ GPa$) $\frac{\phi_c}{K_f Z_N^d} = 0.022$, which is considerable smaller than unity.

Except for density effects, few cases of shear-wave velocity dependence on saturation have been reported in the literature. This is probably due to the small number of multicomponent, time-lapse experiments that have been acquired over fractured reservoirs. Since, not all the theories and assumptions presented in this chapter have

been tested it is important to design experiments on fractured rocks where the fluid dependence of shear-waves with saturation can be studied.

Due to the uncertainties in the fracture parameters of natural rocks it is convenient to conduct experiments on synthetic rocks for which all the parameters are well known. Rathore et al. (1994) manufactured a synthetic sandstone with epoxy-cemented sand in which metallic discs of known shape were embedded in successive layers. The discs were then leached out chemically leaving cracks of known geometry that generated a rock with transversely isotropic symmetry.

The same technique could be applied to build a monoclinic rock with two sets of non-orthogonal penny-shaped cracks. In this case the metal discs could be placed at a fixed angle in thin slabs of synthetic sandstone. Then the rock could be built by compressing several slabs together.

Another alternative is to follow the model of tilted rotationally invariant cracks in a TI background proposed by Grechka and Tsvankin (2001). First, the rock could be built following Rathore's method to obtain one set of cracks. Then, the rock would be stressed with the maximum compressive direction at an angle from the crack normals. This will generate a second set of stress-induced cracks and make the symmetry of the rock monoclinic. However, the disadvantage of this method is that the shape and distribution of the cracks will not be known.

Once the sample is built, velocity measurements can be done for propagation parallel to the symmetry plane and out of the symmetry plane. Out-of-plane velocity measurements should give NMO ellipses whose orientation depend on saturation. Velocity measurements of shear-waves propagating in the plane of symmetry should be fluid dependent.

Chapter 5

INTEGRATING PRESSURE-TRANSIENT DATA INTO SEISMIC RESERVOIR CHARACTERIZATION

5.1 Introduction

Pressure-transient experiments performed by engineers perturb the pore pressure of the reservoir and test the compliance of the rock's pores. Seismic experiments performed by geophysicist perturb the confining pressure and test the compliance of the bulk rock volume. Because elasticity theory provides relations between the pore and bulk compressibilities, well test and seismic data analysis can be used jointly to characterize the elasticity of the reservoir rocks.

Well test analysis is the generic name given to the study of pressure and flow-rate data measured at the well location. If Darcy's law is valid and the rock behaves elastically, the diffusion equation describes fluid flow through the reservoir, providing estimates of storage capacity, average permeability and average pressure, Da Prat (1990). The condition of elasticity inherent in the diffusion equation links well test measurements to the pore space compressibility of the rock. Since the compressibility of the pore space is a function of the mineral modulus and dry bulk modulus of the rock Zimmerman (1991), well test measurements can be related to some of the elastic parameters that are estimated from seismic data. Therefore, well test analysis can provide a quantitative link between geophysical and engineering measurements that is useful for reservoir characterization.

Both well test and seismic propagation analysis suffer from non-uniqueness of the solutions that model a given reservoir. By estimating some of the elastic parameters of the rock from both a flow experiment and seismic data, one can reduce the non-uniqueness of the solutions by correlating the outcome of the two independent analyses.

In this chapter, Zimmerman's (1991) rock compressibility relations are used to show how the rock's storage capacity is a function of the mineral and dry rock compressibility. If the rock is isotropic, storage capacity estimates from pressure-transient tests can be used in Gassmann's (1951) equations to predict changes in the bulk modulus of the rock with saturation, *without knowing the fluid compressibility and the rock porosity.* If the rock is fractured and anisotropic, the application of Schoenberg's linear slip theory (Schoenberg and Douma, 1988; Schoenberg and Sayers, 1995) yields a relation between the normal compliance of the fracture system and the ratio of

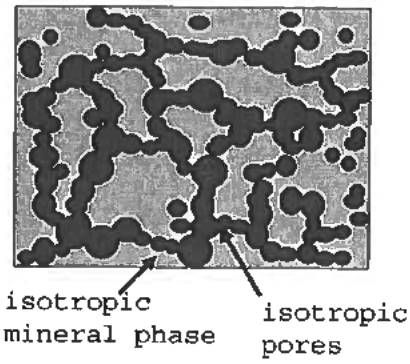

FIG. 5.1. Schematic representation of an isotropic, single porosity rock. The ISP rock may be modeled assuming the pores are all spherical or of arbitrary shape with random orientations.

the fracture storage capacity to total rock storage capacity (storage capacity ratio). Since the normal compliance of the fracture system may be estimated from seismic data Bakulin et al. (2000a), and the storage capacity ratio can be measured from well test data, the derived relation allows a quantitative comparison between independent experiments.

The theory developed for the fractured anisotropic rock is applied to the analysis of pressure-transient data from Weyburn field with the objective of constraining the value of the normal fracture compliance in the area around the well where the test was performed. Assuming an ideal shape of the fractures in the reservoir, the fracture density and porosity are estimated from the storage capacity ratio.

Even though there exists a variety of methods and experiments from which formation storage capacity can be estimated (Lee, 1982; Da Pratt, 1990), this chapter will concentrate on single well, pressure-transient analysis in which the well is produced at a constant rate. However, the link between the well test parameters and the rock's elastic parameters will be valid for any other type of well test experiment.

5.2 Part I: Isotropic Single Porosity Rock

The first model to be considered is defined as the *isotropic, single porosity* (ISP) rock, which is composed of a mineral phase and a single porous phase. The mineral phase is assumed to be elastically isotropic and homogeneous, and the pores are assumed to be randomly oriented. This condition implies that the porous rock will be elastically *isotropic* and that it can be modeled as a collection of spherical pores or randomly oriented pores in an isotropic background material (see Figure 5.1).

The flow properties of the isotropic, single porosity rock, require that all the pores that account for the flow account for the storage capacity of the rock. This means that the storage capacity measured from a flow experiment corresponds to the connected pores of the rock. The storage capacity contains information about the pore and fluid compressibility, providing the link between the well test experiment and the elasticity of the rock.

5.2.1 Measuring the storage capacity

In the ISP rock, the pressure variation (Δp) with time (t) is described by the diffusion equation assuming the flow is single phase, that Darcy's law holds, and the fluid is slightly compressible. In radial coordinates the diffusion equation can be written as

$$\frac{\kappa_i}{\mu}\frac{1}{r}\frac{\partial}{\partial r}\left(r\frac{\partial \Delta p}{\partial r}\right) = \phi_i c_i \frac{\partial \Delta p}{\partial t}, \tag{5.1}$$

where μ is the fluid viscosity, κ_i is the rock's permeability and ϕ_i is the porosity, with the subscript i indicating these properties are measured on an elastically isotropic rock. c_i is the total compressibility of the isotropic pore/fluid system which can be expanded as

$$c_i = \frac{1}{K_f} + c_{pp,i}, \tag{5.2}$$

where K_f is the fluid bulk modulus, and $c_{pp,i}$ is the pore space compressibility of the isotropic pores.

The first term in equation (5.2) is the fluid's contribution to the total compressibility of the pore/fluid system. The second term ($c_{pp,i}$) reflects the excess pore fluid that can be stored in the pore space (V_p) due to an increase in the pore pressure (p_p) at a constant confining pressure (p_c),

$$c_{pp,i} = \frac{1}{V_p}\left(\frac{\partial V_p}{\partial p_p}\right)_{p_c}. \tag{5.3}$$

The product of the porosity and the total pore/fluid system compressibility ($\phi_i c_i$) is defined as the storage capacity of the reservoir rock, which can be estimated from the well test data analysis based on the solution of equation (5.1) (see Appendix F). Since the storage capacity has information about porosity (ϕ_i), fluid compressibility ($1/K_f$) and pore space compressibility($c_{pp,i}$), I show below that it can be used to analyze the changes in seismic wave velocity through the rock with different fluid saturations.

5.2.2 Storage capacity and the fluid substitution problem

One of the objectives of rock physics, is to predict the changes in the velocity of a seismic wave due to changes in the fluid saturation of the rock. This fluid substitution problem can be addressed by finding equations that predict the velocities of the wave propagating through a saturated rock (saturated rock velocities) from the velocities of the wave propagating through the dry rock (dry rock velocities).

Gassman's (1951) equations predict the saturated rock velocities from the dry rock velocities under the assumption that the rock is isotropic, monomineralic and that the pore pressure is equilibrated throughout the pore space. Therefore, Gassman's equations are applicable to the ISP rock model defined above, for which the storage capacity of the rock ($\phi_i c_i$) can be measured from pressure-transient analysis. For an isotropic rock, the wave velocities are determined by the bulk (K) and shear (G) moduli and the bulk rock density (ρ). Gassman's (1951) equations for the change in K and G are

$$\frac{1}{K_s} = \frac{1}{K_{d,i}} - \frac{\left(\frac{1}{K_{d,i}} - \frac{1}{K_m}\right)^2}{\left(\frac{1}{K_f} - \frac{1}{K_m}\right)\phi_i + \left(\frac{1}{K_{d,i}} - \frac{1}{K_m}\right)}, \tag{5.4}$$

$$G_s = G_d, \tag{5.5}$$

where K_m is the bulk modulus of the mineral material, the "d, i" subscripts stand for measurement done on the dry, isotropic rock and the "s" subscript stands for a measurement done on a rock saturated with a fluid with bulk modulus K_f.

One of the problems in applying equations (5.4) and (5.5) to seismic data is that the prediction of K_s depends on the parameters K_f, ϕ_i, $K_{d,i}$ and K_m, which are usually estimated from well logs and cores at a much smaller scale than seismic scale. However, the scale of measurement of the storage capacity estimated from pressure-transient tests is determined by the drainage radius which can be of the order of tens to hundreds of meters. Therefore, the introduction of storage capacity into Gassmann's equation could provide estimates of K_s that are more consistent with the seismic scale of measurement.

In monomineralic, porous rocks, the existence of two different volumes (bulk and pore volumes) and two different pressures (pore and confining pressures) results in four rock compressibilities Zimmerman (1991). Each of these compressibilities relates changes in either the bulk volume (V_b) or pore volume (V_p) to changes in the confining pressure (p_c) or pore pressure (p_p), and are defined as:

$$c_{bc} = \frac{-1}{V_b}\left(\frac{\partial V_b}{\partial p_c}\right)_{p_p} \equiv \textit{dry bulk compressibility},$$

$$c_{bp} = \frac{1}{V_b}\left(\frac{\partial V_b}{\partial p_p}\right)_{p_c} \equiv \textit{subsidence compressibility},$$

$$c_{pc} = \frac{-1}{V_p}\left(\frac{\partial V_p}{\partial p_c}\right)_{p_p} \equiv \textit{compaction compressibility},$$

$$c_{pp} = \frac{1}{V_p}\left(\frac{\partial V_p}{\partial p_p}\right)_{p_c} \equiv \textit{pore compressibility}. \tag{5.6}$$

The pore compressibility c_{pp} is the second term in the expression of the total pore/fluid system compressibility in equation (5.2) and c_{bc} is the inverse of the dry rock bulk modulus ($K_{d,i}$). As shown in Chapter 2, c_{pp} can be expressed as a function of $K_{d,i}$, ϕ_i and K_m as

$$c_{pp} = \left(\frac{1}{K_{d,i}} - \frac{1+\phi_i}{K_m}\right)\frac{1}{\phi_i}. \tag{5.7}$$

Substituting equation (B.5) into the definition of c_i in equation (5.2), the storage capacity of the reservoir is

$$\phi_i c_i = \left(\frac{1}{K_f} - \frac{1}{K_m}\right)\phi_i + \left(\frac{1}{K_{d,i}} - \frac{1}{K_m}\right). \tag{5.8}$$

Comparison of equations (5.8) and (5.4) shows that the denominator on the right side of equation (5.4) is the storage capacity of the rock. Therefore, the storage capacity measured from the well test experiment can be used to rewrite Gassman's equation (5.4) as

$$\frac{1}{K_s} = \frac{1}{K_{d,i}} - \frac{\left(\frac{1}{K_{d,i}} - \frac{1}{K_m}\right)^2}{\phi_i c_i}. \tag{5.9}$$

This equation highlights the benefit of adding the information provided by the pressure-transient analysis. The advantage of expression (5.9) over the Gassmann's equation is that *no assumptions* are needed about the values of the fluid bulk modulus or formation porosity to calculate K_s because they are included in the storage capacity, $\phi_i c_i$. However, it is still necessary to have estimates of the mineral and dry rock bulk moduli.

From an estimate of the bulk modulus of the rock saturated with a fluid having bulk modulus K_{f1} (e.g. from estimates of P-, S-wave velocities and density), equation (5.9)can be used to predict the change in the bulk modulus caused by substitution of a second fluid (K_{f2}). This requires a time-lapse well test experiment with one pressure-transient test done with the original fluid and a second after the fluid

substitution (e.g. after production or a fluid injection process). In this scenario, the storage capacity estimated from the first test $[(\phi_i c_i)_1]$ would be used with the estimate of saturated bulk modulus (K_{s1}) to calculate $(K_{d,i})$ according to

$$\frac{1}{K_{d,i}} = \frac{1}{K_m} + \frac{(\phi_i c_i)_1}{2}\left[1 - \sqrt{1 - \frac{4(\frac{1}{K_{s1}} - \frac{1}{K_m})}{(\phi_i c_i)_1}}\right]. \tag{5.10}$$

Then, the estimated $K_{d,i}$ can be substituted in equation (5.9), with the storage capacity estimated from the second pressure-transient test $[(\phi_i c_i)_2]$, to predict the new saturated rock bulk modulus (K_{s2}).

An important observation is that equation (5.9) predicts that the change in the saturated rock compressibility $(1/K_s)$ is proportional to the change in the inverse of the storage capacity i.e.

$$\Delta\left(\frac{1}{K_s}\right)_{21} = -\left(\frac{1}{K_{d,i}} - \frac{1}{K_m}\right)^2 \Delta\left(\frac{1}{\phi_i c_i}\right)_{21}, \tag{5.11}$$

where

$$\Delta\left(\frac{1}{K_s}\right)_{21} = \frac{1}{K_{s2}} - \frac{1}{K_{s1}},$$

$$\Delta\left(\frac{1}{\phi_i c_i}\right)_{21} = \frac{1}{(\phi_i c_i)_2} - \frac{1}{(\phi_i c_i)_1}.$$

If seismic and pressure-transient experiments are performed and then repeated after a fluid substitution process, the proportionality shown in equation (5.11) will hold if the fluid substitution process does not change $(\frac{1}{K_{d,i}} - \frac{1}{K_m})$. In Chapter 2 it was shown that

$$c_{pc,i}\phi_i = \frac{1}{K_{d,i}} - \frac{1}{K_m}, \tag{5.12}$$

where $c_{pc,i}$ is the compaction compressibility defined in equation (5.6). Therefore, the proportionality will hold if pressure changes in the reservoir during the well test experiment are not high enough to alter the porosity or compaction compressibility of the reservoir. This should hold true for most well compacted reservoir rocks.

5.3 Part II: Anisotropic Double Porosity Rock

The second model is the *anisotropic, double porosity* (ADP) rock, which is composed of an isotropic, homogeneous mineral phase and two porous phases. The two

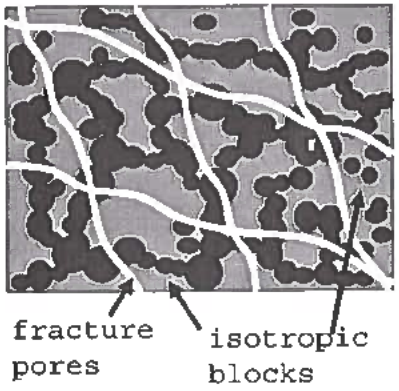

FIG. 5.2. Schematic representation of the anisotropic, double porosity rock. The rock is composed of elastically isotropic blocks separated by fractures.

different pore types will be referred to as the *isotropic pores* and the *fracture pores*, respectively. The first type of pores are deemed *"isotropic"* because their inclusion in the mineral phase does not render the rock anisotropic. These may be thought of as pores of arbitrary shape that are randomly oriented as in the case of the ISP model discussed before. On the other hand, the fractures are assumed to be low aspect ratio pores that have preferential orientations and make the rock elastically anisotropic. It will also be assumed that the internal structure of the ADP rock can be described as a group of isotropic blocks, where the isotropic pores reside, that are separated by the network of through-going fractures as shown in Figure 5.2.

With regard to flow properties, the isotropic pores have most of the storage capacity of the rock but have small permeability. Flow can occur between isotropic pores and fractures but flow into the wellbore occurs only through the fracture network. In well test analysis this is called the double porosity model (Barrenblatt et al., 1960; Warren and Root, 1963).

As in the single porosity rock, the link between pressure-transient analysis and the rock's elasticity is in the storage capacity. However, in this model the parameter that can be measured is the ratio of the fracture system storage capacity to the total storage capacity of the rock (storage capacity ratio) which is defined as

$$\omega = \frac{\phi_F c_F}{\phi_F c_F + \phi_i c_i}, \tag{5.13}$$

where $\phi_F c_F$ is the storage capacity of the fracture pores and $\phi_F c_F + \phi_i c_i$ is the total storage capacity of the rock.

5.3.1 Measuring the storage capacity ratio, ω

In the ADP rock, the pressure variation (Δp) with time (t) is also described by the diffusion equation. However, the presence of two pore types with different storage and flow capacities requires the definition of two differential equations Da Prat (1990). The first differential equation describes the flow through the fracture network into the wellbore, which can be written in radial coordinates as

$$\frac{\kappa_F}{\mu}\frac{1}{r}\frac{\partial}{\partial r}\left(r\frac{\partial \Delta p_F}{\partial r}\right) = \phi_F c_F \frac{\partial \Delta p_F}{\partial t} + \phi_i c_i \frac{\partial \Delta p_i}{\partial t}, \tag{5.14}$$

where μ is the fluid viscosity, κ and ϕ are the permeability and porosity, respectively, with the subscript "F" indicating fracture pores and the subscript "i" indicating isotropic pores. c_F and c_i are the compressibilities of the fracture and isotropic pore systems, respectively.

Two pressure variations are indicated in equation (5.14), one in the fractured pore system (Δp_F) and one in the isotropic pore system (Δp_i). Since flow into the wellbore occurs only through the fracture network, the second term on the right side of equation (5.14) represents the volume of fluid flowing from the isotropic pores into the fracture system. The rate of flow into the fracture system is determined by the pressure differential between isotropic and fracture pores ($\Delta p_F - \Delta p_i$) and the permeability of the isotropic pores (κ_i). Therefore, the second differential equation is

$$\phi_i c_i \frac{\partial \Delta p_i}{\partial t} = \frac{\kappa_i}{\mu}\frac{(\Delta p_F - \Delta p_i)}{L^2}, \tag{5.15}$$

where L is the characteristic length of the isotropic rock block.

From well test data analysis based on the solution of differential equations (5.14) and (5.15), it is possible to estimate the storage capacity ratio (see Appendix G). The ω parameter includes information about the fracture porosity and fracture pore space compressibility that links well test experiments with elastic parameters that can be estimated from seismic data.

5.3.2 ω parameter and normal fracture compliances

When fractures are introduced into an isotropic porous rock, the overall compressibility of the rock increases due to the excess compliance associated with the fracture system (Schoenberg and Sayers, 1989). Therefore, the compressibility of a dry fractured rock is

$$\frac{1}{K_{d,(i+f)}} = Z_{NF} + \frac{1}{K_{d,i}}, \tag{5.16}$$

where Z_{NF} is the normal compliance of the dry fracture system, $K_{d,i}$ is the dry bulk modulus of the isotropic part of the rock, and $K_{d,(i+f)}$ is the dry bulk modulus of the whole rock, which includes both isotropic and fracture pores.

If the storage capacity ratio can be expressed in terms of the dry rock compressibility (5.16), it will also be a function of the normal compliance of the fracture system, Z_{NF}. Because estimates of Z_{NF} can be obtained from seismic data for some types of fractured rocks Bakulin et al. (2000a), having ω as a function of the Z_{NF} implies it may be possible to obtain estimates of the normal fracture compliance (Z_{NF}) from pressure-transient analysis or estimates of storage capacity ratio (ω) from seismic data analysis.

The derivations presented in Appendix H show that the ω parameter can be written as

$$\omega = \frac{\left(\frac{1}{K_f} - \frac{1}{K_m}\right)\phi_F + \left(\frac{1}{K_{d,(i+f)}} - \frac{1}{K_{d,i}}\right)}{\left(\frac{1}{K_f} - \frac{1}{K_m}\right)\phi_t + \left(\frac{1}{K_{d,(i+f)}} - \frac{1}{K_m}\right)}, \tag{5.17}$$

where $\phi_t = \phi_i + \phi_F$. Inserting equations (5.12) and (5.16) into equation (5.17), ω is expressed as a function of the normal fracture compliance Z_{NF} as

$$\omega = \frac{\left(1 - \frac{K_f}{K_m}\right)\phi_F + K_f Z_{NF}}{\left(1 - \frac{K_f}{K_m}\right)\phi_t + K_f Z_{NF} + K_f c_{pc,i}\phi_i}. \tag{5.18}$$

The disadvantage of expression (5.18) is that it has too many parameters, few of which are known in practice. However, it is possible to find approximations that will simplify the expression for ω in the limiting cases of very incompressible fluids ($K_f \rightarrow 3\ GPa$) or in the case of very compressible fluids ($K_f \rightarrow 0\ GPa$). The first approximation, which is reasonable for most fluids and mineral components is to consider that $1 - K_f/K_m \approx 1$, e.g. even for a "stiff" fluid ($K_f = 3$ GPa) and a "soft" mineral ($K_m \approx 40$ GPa), $1 - K_f/K_m \approx 0.94$.

Under the previous approximation equation (5.18) can be written as

$$\omega \approx \frac{\phi_F + K_f Z_{NF}}{\phi_t + K_f\left(Z_{NF} + c_{pc,i}\phi_i\right)}. \tag{5.19}$$

The previous expression can be simplified further if the reservoir fluid is a gas at low effective pressures ($K_f \rightarrow 0\ GPa$), in which case equation (5.19) yields

$$\omega \rightarrow \frac{\phi_F}{\phi_t}. \tag{5.20}$$

This simple expression indicates that storage capacity ratios measured from pressure-transient tests on gas-producing wells could give estimates of the ratio of fracture porosity to total porosity in the reservoir.

For wells producing stiff fluids, $K_f \rightarrow 3\ GPa$, stronger assumptions are required to simplify further equation (5.19). If the fracture porosity is small compared to the $K_f Z_{NF}$ and the fracture compliance is large compared to the compressibility of the isotropic pores, equation (5.19) can be written as

$$\omega \approx \frac{K_f Z_{NF}}{\phi_t + K_f Z_{NF}}. \tag{5.21}$$

The validity of this approximation will depend on the type of fractures and the type of isotropic pores. For stiff spherical pores the compaction compressibility $c_{pc,i}$ is small enough to justify the approximation.

The advantage of expressions (5.20) and (5.21) is that they can be used to predict the values of ϕ_F or Z_{NF} from estimates of ω, provided that ϕ_t and K_f are known. Alternatively, equation (5.21) can be used to estimate ω from seismically derived values of Z_{NF}. Since ω is one of at least three parameters that must be estimated from pressure-transient analysis (Appendix G), seismically derived values of ω can be helpful to constrain the parameter inversions done by the well test engineer.

Information about the fracture density of the rock (η_F) can be extracted from equation (5.21) assuming a specific micro-structural description of the fractures. If the fracture pores behave elastically as penny-shaped cracks, Z_{NF} is Bakulin et al. (2000a)

$$Z_{NF} = \frac{A_N \eta_F}{M_i \left(1 - A_N \eta_F\right)}, \tag{5.22}$$

where

$$A_N = \frac{4}{3\frac{V_{Pi}}{V_{Si}}\left(1 - \frac{V_{Pi}}{V_{Si}}\right)}, \tag{5.23}$$

M_i is the P-wave modulus of the isotropic background rock, and V_{Pi} and V_{Si} are the P- and S-wave velocities of the isotropic background rock. Furthermore, the fracture density (η_F) is a function of the fracture porosity and the fracture aspect ratio (α_F):

$$\eta_F = \frac{3\phi_F}{4\pi\alpha_F}. \tag{5.24}$$

Note that equations (5.21)-(5.24), make it possible to estimate the fracture density and fracture porosity from ω. However, this requires *strong* assumptions about the

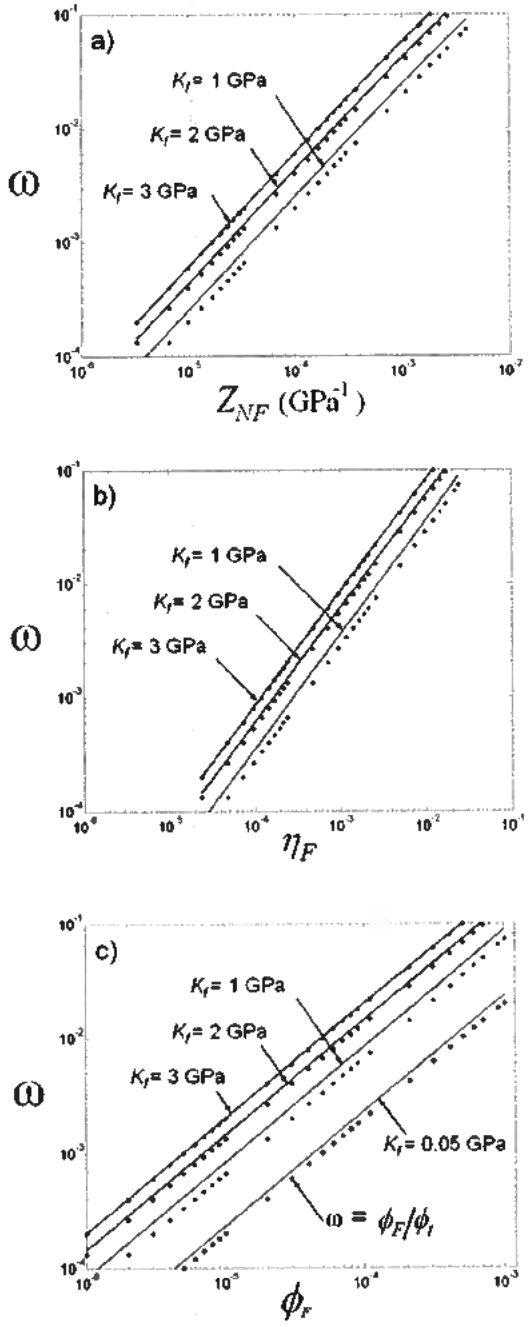

FIG. 5.3. ω plots for different values of K_f and $\phi_t = 0.05$. Solid lines are the exact result from equation (5.18) and dots show the approximation (5.21). (a) ω vs. Z_{NF} (b) ω vs. η_F, with the fracture compliance calculated from equations (5.22) and (5.23) assuming a calcite mineral matrix. (c) ω vs. ϕ_F, assuming a crack aspect ratio of 0.01. Also indicated is the continuous line showing how the approximation $\omega \approx \phi_F/\phi_t$ is good for low fluid bulk modulus values.

geometry of the fractures.

Figures 5.3a-5.3c show the exact (solid lines) and approximate (dots) results of ω versus fracture compliance, fracture density and fracture porosity for a rock with a total porosity $\phi_t = 0.05$. The exact curves in Figure 5.3b are calculated for a calcite mineral and spherical isotropic pores, and a fracture aspect ratio $\alpha_F = 0.01$ is used in Figure 5.3c.

The approximate equation (5.21) becomes more accurate for larger values of the fluid bulk modulus in all three plots. Figure 5.3c shows that the approximation (5.20) is better for fluids with bulk modulus less than 0.05 GPa, indicating that well test analysis in gas-producing fractured formations could give estimates of the ratio of fracture porosity to total porosity.

In practice, estimating the fracture to total porosity ratio from a gas well using equation (5.20) is the procedure with least number of assumptions. In water producing wells, estimating the fracture compliance (Z_{NF}) involves the fewest assumptions; ω is provided by the well-test analysis, K_f can be measured on fluid samples, and ϕ_t can be estimated from well log porosity measurements. Calculating fracture density requires estimates of M_i, V_{Pi} and V_{Si} of the background isotropic rock. Finally, estimates of the fracture porosity from the water producing well requires knowledge of all of the above parameters plus the fracture aspect ratio.

5.4 Analysis of Weyburn Field Data

As described in Chapter 1, Weyburn field is a carbonate reservoir consisting of a 30 m interval of dolomite and limestone. There is extensive proof from production, core, and borehole data that the reservoir is fractured. Figure 5.4 shows pressure data acquired at one of the wells during a pressure build-up test. Since the well is mainly a water producer (oil/water ratio = 2 %), it is ideal for applying equation (5.21) to calculate the normal fracture compliance from the ω estimate.

Data preparation, quality control, and analysis was done using the commercial software *Saphire*. The PVT data were taken from the model provided by the field operator, and all the fluids' information was taken from data acquired in a well 200 m away from the test well.

The inversion algorithm gives estimates of wellbore storage (C), skin parameter (S), initial pressure (p_{ini}), flow capacity ($\kappa_F h$), and ω and λ parameters (See Appendices A and C for definitions). Figure 5.5 shows four model curves from four inversion trials with widely different starting set of parameters. Table 1 summarizes the inversion results for four trials and shows that the wellbore storage (C) and storage capacity ratio (ω) are the most stable estimates.

Based on the average of the storage ratios presented in Table 1 ($\omega = 0.042$), the compressibility of a fluid mixture based on the well's water cut (98 % water, 2 %

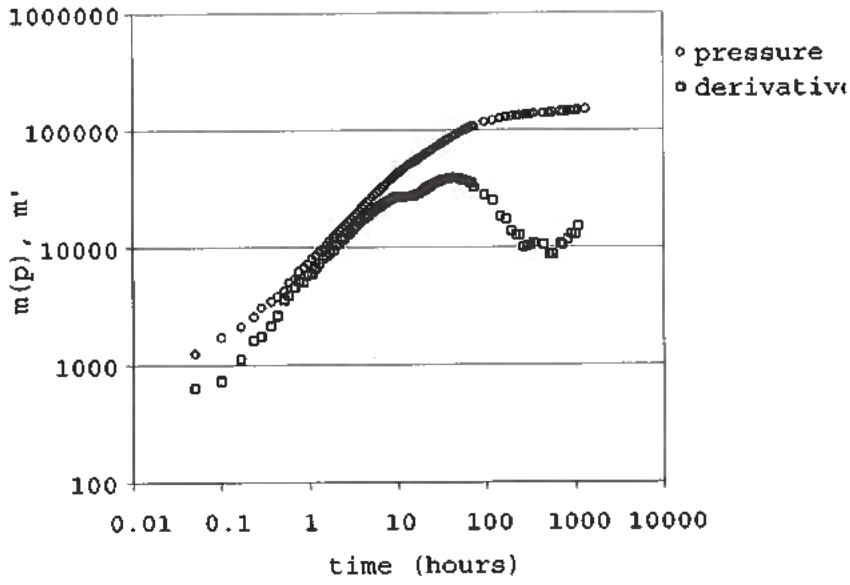

FIG. 5.4. Pressure data and derivative vs. time for the Weyburn field well. Since the well is not producing a single fluid phase (98% water, 2% oil) the axis is expressed in terms of pseudo pressure [**m(p)**] in units of *psi/cp* and derivative of pseudo pressure [**m'(p)**].

	Fit 1	Fit 2	Fit 3	Fit 4
$C\ (m^3/Kpa)$	0.040	0.039	0.043	0.037
S	-8.636	-8.944	-8.719	-12.109
$p_{ini}\ (Pa)$	23603	24800	24000	29000
$\kappa_P h\ (md-ft)$	274	177	244	41
ω	0.044	0.041	0.043	0.037
$\lambda x 10^{-8}$	8	0.1	9	0.005

Table 5.1. Well test parameter inversion results for four trial examples.

oil at 15 GPa differential pressure) and an average formation porosity $\phi_t = 0.2$, the normal fracture compliance estimated from equation (5.21) is $Z_{NF} \approx 0.003 GPa^{-1}$. Under the assumption of penny shaped fractures and limestone isotropic background, the estimated fracture compliance corresponds to a fracture density of $\eta_F \approx 0.03$. For an average aspect ratio $\alpha_F = 3x10^{-4}$ of fractures observed in Weyburn core Bunge (2000), the predicted fracture porosity is $\phi_F \approx 4x10^{-5}$. However, the fracture porosity estimated from Weyburn core averages $\phi_{F,core} \approx 3x10^{-4}$, which is an order of magnitude larger than the well test estimate.

Larger values of fracture porosity are expected from the core measurements due to the reduction in the confining stress that occurs when the core is extracted from the subsurface. Therefore, the porosity derived from well test analysis can be considered an *in situ* estimate that gives a lower bound to the possible values of fracture porosity.

The estimate of the fracture compressibility, $Z_{NF} \approx 0.003 GPa^{-1}$, is likely more reliable than the porosity estimate because of the smaller number of assumptions required for its calculation. In this data set, the stability of the inverted ω parameter facilitates obtaining an estimate of the fracture compressibility, Z_{NF}. Alternatively, where the storage capacity ratio is hard to obtain, Z_{NF} estimates from seismic data could be used to constrain the inversion of the ω parameter.

5.5 Discussion and Conclusions

In elastically isotropic reservoirs the storage capacity estimated from pressure-transient data, includes information of fluid compressibility and rock porosity averaged over the radius of investigation of the well test. This information can be used directly in Gassmann's equation to predict the changes in the rock's bulk compressibility with saturation.

In fractured anisotropic rocks, the storage capacity ratio (ω) provides information of the fracture compliance, fracture density and fracture porosity. In gas-producing wells in which the gas at reservoir conditions has a bulk modulus smaller

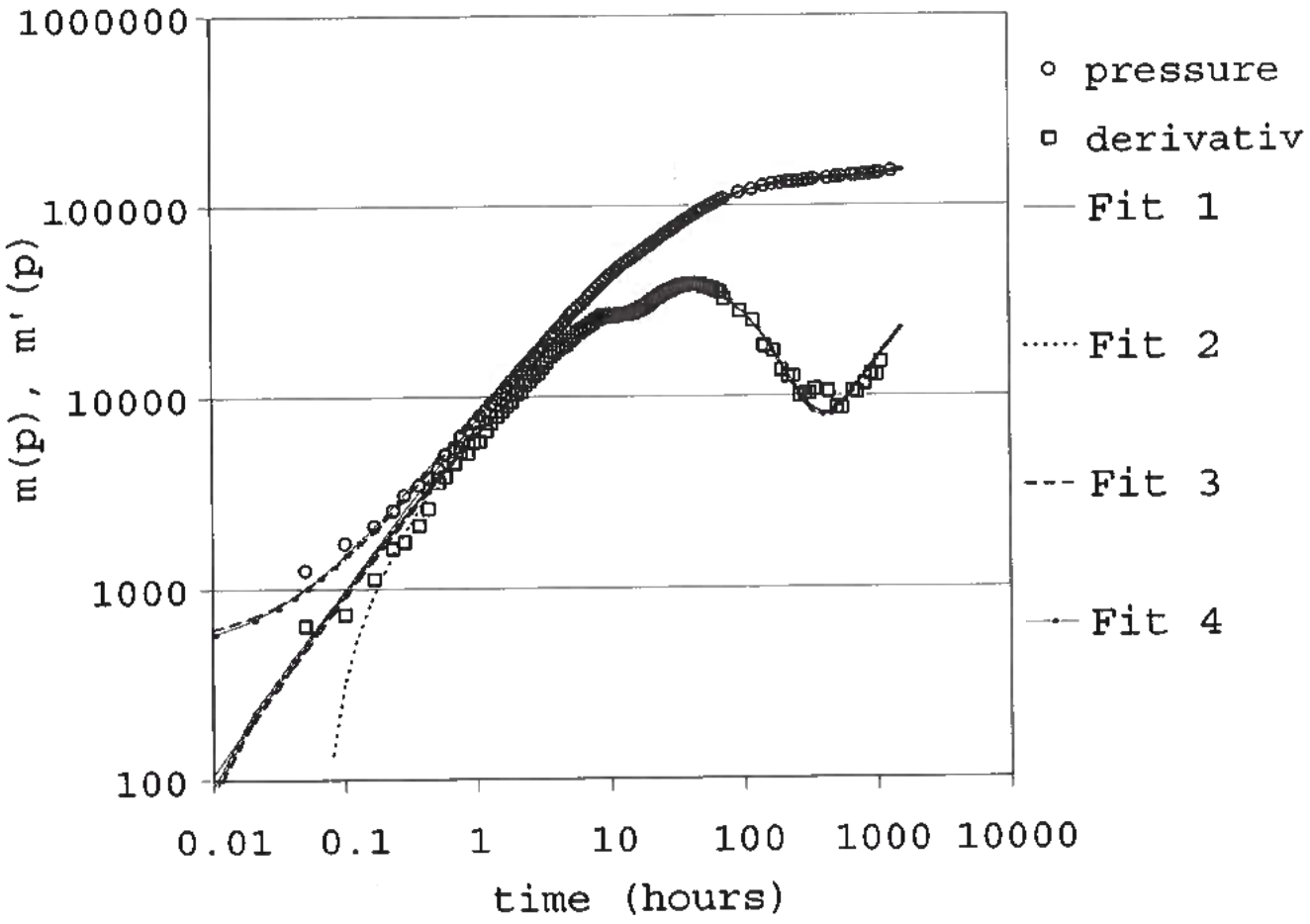

FIG. 5.5. Best fit models for the four parameter inversions shown in Table 1. Since the well is not producing a single fluid phase (98% water, 2% oil) the axis is expressed in terms of pseudo pressure [**m(p)**] in units of *psi/cp* and derivative of pseudo pressure [**m'(p)**].

than $0.05GPa$, the ω parameter can be used as an approximate measure of the fracture porosity to total porosity ratio ($\omega \approx \frac{\phi_F}{\phi_t}$). If the unfractured porosity (ϕ_i) is measured from well log tools, the fracture porosity can be approximated from estimates of ω.

If the well test experiment is done on a water saturated section of the fractured reservoir (high fluid bulk modulus), the storage capacity ratio can be approximated by a simple equation that is a function of the normal compliance of the fracture system (Z_{NF}). In this case ω can be estimated from seismically derived values of the normal fracture compliances and vice versa. If a specific model of fractures is assumed, such as an ellipsoidal crack model, the analysis can be taken further to predict the fracture density from the storage capacity ratio.

Even in cases where there is no idealized model that can quantitatively describe the fracture compliances as a function of the fracture density, these two will always be related qualitatively. In other words, a large value of the normal fracture compliance has to be associated to a large value of the fracture density. Since the exact equation for ω indicates that large values of fracture compliance correspond to large values of fracture density, we must conclude that the same qualitative relation will exist between ω and the fracture density. Therefore, if seismic and pressure-transient data are analyzed simultaneously in a reservoir that behaves as an anisotropic, double porosity rock, it should be possible to quantitatively correlate the variation in storage capacity ratio with variation of the normal fracture compliance.

Chapter 6

WEYBURN FIELD MULTICOMPONENT CASE STUDY

6.1 Introduction

As described in the introduction, Weyburn field produces oil from the fractured Mississippian carbonate rocks of the Midale beds. In 2000 the field operator, Encana, started a recovery project in which simultaneous, but separate, water and CO_2 injection was implemented to sweep the reservoir more efficiently and increase production.

Due to the existence of at least two fracture trends in the reservoir (Bunge, 2000), it is necessary to quantify the variation of the fracture density and the changes in fracture orientation because fractures are potential conduits of CO_2 that can induce early breaktrough at the producers. Therefore, the utility of time-lapse multicomponent data is two-fold: the "baseline" survey (before CO_2 injection) can be used for a static characterization of the reservoir area, whereas the "repeat" or "monitor" survey (after a period of CO_2 injection) can be used for a dynamic characterization by monitoring changes in the elastic parameters of the rock as the fluids migrate through the fracture network.

The data acquired by the Reservoir Characterization Project includes compressional-wave (P-wave) and shear-wave (S-wave) data for both the baseline and repeat surveys. Analysis of the P-wave data was performed by Brown (2002) and Herawati (2001) in the post-stack domain for the baseline and repeat survey, and by Jenner (2001) in the pre-stack domain for the baseline survey.

Brown (2002) concludes that amplitude differences between the P-wave baseline and monitor surveys correspond to changes in the fluid saturation in the reservoir due to the injection process. Furthermore, some of the amplitude variations seem to be related to fluid migration through fractures that connect horizontal injectors and producers. Jenner (2001) concluded that the azimuthal variation of the normal moveout (NMO) velocities of P-waves was related to the azimuthal anisotropy generated by the fractures in the reservoir interval. However, a more complete interpretation of the elastic anisotropy of the reservoir rocks requires simultaneous analysis/interpretation of both P- and S-waves.

When a shear-wave propagates through an elastically anisotropic medium the phenomenon of birefringence occurs, in which the initial wave splits into two waves with different polarizations and different propagation velocities. The fractional dif-

ference in travel time between the fast and slow split shear-waves is defined as the shear-wave splitting. Assuming that a stacked S-wave section generates an acceptable approximation of vertically propagating S-wave data, the analysis of the shear-wave splitting and polarization can be interpreted in conjunction with the P-wave azimuthal anisotropy to extract information about the fractured network.

Analysis of the shear-waves in the stacked domain was done before without properly accounting for the vertical and lateral variability of the shear-wave polarization (Reasnor, 2001). The work presented in this chapter shows how the "layer stripping" method proposed by Thomsen et al. (1999) was applied to the shear-wave data to remove the shear-wave splitting in the overburden before analyzing the reservoir interval. The analysis of shear-waves is done for both the baseline and repeat seismic surveys in order to assess the existence of any changes in the shear-splitting with the injection process.

After removing the influence of the overburden, areas of high shear-wave splitting in the reservoir interval can be consistently identified both from amplitude and travel time analyses. For both the baseline and repeat surveys, most of the time-based shear-splitting values are greater than zero by more than one standard deviation. The amplitude-based estimates of the shear-splitting are noisier and are usually within one standard deviation of zero, but the distribution of large splitting zones coincides with the travel-time derived splitting maps.

In the following sections I will start by describing the available data and the parameters that were used to acquire and process them. Next an overview of the layer stripping method and the polarization analysis will be presented.

6.2 Datasets and Acquisition

The seismic data were acquired over an area that includes four horizontal CO_2 injectors and several horizontal and vertical producers. Figure 6.1 indicates the well positions and the location of the three-component VSP and a full-waveform, dipole sonic log.

The baseline and monitor surveys were acquired in October 2000 and October 2001, respectively. In order to achieve the best repeatability between data sets, the surveys were designed with the same parameters (see Table 6.1), the only difference being the use of surrogate vibroseis trucks in case of break-downs. The acquisition parameters were designed to achieve high fold and wide azimuthal distribution in the center area that includes the four injectors.

The survey coordinate system was chosen with the inline direction approximately parallel to the horizontal injectors at an azimuth of N46E. The three-component geophones were oriented with the first horizontal component, H1, at N46E and the second horizontal component, H2, at N316E. The sources vibrated in the directions

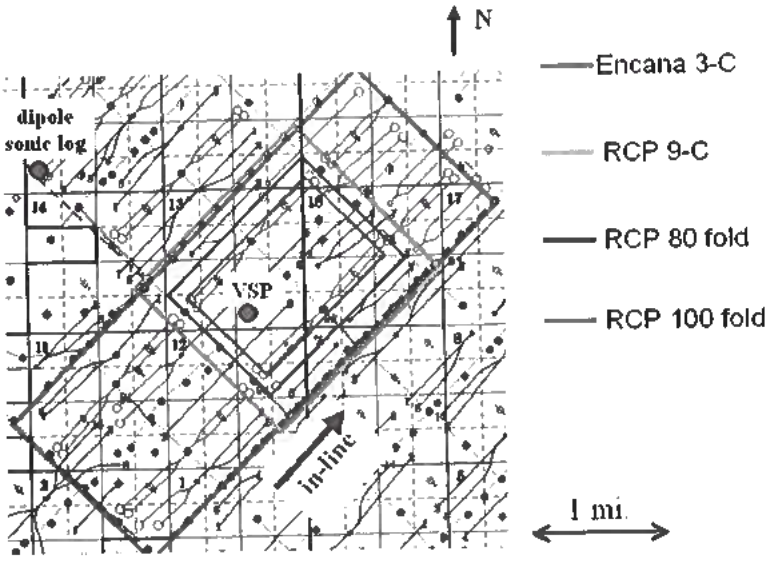

FIG. 6.1. Survey map with location of VSP and dipole sonic log.

S1 and S2 parallel to the H1 and H2 geophones respectively.

Under the assumption that the subsurface is horizontally layered and that waves approach the surface at near-vertical angles, most of the shear-wave energy is concentrated in the horizontal components of the geophones. If these assumptions hold, shear-wave analysis is reduced to the processing of four data subsets: S1H1, S1H2, S2H1 and S2H2. Each of these subsets correspond to a source-receiver combination e.g. the data subset S1H2 refers to the data recorded in the geophone component H2 emitted from the source component S1 (in what follows S1H1 and S2H2 are referred to as the diagonal trace elements, whereas S1H2 and S2H1 are referred to as the off-diagonal trace elements).

Before beginning the processing of the shear data, all sources and receivers were mathematically rotated to a coordinate system in which the source and receiver components S1 and H1 were oriented to N53E and the source and receiver components S2 and H2 were oriented to N323E (in what follows this will be referred to as the N53E coordinate system). This new coordinate system was obtained from a polarization analysis performed on the near offset VSP (Terrell, 2001).

To improve repeatability, the baseline data were reprocessed after the acquisition of the repeat survey. An important caveat, however, is that different ground moisture conditions between acquisitions resulted in poorer coupling of the sources and receivers in the monitor survey, which resulted in nosier estimates of the shear splitting from the second acquisition.

Parameter	Baseline	Repeat
Source	IVI TRIAX, Mertz 18, 13	IVI TRIAX, I/O Sidewinder
Sweep (P-wave)	8-180 Hz	8-180 Hz
Sweep (S-wave)	6-80 Hz	6-80 Hz
Source Spacing	40 m or 80 m	40 m or 80 m
Source Lines	28	28
Source Line Spacing	80 m	80 m
Source Points	1386	1386
Recording System	I/O System II	I/O System II
Sampling Interval	2 ms	2 ms
Receivers	OYO 10 Hz, 3-component	OYO 10 Hz, 3-component
Group Spacing	40 m	40 m
Groups per Line	60	60
Receiver Lines	20	20
Receiver Line Spacing	40 m	40 m
Maximum Fold	400 (P), 140 (S)	400 (P), 140 (S)

Table 6.1. Acquisition parameters for baseline and repeat surveys.

The following basic processing steps were applied to both the baseline and repeat data sets before the post-stack analysis:

1) Build geometry
2) Rotate all trace components to N53E
3) Surface consistent amplitude scaling
4) Spherical divergence correction $[(TV)^2]$
5) Mapping of P-S statics to S-S geometries and application
6) Velocity picking
7) Application of surface consistent statics and velocities
8) Shot domain application of Radon Filter
9) Mute
10) 2000ms AGC
11) Stack
12) Bandpass filter 5-35 Hz

6.3 Vertically Varying Shear-Splitting and Layer Stripping of Overburden

Although the desired parameter is the shear-splitting at the *reservoir level*, anisotropic intervals above the reservoir may generate splitting in the overburden

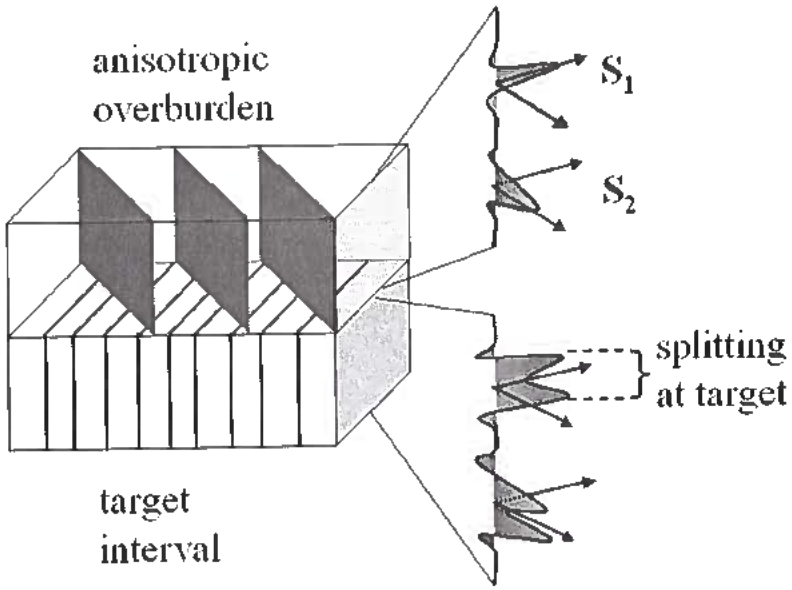

FIG. 6.2. Schematic representation of the detrimental effect of vertically varying shear-splitting on the recorded traces.

that mask the birefringence that occurs in the zone of interest. The existence of "anisotropic layers" in the overburden may result in a vertically varying shear-splitting that has a detrimental effect on the interpretation of S-waves at the target interval.

Although it is expected that the anisotropic layers have some correlation with geological layers, the correspondence is *not* necessarily one to one. The interpreter interactively judges from the data when there is an observable change in the polarization and/or splitting of the shear-waves Thomsen et al. (1999).

Figure 6.2 gives a simple example of the vertically varying shear-splitting in which two anisotropic layers are stacked on top of each other with the lower one as the target interval. The anisotropy in the layers is represented by sets of fractures aligned in different directions. When the vertically propagating shear-wave enters the top layer it splits into two waves, one polarized parallel to the fractures in that layer and the other polarized perpendicular to the fractures. After traveling through the top layer there is an accumulated time-lag between the split-waves due to the different velocities in each polarization direction. When the waves enter the target interval further splitting occurs and the same process is repeated as the waves are reflected back towards the surface. The end result is that the multiple splittings deteriorate the arrivals making it difficult to interpret the data.

Thomsen et al. (1999) proposed a layer stripping method to remove the influence of the azimuthal anisotropy in the overburden from the estimates taken at the target

interval. In this technique, each anisotropic layer is stripped from top to bottom through the application of four steps:

1) estimate the fast shear polarization direction in the layer and mathematically rotate the sources and receivers into the coordinate system defined by that direction

2) estimate the time lag (Δt) between the slow (S2H2) and fast (S1H1) trace elements at the bottom of the layer

3) remove the azimuthal anisotropy of the layer by subtracting the time lag (Δt) from the slow trace (S2H2), and by subtracting a time lag ($\Delta t/2$) from the off-diagonal traces (S1H2, S2H1)

4) equalize the amplitudes of the diagonal trace elements (S1H1, S2H2) to correct for any differential attenuation of the two shear-modes.

This procedure is repeated for all the layers until the target interval is reached.

The estimation of the fast polarization direction in a given layer is done by applying the Alford rotation method (Alford, 1986; Thomsen, 1988). The logic behind this technique is that in the hypothetical case that the S1 and H1 components of the sources and receivers were aligned with the fast shear polarization direction, all the energy of the fast shear-mode will be concentrated in the S1H1 trace and all the energy of the slow shear-mode will be in the S2H2 trace. Hence, finding the coordinate system defined by the fast shear-wave polarization consists in finding the angle by which the sources and receivers have be rotated to maximize the energy in the diagonal trace elements, S1H1 and S2H2.

Figure 6.3 shows the effect of the Alford rotation on noise-free synthetic traces in which the direction of the fast shear-wave polarization coincides with a rotation angle $\Theta = 0°$. When the rotation angle is $\Theta = 0°$ (S1 and H1 components aligned with the fast-polarization direction), the energy is maximized in the diagonal traces (S1H1 and S2H2) and minimized in the off-diagonal elements (only S1H2 is shown). The time-lag between the fast and slow traces is indicated by the dotted lines. As the rotation angle departs from zero, energy appears in the off-diagonal elements indicating that the source and receiver are *not* aligned with the coordinate system defined by the fast polarization direction. When the rotation angle is set to $\Theta = 90°$ the energy is minimized in the off-diagonals again, however, because the S1 and H1 components are aligned with the slow-polarization direction the time lag between the diagonal components is reversed with respect to the case when $\Theta = 0°$.

For the Weyburn field data, the polarization and layer stripping analyses were done separately for the baseline and repeat surveys. Figures 6.4-6.7 illustrate how the layer stripping procedure was applied showing the results for the baseline survey, the corresponding figures for the monitor survey are not shown but the approach was the same. The final products at the end of the post-stack shear-wave analysis are estimates shear-splitting from travel times and amplitudes, and fast shear-wave polarizations from travel times for both baseline and monitor surveys. Standard de-

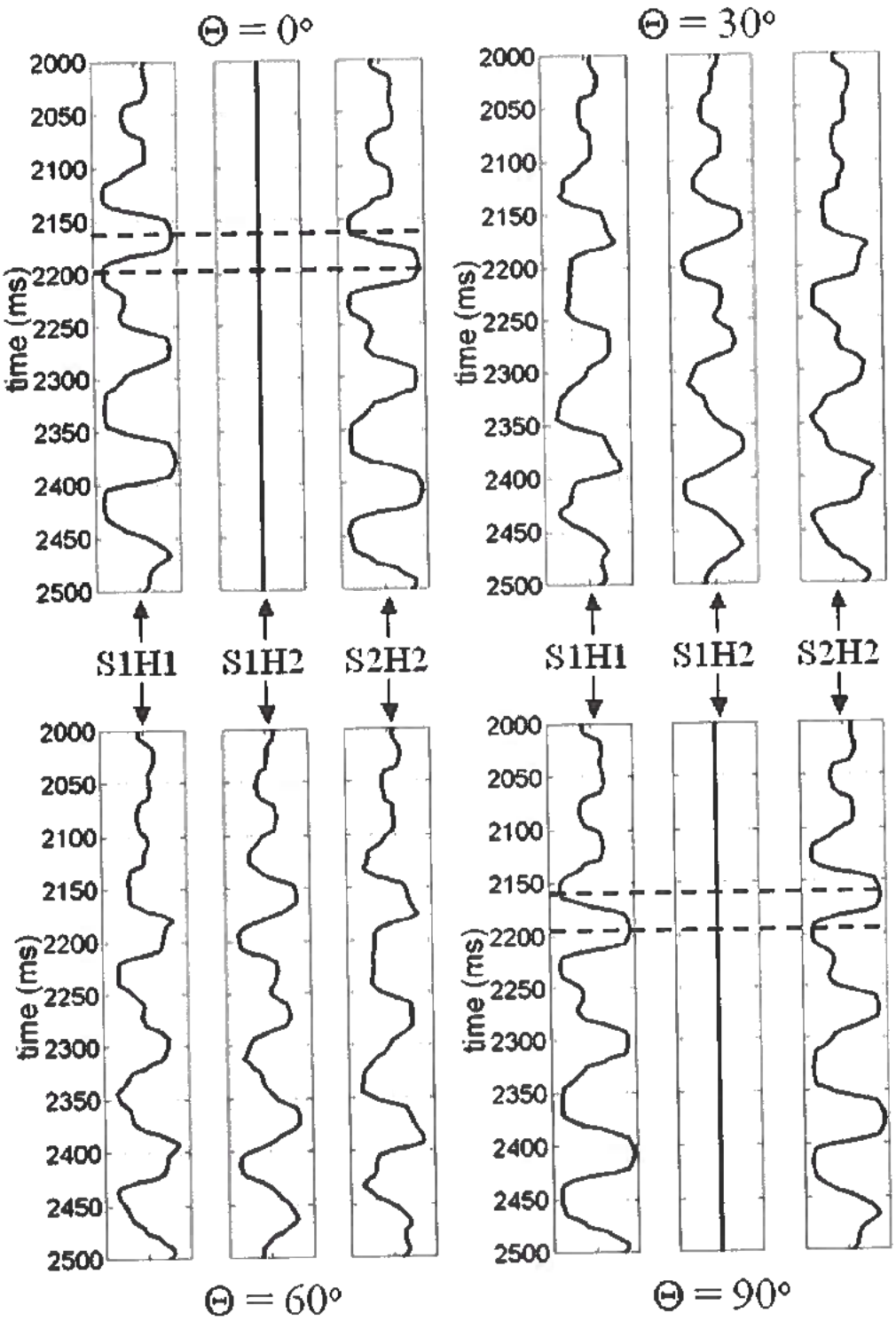

FIG. 6.3. Noise free, synthetic example of the effect of Alford Rotation on the components S1H1, S1H2, S2H2.

viations are also calculated for each of the parameters to be used in the interpretation in the next chapter.

Figure 6.4 shows the four trace elements S1H1, S1H2, S2H1 and S2H2 for one line of the Weyburn shear data rotated to the N53E coordinate system. The target zone is marked by the Mississippian unconformity horizon at approximately 3050 ms, and the reservoir is comprised by the Mississippian peak and the trough below it.

Two anisotropic layers were identified in the overburden from the time-varying rotation analysis performed on the data. The first layer is the interval that goes from the surface to the Viking horizon (Surface-to-Viking layer), whereas the second anisotropic layer is the interval between the Viking and the Lower Vanguard horizon (Viking-to-Vanguard layer) (Figure 6.4). The interval between the Lower Vanguard and the Mississippian horizons did not present any variation in the shear-splitting or shear-wave polarization.

The high energy visible in the cross-diagonal traces above the Viking and Lower Vanguard horizons indicates that the N53E coordinate system is not the "natural" coordinate system for these two layers. Note also that the change in cross-diagonal energy below the Viking horizon is indicative of the different polarization directions in the anisotropic layers.

Applying the layer stripping steps described above, the contribution of the anisotropic intervals in the overburden was removed. Figure 6.5 shows the reduction in the cross-diagonal energy that results after the complete layer stripping procedure is applied to both overburden layers.

In order to realize the effect of layer stripping on the data, Figures 6.6 and 6.7 show the variation of polarization directions between the Viking and Lower Vanguard horizons and compare the traces before and after the layer stripping procedure at each interval. Due to the orientation of the survey grid (see Figure 6.1), in all the maps shown below the data are presented in the survey coordinate system, in which North points at 46° from the x-axis.

The color map in Figure 6.6 shows the time difference between the fast and slow shear-wave (calculated as $t_{fast} - t_{slow}$) and the fast shear-wave polarization direction (black lines), at the Viking horizon after Alford rotation. The size of the line segments that represent the fast polarization direction are scaled by the difference $t_{fast} - t_{slow}$. Note that most of the polarization directions after Alford rotation are different from the N53E direction, which is roughly parallel to the x-line axis in the survey coordinate system.

The panels in the bottom of Figure 6.6 show the effect of layer stripping on in-line 68 of the Viking Horizon. Each panel presents the four traces: S1H1, S1H2, S2H1 and S2H2, for every x-line shown. Before layer stripping is applied, the time lag between the S1H1 and S2H2 traces and energy in the cross-diagonals are clearly visible. After layer stripping the time lag is removed, the cross-diagonal energy is

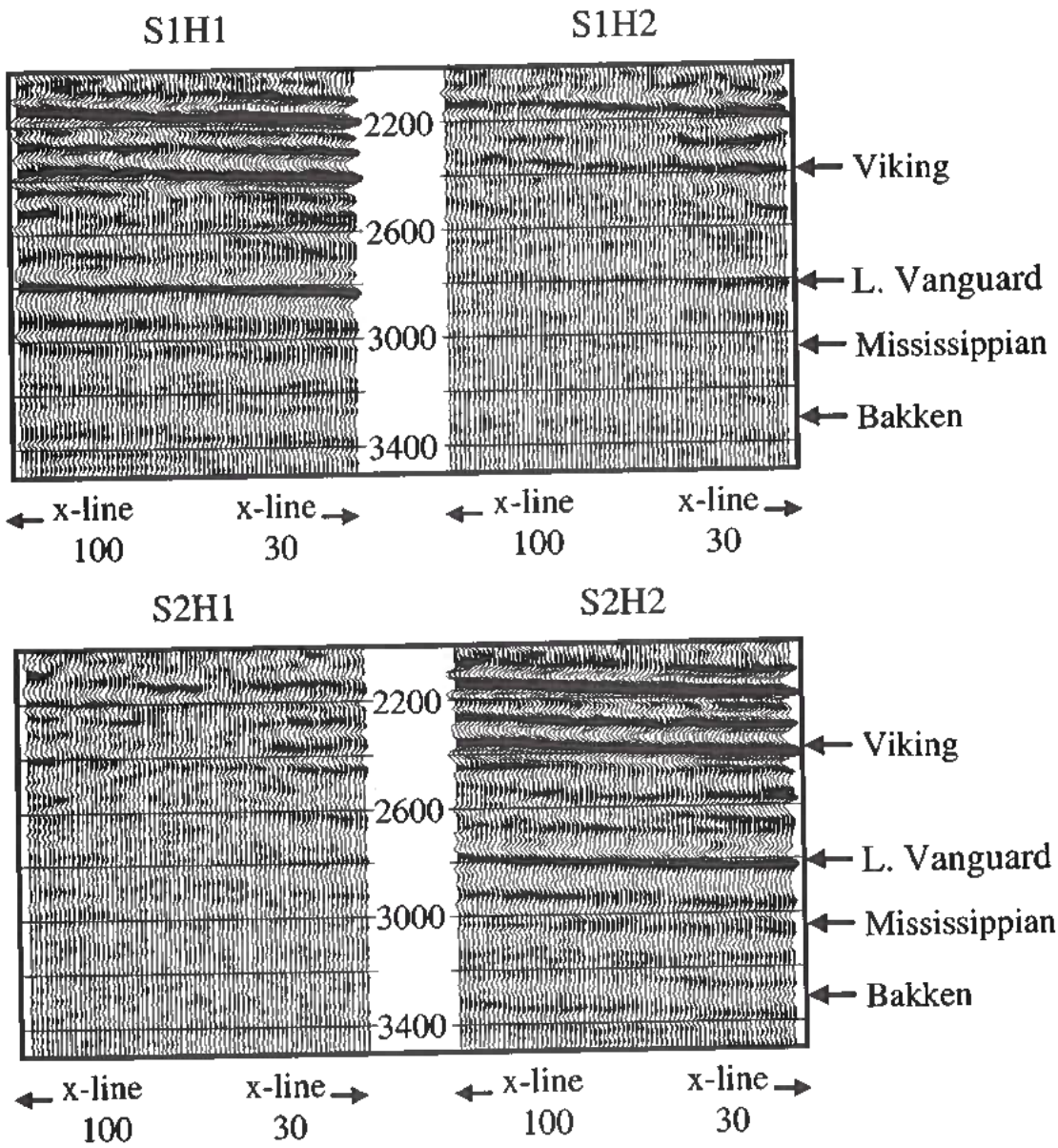

FIG. 6.4. Traces at line 80 before layer stripping and rotated into the N53E coordinate system. Note the high energy levels in the cross-diagonal traces above the Lower Vanguard horizon.

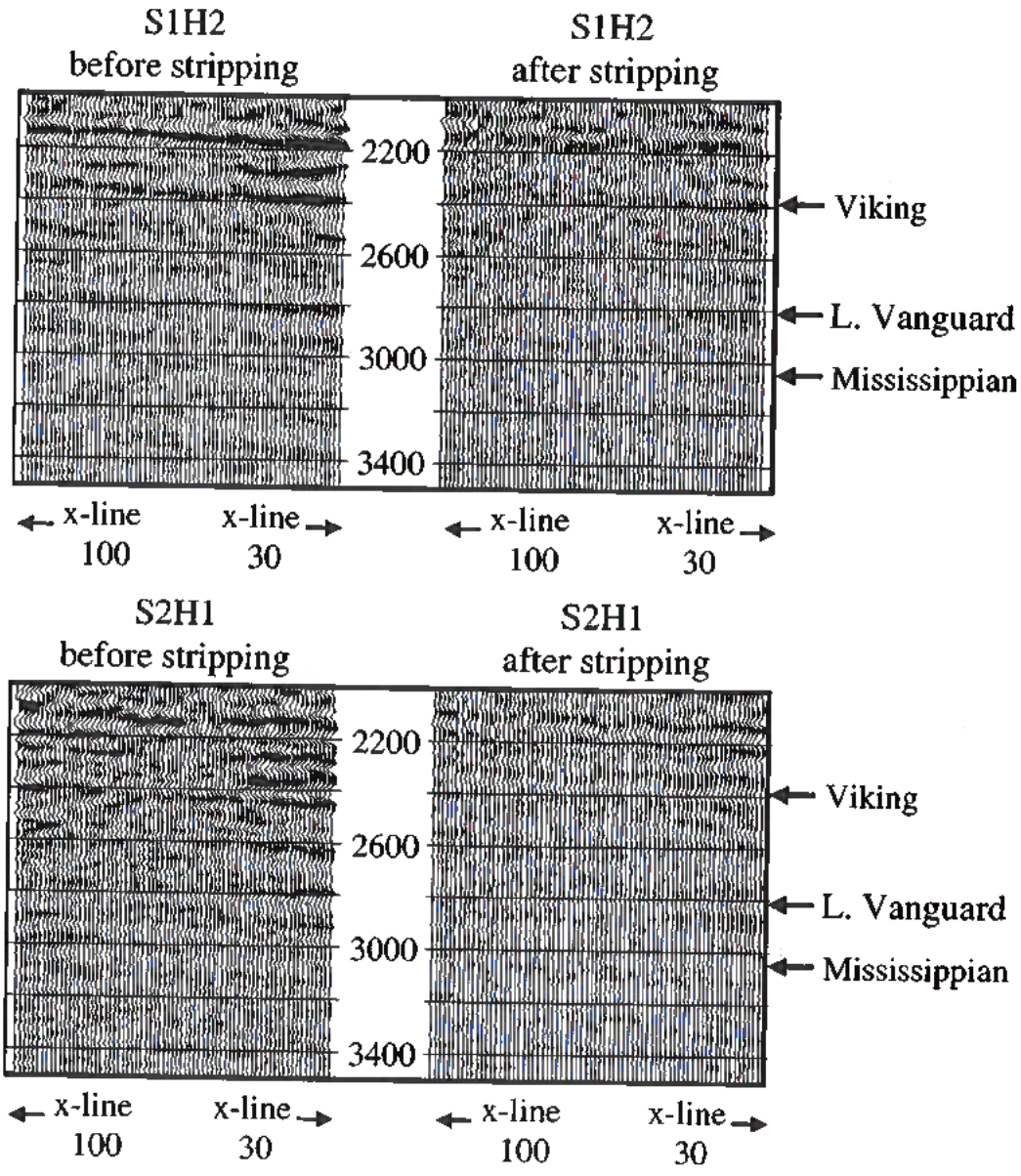

FIG. 6.5. Cross-diagonal traces S1H2 and S2H1, before and after layer stripping for line 80.

reduced and the amplitudes of the S1H1 and S2H2 traces are balanced. If the Surface-to-Viking layer were the only anisotropic interval in the overburden no further time differences or energy in the cross-diagonals would occur below the Viking after layer stripping. However, rotation analysis at the Lower Vanguard horizon revealed the need to consider the Viking-to-Vanguard interval as an independent anisotropic layer.

Figure 6.7 shows the map of fast and slow shear-wave time differences with polarization directions, calculated in the same way as Figure 6.6. Most of the splitting in this interval occurs below in-line 40 and between in-lines 60 and 80. Note that at the Lower Vanguard most of the fast shear polarization directions are perpendicular to the x-line axis, which indicates that they are almost perpendicular to the original rotation angle, N46E, applied to the data. The panels at the bottom of Figure 6.6 show how the layer stripping procedure applied to the Viking-Vanguard interval minimizes the cross-diagonal energy and balances the amplitudes between the S1H1 and S2H2 traces. Because the interval between the Lower Vanguard and the Mississippian horizons did not present vertical variations in the shear-splitting or shear-wave polarization, no further layer stripping analysis was done.

6.4 Travel-Time and Amplitude Analysis at the Target Interval

After the removing the influence of the overburden, the analysis of the shear-wave travel times and amplitudes was performed on the reservoir interval. Because of the thinness of the reservoir, which is included in the Missippian peak and the trough below it, travel times and amplitudes analysis provide information at different scales. In order to observe the build-up of the time lag between the fast and slow shear-waves it is necessary to analyze a coarse interval below the target horizon. Therefore, the shear splitting measured from travel times most probably will include contributions from the reservoir and the beds immediately below it. However, a more localized estimate of the shear splitting can be obtained from the difference in amplitudes between the different polarized shear-modes measured from reflections at the top of the reservoir (Thomsen, 1988).

The travel time analysis to estimate the shear-wave splitting and polarizations around the reservoir was performed in the time interval between the horizon immediately above the Mississippian unconformity, a peak at approximately 3000 ms, and the Bakken horizon, a trough located at approximately 3390ms (see Figure 6.7). This interval was chosen for two main reasons. First, the Bakken horizon is the most continuous and easiest to pick marker below the Mississippian unconformity. Second, the thickness of the time interval is approximately equal to the vertical resolution of the pre-stack analysis done on the azimuthal variation of P-wave NMO (Jenner, 2001). Since one of the objectives of the work presented here is to integrate the post-stack shear analysis with the pre-stack P-wave results, it is convenient to have estimates

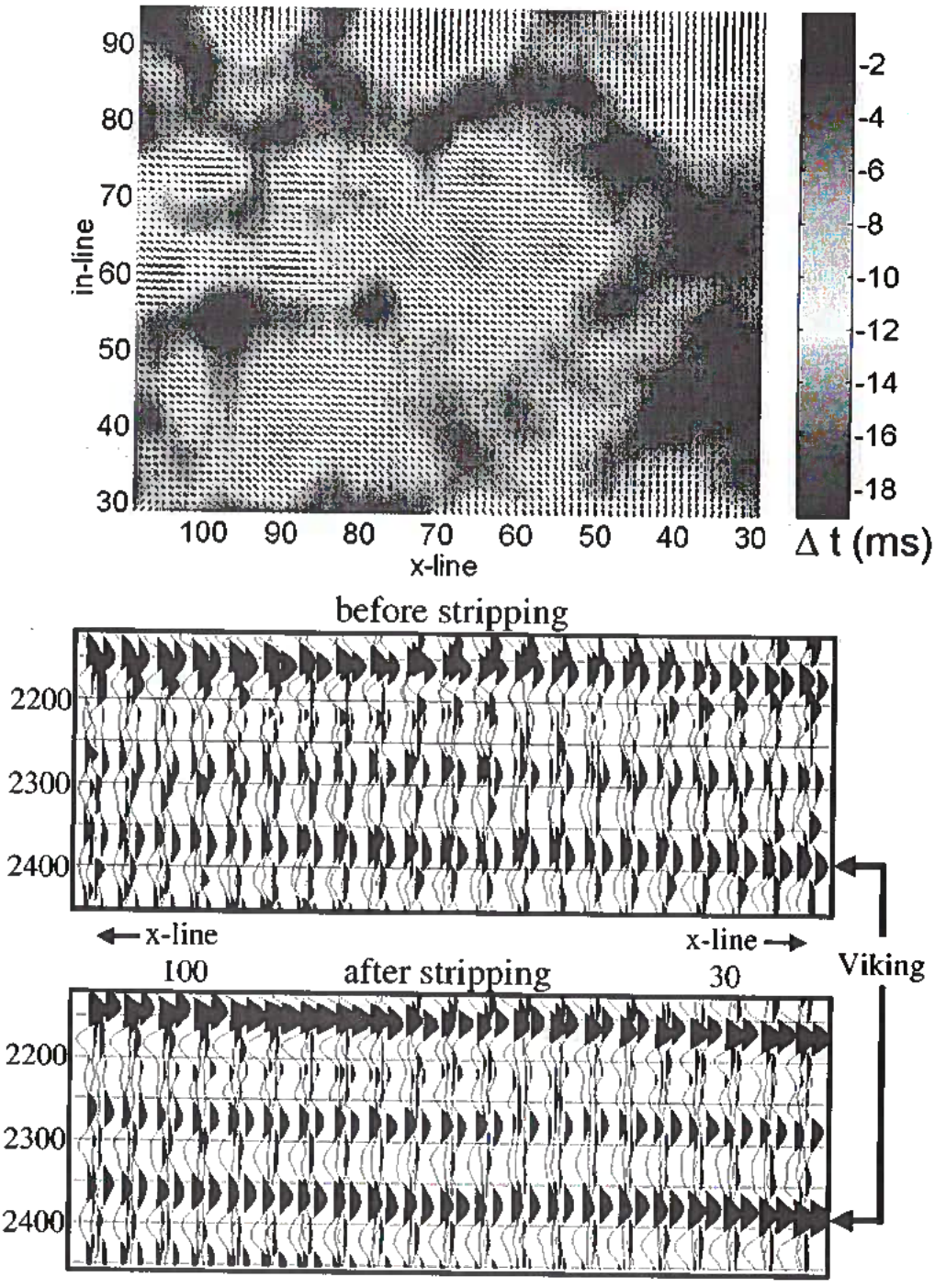

FIG. 6.6. Top: map of the time difference between the slow and fast shear-wave at the Viking horizon after Alford rotation. Bottom panels show the traces S1H1, S1H2, S2H1, S2H2 before and after the layer stripping procedure in the line portion indicated in the map.

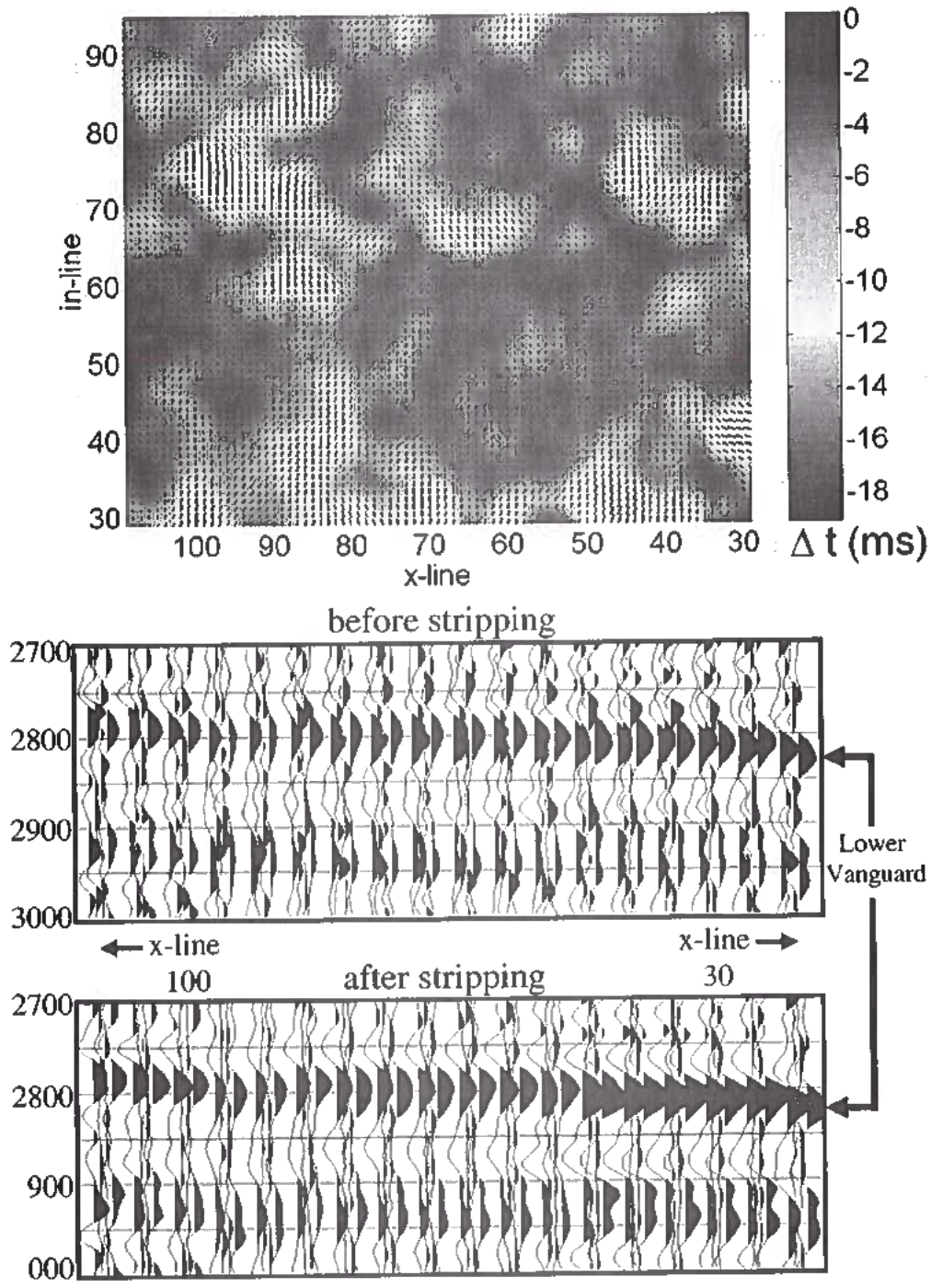

FIG. 6.7. Top: map of the time difference between the slow and fast shear-wave at the Lower Vanguard horizon after Alford rotation. Bottom panels show the traces S1H1, S1H2, S2H1, S2H2 before and after the layer stripping procedure in the line portion indicated in the map.

from both data sets that were obtained at comparable time scales.

Figures 6.8 and 6.9 show the *mean* estimates of the shear splitting and fast shear polarization directions calculated from travel times in the interval described above, for the baseline and the monitor surveys respectively. The qualifier *mean* indicates that each value shown in the maps is an average calculated from the "raw" shear-splitting values in overlapping bins of 9 x-lines by 9 in-lines or 180 by 180 meters (maps of the raw shear-splitting and fast shear polarization can be found in the Appendix A).

The logic behind averaging the "raw" values in a bin, is that the 20 meter spacing between Common Depth Points (CDP's) in the data is much smaller than the size of a Fresnel zone for the shear-waves at the target interval. If we assume that CDP's within a Fresnel zone sample roughly the same portion of the subsurface, we can use the mean of the values at the CDP's as an estimate of the shear-splitting and the standard deviation as an estimate of the uncertainty in the measurement. This method of calculating the estimate and its variance assumes that the uncertainty is constant within the selected bins (van Wijk et al., 1999).

Because the survey over Weyburn field was specifically designed to have closely spaced in-lines and x-lines, each mean and variance estimate can be calculated from 81 "raw" values. An important caveat is that the condition of locally constant uncertainty may be violated in areas of the data in which the parameter (e.g. shear-splitting) varies rapidly in a given direction within a bin size. Hence, it is possible that the standard deviation may be overestimated in the perimeter of high-anisotropy "anomalies".

The panels at the bottom of Figures 6.8 and 6.9 show pairs of fast and slow shear-wave traces along selected in-lines at the Bakken horizon, where the fast trace is the one to the left of the pair. The shear splitting (γ) can be calculated from the difference in travel times between the fast and slow trace. Assuming weak anisotropy γ can be written approximately as

$$\gamma \approx \frac{t_{fast} - t_{slow}}{t_{slow}}. \tag{6.1}$$

Because the distance traveled by the both shear-modes is the same and the vertical traveltime of each mode is the distance divided by the corresponding vertical velocity, equation 6.1 is equivalent to

$$\gamma \approx \frac{V_{slow} - V_{fast}}{V_{fast}}, \tag{6.2}$$

where V_{slow} and V_{fast} are the vertical velocities of the slow and fast shear-waves respectively. Hence, γ is always negative and it coincides with the linearized version of the Thomsen style parameter $\gamma^{(V)}$ for the case of a HTI symmetry rock (Tsvankin, 1997).

In order to give an idea of the uncertainty in the shear splitting estimates from

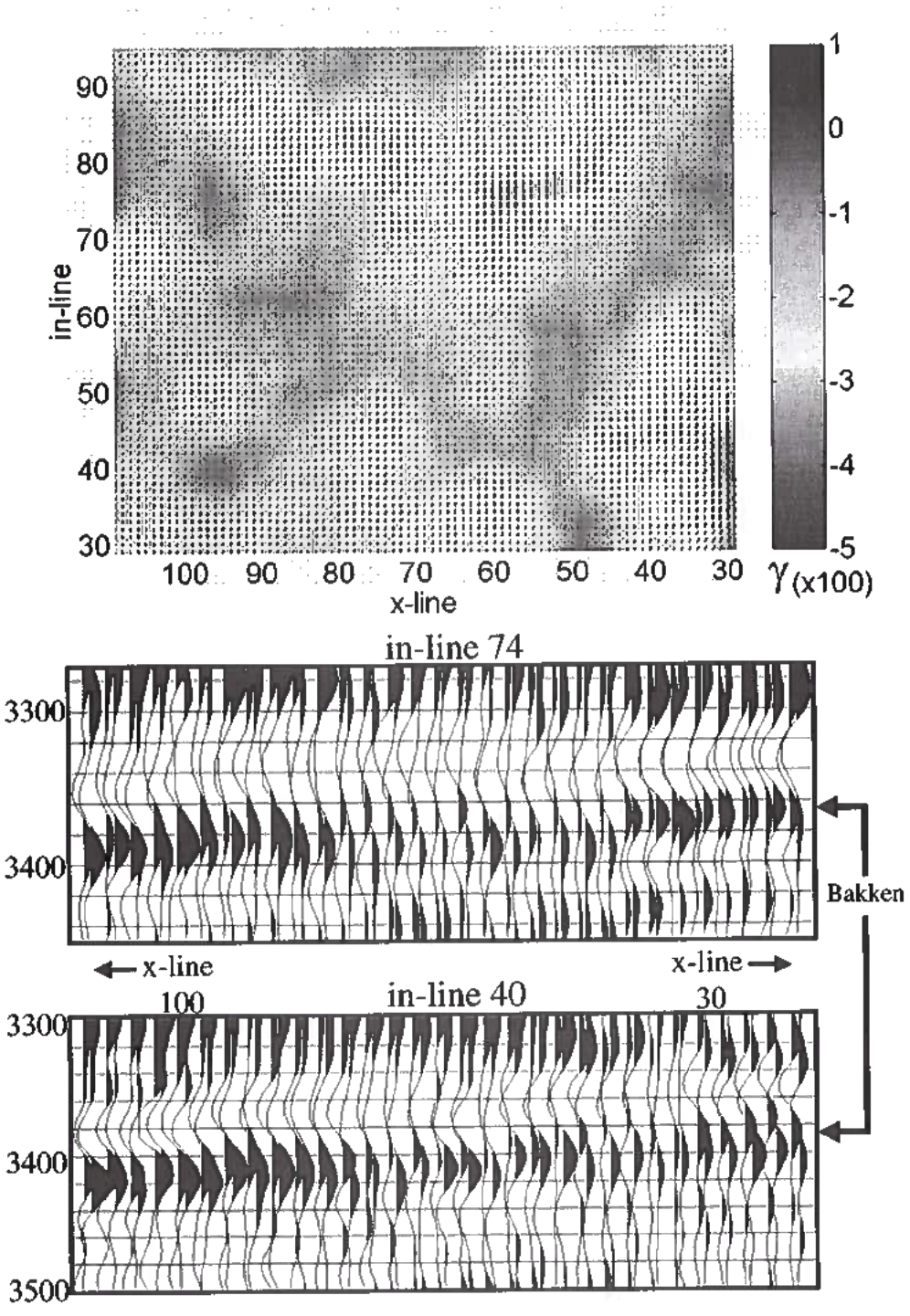

FIG. 6.8. Top: shear splitting parameter from travel times at the Bakken horizon for the baseline survey. Bottom: panels indicate time lag between the fast and slow S-waves for two in-lines. In each pair of traces the fast and slow shear-waves are located to the left and right, respectively. The panels are displayed in reverse polarity to improve visibility of the Bakken trough.

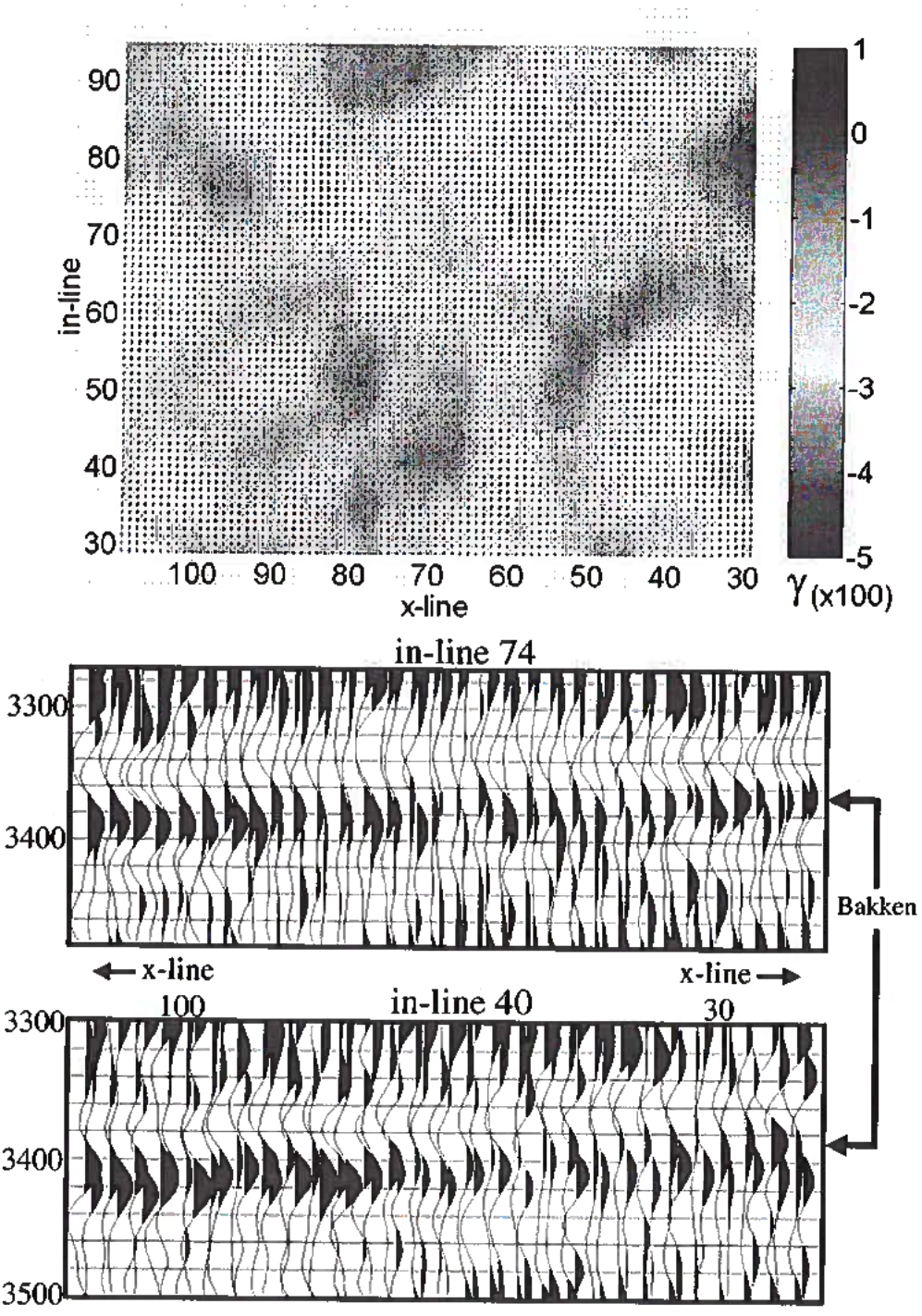

FIG. 6.9. Top: shear splitting parameter from travel times at the Bakken horizon for the monitor survey. Bottom: panels indicate time lag between the fast and slow S-waves for two in-lines. In each pair of traces the fast and slow shear-waves are located to the left and right, respectively. The panels are displayed in reverse polarity to improve visibility of the Bakken trough.

travel-times, Figure 6.10 shows the shear splitting for the baseline and monitor surveys setting to zero all values that are within one standard deviation of zero. Figure 6.11 shows a more conservative approach in which all values within two standard deviations from zero are set to zero. From both figures one can tell that the estimates in the baseline survey have a smaller variance, which is consistent with the observation that the baseline data appears less noisy to the eye than the monitor survey.

Figures 6.8-6.10 suggest three different approaches for interpretation of the travel-time results. In the most liberal interpretation (qualitative) all the features found in the shear-splitting maps would be taken into consideration. In the two more conservative interpretations only values "above" one or two standard deviations from zero would be considered statistically significant. In the next chapter the one standard deviation approach will be used to interpret simultaneously the travel-time derived shear-splitting and the P-wave NMO results.

As mentioned previously, the reflectivity differences between the different polarized shear modes can provide estimates of the change in shear splitting across the reflecting interface. If R_{11} and R_{22} represent the normal-incidence reflectivity of the fast and slow shear-wave respectively, then

$$R_{22} - R_{11} \approx \frac{1}{2}(\gamma_2 - \gamma_1), \tag{6.3}$$

where γ_1 and γ_2 are the shear-splitting above and below the reflecting interface respectively. If the layer above the reservoir does not present split S-waves (e.g. an isotropic cap layer), then the difference in reflectivity can be interpreted as the shear-splitting in the reservoir layer.

As mentioned above, the layer directly above the Mississippian unconformity did not have significant shear-splitting in the layer-stripping analysis. This observation is consistent with the shear-splitting calculated from the dipole-sonic log located north of the survey area (see location in Figure 6.1). Figure 6.12 shows that with the exception of some noisy spikes there is no significant shear-splitting in the layers directly above the Mississippian unconformity, whereas the splitting increases coherently in the reservoir interval. Therefore, it is reasonable to assume that the shear-splitting parameter γ_1 above the Mississippian interface is zero. The previous assumption allows interpreting the difference between the fast and slow reflectivity at the Mississippian as the shear-splitting parameter in the reservoir interval.

The reflectivities R_{11} and R_{22} are calculated by normalizing the amplitudes picked at the Mississippian in the S1H1 and S2H2 traces by the amplitudes picked at the Lower Vanguard after layer stripping. This can be done because after the layer stripping procedure is applied, the effects of propagation through the overburden are removed and the shear amplitudes at the Lower Vanguard represent the strength of an effective source that propagates the signal into the layers below.

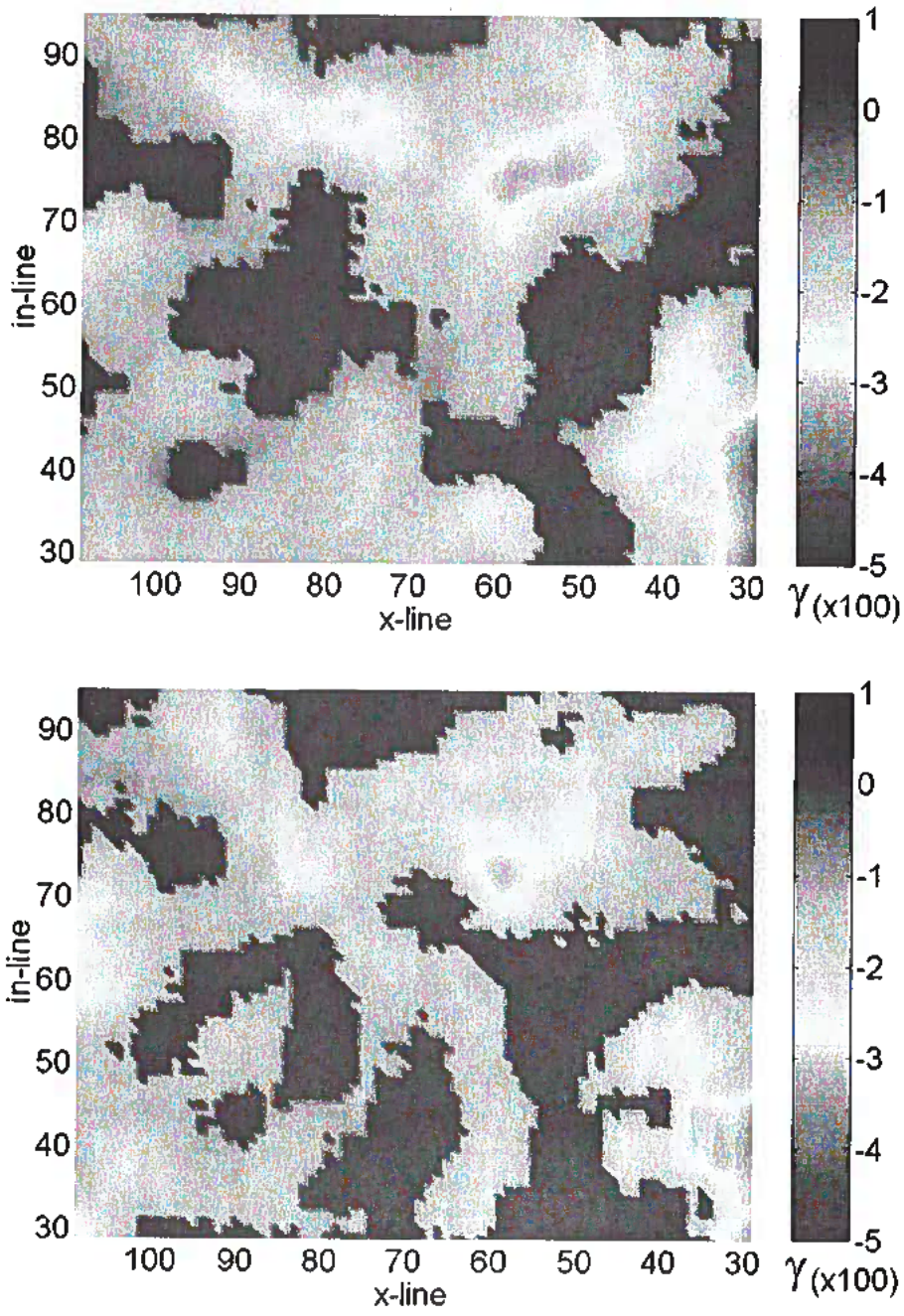

FIG. 6.10. Values of shear splitting parameter from travel times above one standard deviation for the monitor survey (top) and repeat survey (bottom). All values of shear splitting that are within one standard deviation of zero are set to zero.

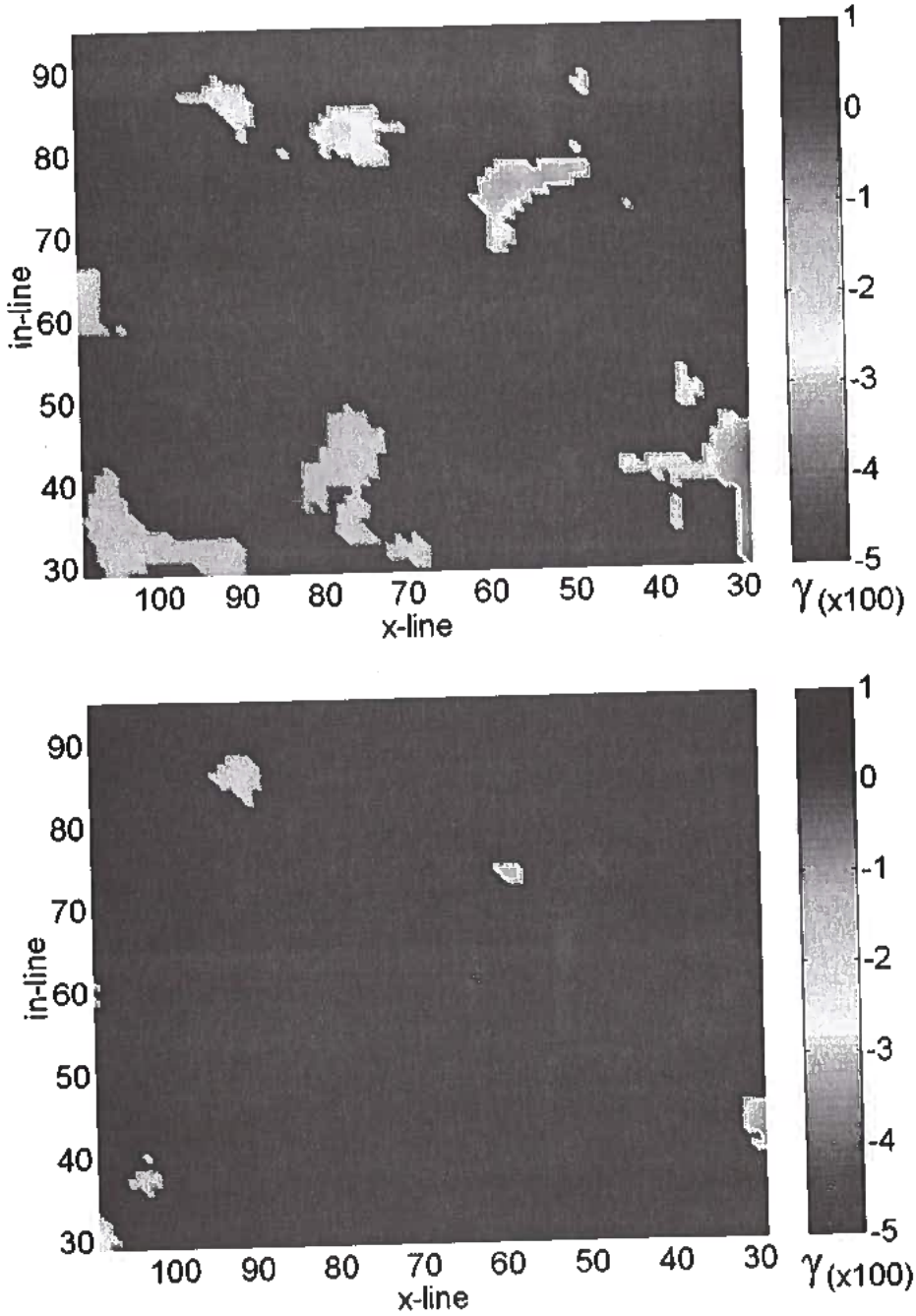

FIG. 6.11. Values of shear splitting parameter from travel times above two standard deviation for the monitor survey (top) and repeat survey (bottom). All values of shear splitting that are within two standard deviation of zero are set to zero.

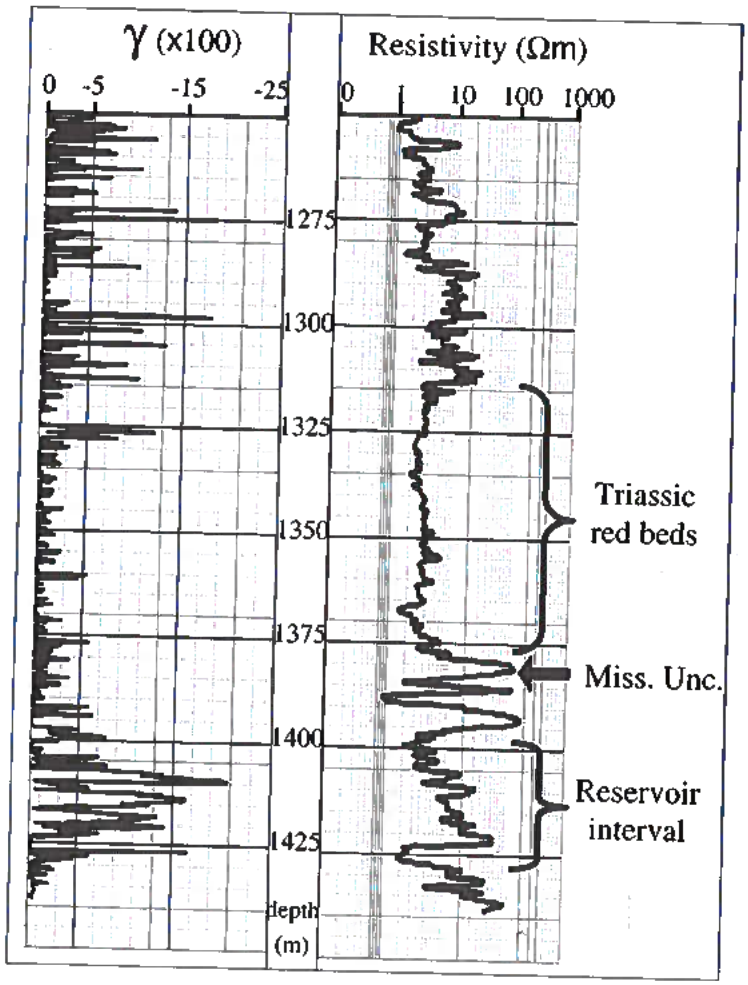

FIG. 6.12. γ parameter from dipole-sonic log and corrected resistivity indicating absence of significant shear-splitting in interval directly above the Mississippian unconformity

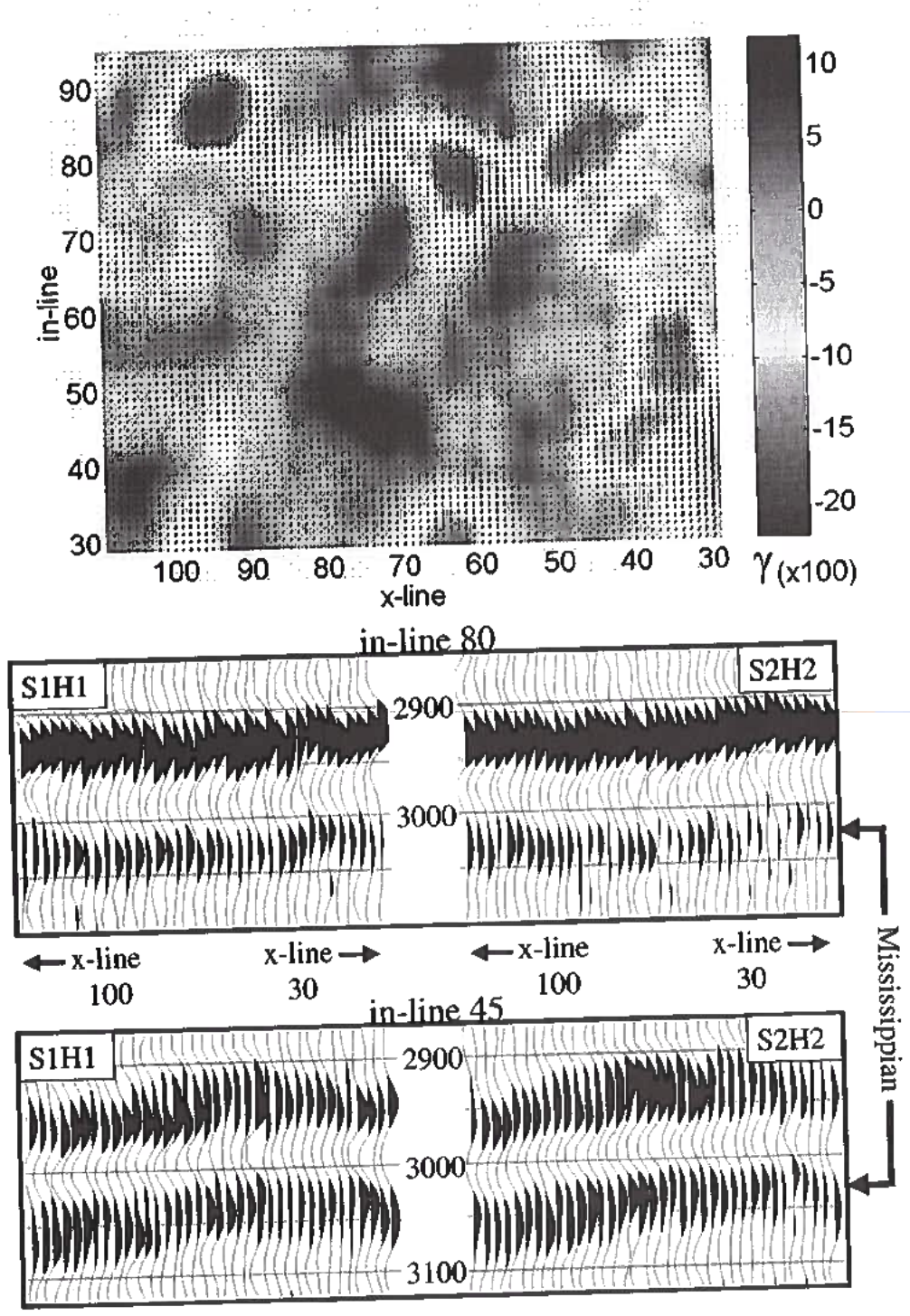

FIG. 6.13. Top: shear splitting parameter from RMS amplitudes picked on the Mississippian unconformity for the baseline survey. Bottom: panels with examples of amplitude differences between the fast (S1H1) and slow (S2H2) S-waves for in-lines 80 and 45.

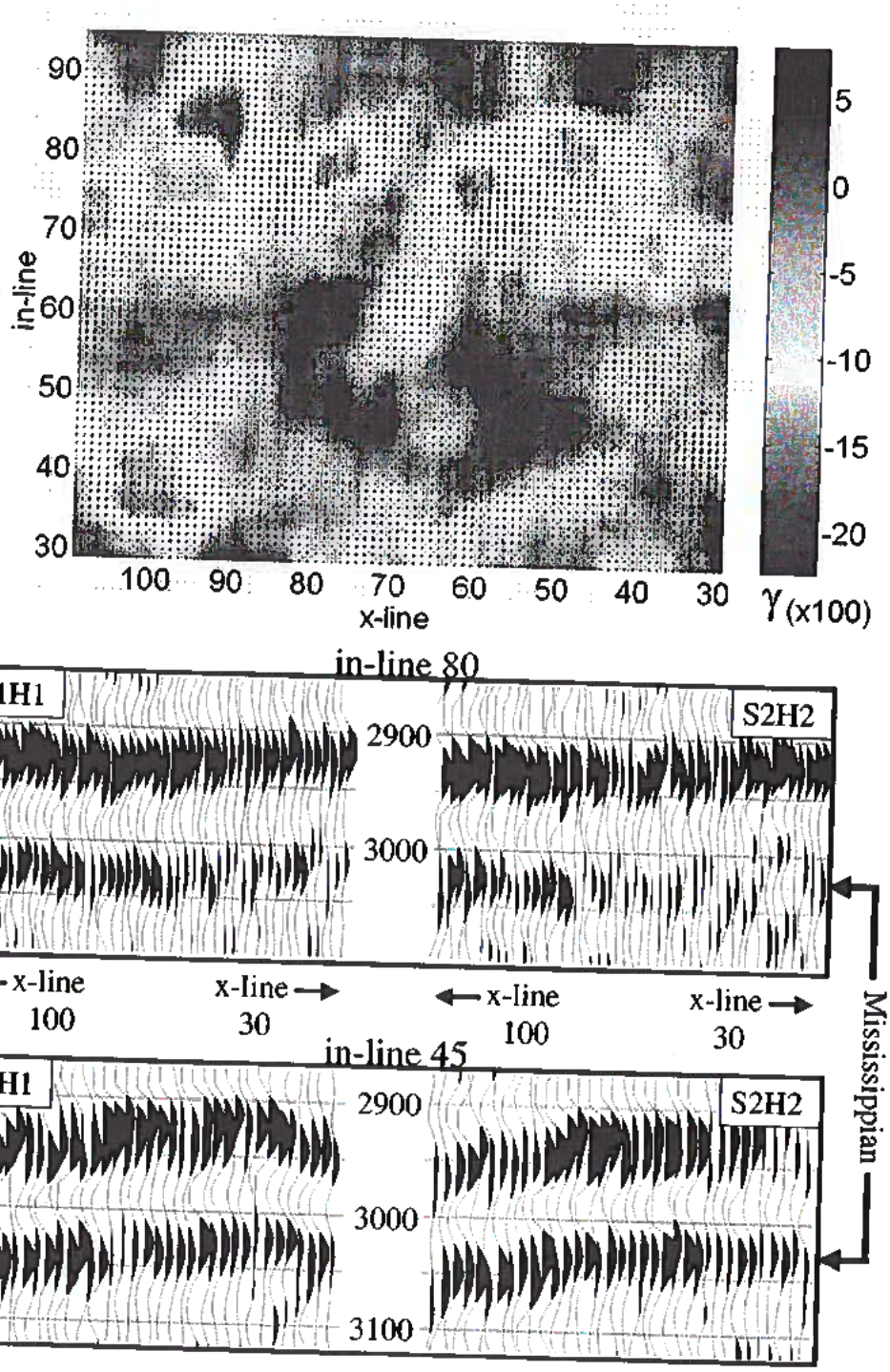

FIG. 6.14. Top: shear splitting parameter from RMS amplitudes picked on the Mississippian unconformity for the monitor survey. Bottom: panels with examples of amplitude differences between the fast (S1H1) and slow (S2H2) S-waves for in-lines 80 and 45.

Figures 6.13 and 6.14 show the mean estimates of the shear-splitting below the Mississippian unconformity derived from RMS amplitudes for the baseline and monitor survey, respectively. The fast shear polarizations direction derived from the travel-time analysis are also shown for references. The panels at the bottom of the figures give examples of the difference in amplitudes between the two shear polarization directions at in-lines 45 and 80.

The mean estimates are obtained from the "raw" amplitude values using the same procedure described for the time-based shear-splitting. Maps of the raw values and the standard deviation calculated from them can be found in Appendix A. Note that the values of shear-splitting derived from amplitudes are much larger than those obtained from the travel-time analysis. However, as it can be seen from the standard deviations shown in Appendix A, most of the amplitude-derived splitting values fall within one standard deviation of zero and all the values are within two standard deviations of zero for both the baseline and monitor surveys. This indicates that even though the amplitude estimates have a better vertical resolution than their travel-time counterparts, they are noisier and have to be interpreted within a lower confidence threshold.

By comparing the shear-splitting estimates from travel-times and amplitudes in the baseline survey (Figures 6.8 and 6.13), it can be seen that there is a good correlation between the high splitting trends in both maps. Two main matching trends can be identified between in-lines 70 and 90 in the top section of the map and between x-lines 30 and 45 in the lower right corner of the maps. Because the travel-time estimates are obtained at a coarser scale than the amplitude estimates, the correlation between high splitting trends suggests that in those areas the shear-splitting measured from travel-times results from splitting occuring in the reservoir beds.

The correlation between high splitting values between the amplitude and travel-time based maps is less evident for the monitor survey. In this case a rough correlation can be observed between the high-splitting trends between in-lines 70 and 90. The most notable change compared to the baseline survey is that the high-splitting zone that was located in the lower right corner between x-lines 30 and 45, no longer appears in the monitor survey amplitude map. Interpretation of the time-lapse variations of the shear-splitting maps will be done in the next chapter.

Chapter 7

INTERPRETATION OF WEYBURN FIELD DATA

7.1 Introduction

As described in the introduction, Weyburn field is a fractured Mississippian carbonate reservoir that has undergone an enhanced recovery process in which water and CO_2 are injected to improve oil production. There is extensive proof that the reservoir is fractured and that there are at least two different fracture trends that can influence fluid migration in the reservoir (Bunge, 2000). It is important to characterize the fracture trends because the objective of the CO_2 injection is to sweep zones of by-passed oil in the reservoir. If the CO_2 encounters fractured zones that provide a direct pathway to the producers the injection process will lose efficiency because instead of sweeping the oil the CO_2 will just be recycled between injectors and producers.

In this Chapter several of the concepts that were introduced in Chapters 3 and 4 will be applied to the characterization from seismic data of the fractured network of Weyburn Field. The first part of the interpretation consists of the analysis of the baseline seismic survey (before CO_2 injection) whereas the second part integrates the time-lapse information from differences observed between the baseline and monitor seismic surveys, and from changes in the production rates.

7.2 Baseline Analysis

The characterization of the baseline survey is centered on the analyses of the polarizations and splitting of shear-waves estimated from travel times, and the azimuthal variation of the normal moveout (NMO) velocities of P-waves for the baseline survey. The processing of the S-waves and the method to obtain polarizations and shear splitting is described in Chapter 7, whereas the processing of the P-waves and the method to obtain the azimuthal variation of the P-wave NMO velocities can be found in Jenner (2001).

The estimates of shear splitting and NMO velocities from the P- and S-wave data are calculated over a vertical section that includes the reservoir, spanning from the reflection immediately above the Mississippian unconformity to the Bakken horizon. Due to the thinness of the reservoir interval, the estimates are also influenced by the carbonate and clastic sections below the reservoir. Hence, the interpretation is done assuming that the anisotropy in the reservoir makes a measurable contribution to the

average anisotropy measured over the whole interval.

Although in general the azimuthal variation NMO velocities may result from dipping reflectors, Jenner (2000) has established that the azimuthal variation around the reservoir interval at Weyburn field is due to the azimuthal anisotropy of the rocks. Hence, Jenner's results will be interpreted solely in the context of anisotropic rock models, and the presence of P-wave NMO or S-wave splitting will be considered a proxy for elastic anisotropy.

The baseline analysis presented below is based on a model-driven classification of the anisotropic parameters estimated from the seismic data. The procedure is to calculate the range of physically plausible anisotropic parameters for several fracture models that are consistent with the fracture orientations found on oriented core and borehole imager data. Then, different regions of the survey area are identified with a fracture model depending on whether the anisotropic parameters estimated from the seismic data are consistent with the ranges predicted by each model.

Bakulin et al. (2000a,b,c) have developed procedures to predict the ranges of possible anisotropic parameters for several fractured rock models including: a single set of aligned vertical fractures, two orthogonal sets fractures and two sets of non-orthogonal fractures . These models are of relevance to the Weyburn study because core and borehole imager data reveal that the fractures are near vertical and may have several different azimuths throughout the reservoir.

The complexity of a fracture model increases with the number of fracture sets and as the rheology of the fractures requires more parameters to describe their elastic behavior. The simplest fracture type is that of a rotationally invariant crack which is described by only two parameters, the normal compliance (Z_N) and tangential compliance (Z_T)(see Chapter 3). If we assume that the fractures at Weyburn field are rotationally invariant, it is possible to generate several models of increasing complexity that are consistent with the fracture orientations found on core and borehole imager data.

Figure 7.1 shows the fracture counts and orientations from borehole imagers on two horizontal wells (EM1-1 and EMI-2), and from one core extracted from a vertical well. The red lines on the EM1-1 and EMI-2 plots indicate the azimuth of the horizontal well along which the measurements were done. The fracture count is low in the direction of the wellbore azimuth because it is difficult to intersect fractures that trend parallel to the horizontal well.

Figure 7.1 suggests there may be up to three fracture sets present in the reservoir interval. However, because the vertical core measurements only show two fracture trends and the borehole imager counts are taken over the total length of the horizontal well, the question remains of whether the three fracture sets are co-located everywhere or if there are fewer sets that change orientation through the reservoir. To maintain all possibilities open, models with one, two and three vertical fracture sets will be

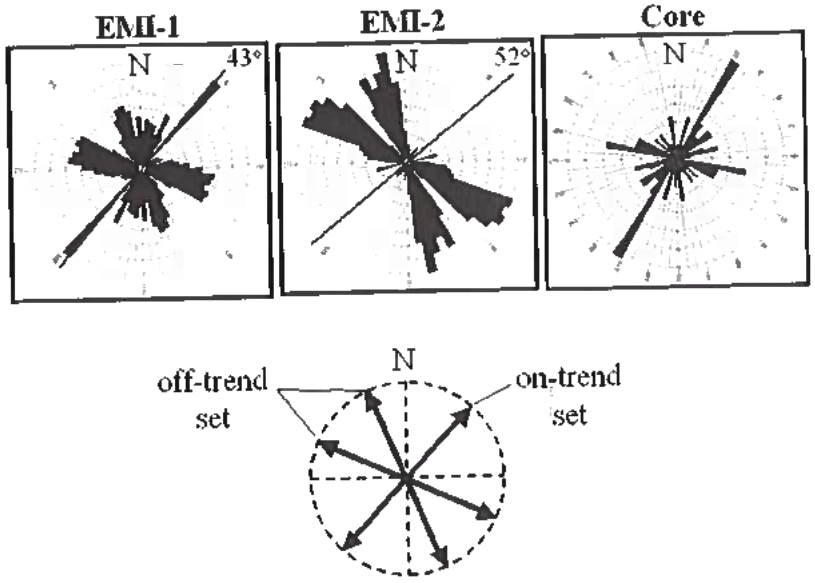

FIG. 7.1. Rose plots indicating fracture orientations in the reservoir interval from horizontal borehole imager data (EMI-1 and EMI-2) and oriented core data. The red lines one the EMI-1 and EMI-2 plots indicate the azimuths of the horizontal boreholes

considered below.

Figure 7.2 shows the basemap of the survey area indicating the location of the injectors (black) and producers (red), and illustrates the importance of identifying the number of co-located fracture sets and their orientation. The sets defined as the "off-trend" in Figure 7.2 are aligned in the direction that "connects" the injectors with the producers. If the injected CO_2 front encounters "off-trend" fracture sets, early breakthrough of CO_2 may occur resulting in a less efficient sweep of the zone between injectors and producers.

7.2.1 Estimates from P- and S-wave data

Figures 7.3 and 7.4 show estimates of the shear-wave splitting and the fractional difference between the fast and slow P-wave NMO velocities. The maps are rotated into the survey coordinate system with north pointing 45 degrees from the x-line axis, and the location of the injector and producer wells is indicated in black and red colors respectively.

The bottom plot in each figure indicates with black arrows the orientation of the fast shear-wave polarization and the fast P-NMO azimuth. From the shear-wave estimates is obvious that most of the fast shear-wave polarizations point in the off-

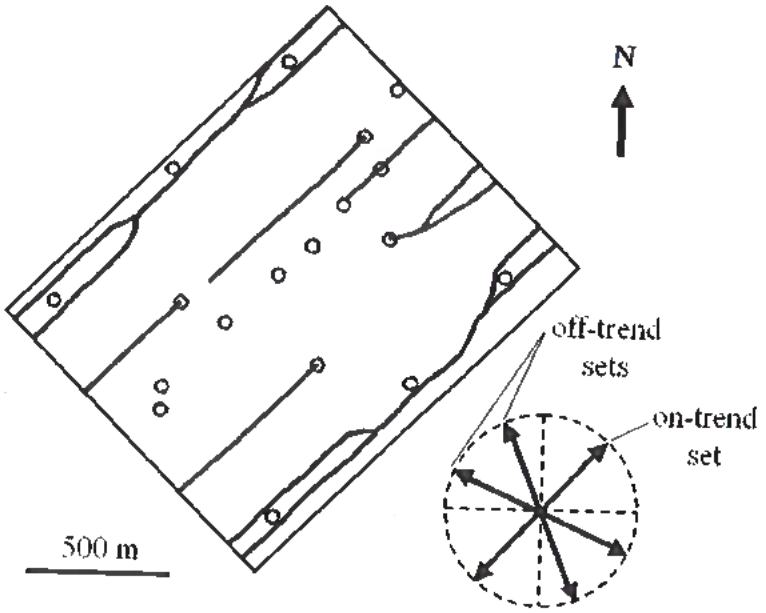

FIG. 7.2. Map of the survey area indicating location of injectors (black) and producers (red). The arrows in the rose plot indicate the fracture orientations from oriented core and borehole imager data.

trend direction defined in Figure 7.2, and the same applies to the fast NMO azimuth in the zones above in-line 70 and below x-line 40. However, in the lower section of the survey between inlines 30 and 50, the fast shear polarization and the fast NMO azimuth may differ by as much as 45°.

Figure 7.5 shows a map of the differences between the fast P-NMO azimuth (β_P) and the fast shear polarization (Π). The fast P-NMO and fast shear polarization directions are considered identical in the areas that have been set to zero (dark blue), which correspond to values of $|\beta_P - \Pi|$ that are smaller than the estimated standard deviation in the difference. In the areas in which the difference $|\beta_P - \Pi|$ is significant, the orientation of the P-NMO fast azimuth is indicated by line segments and the fast S-wave polarization orientation is indicated by arrows. The red areas, in which the orientation difference is close to 90°, are not significant because they correspond to low anisotropy zones in both the P-wave NMO and S-wave splitting maps.

The differences in the alignment of the S-wave polarizations and fast P-NMO ellipse suggest that the fracture network in the lower section may be different from the rest of the survey area. As it was shown in Chapter 4, rocks with monoclinic or lower symmetry may have NMO ellipses that are rotated with respect to the directions of the fast shear-wave polarization. Because rocks with higher symmetry (non-tilted orthorhombic and HTI) will have NMO ellipses that will match the fast-

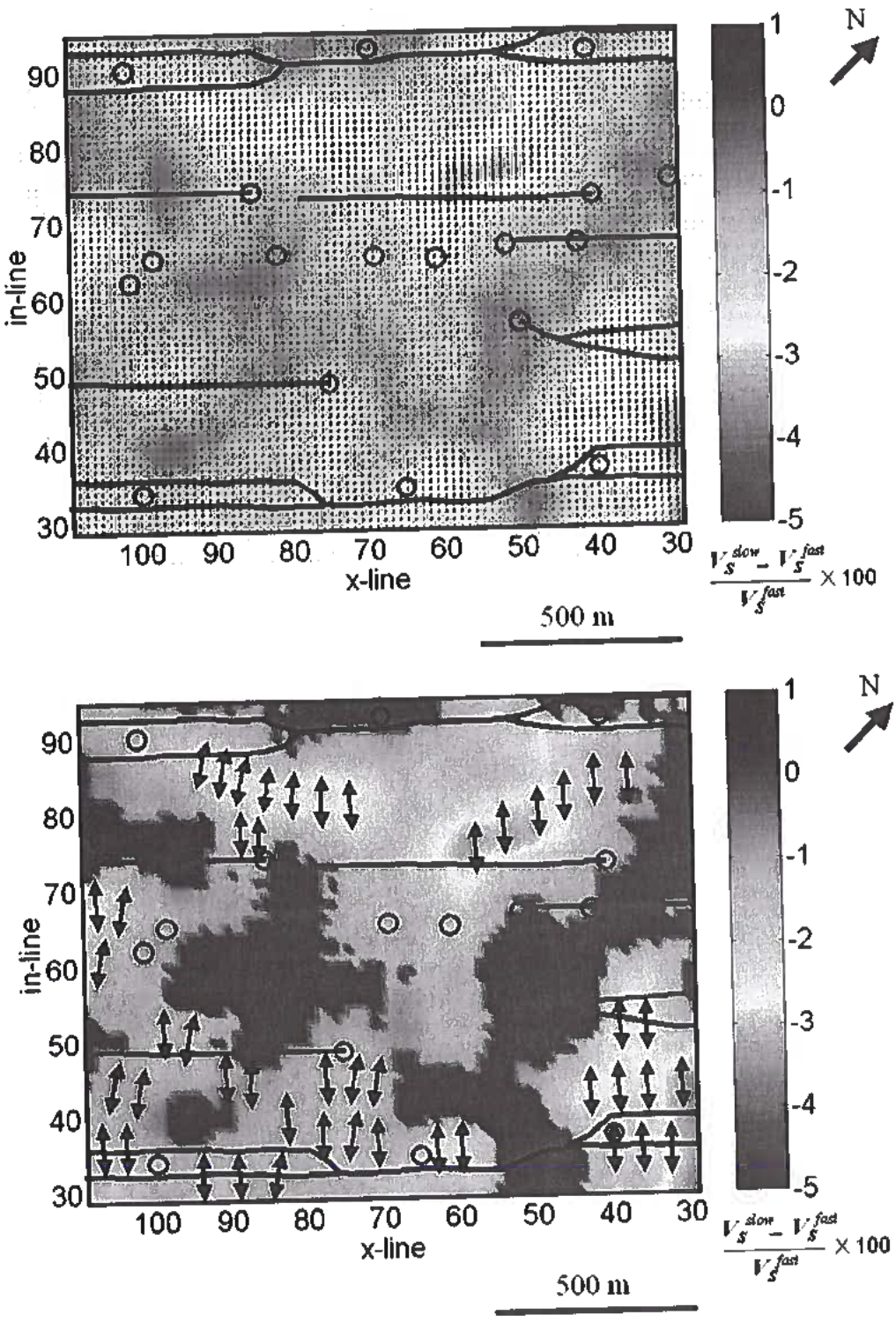

FIG. 7.3. Top: Shear splitting and fast polarization direction estimates at every CDP. Bottom: splitting values above one standard deviation from zero with average polarization directions indicated by large black arrows.

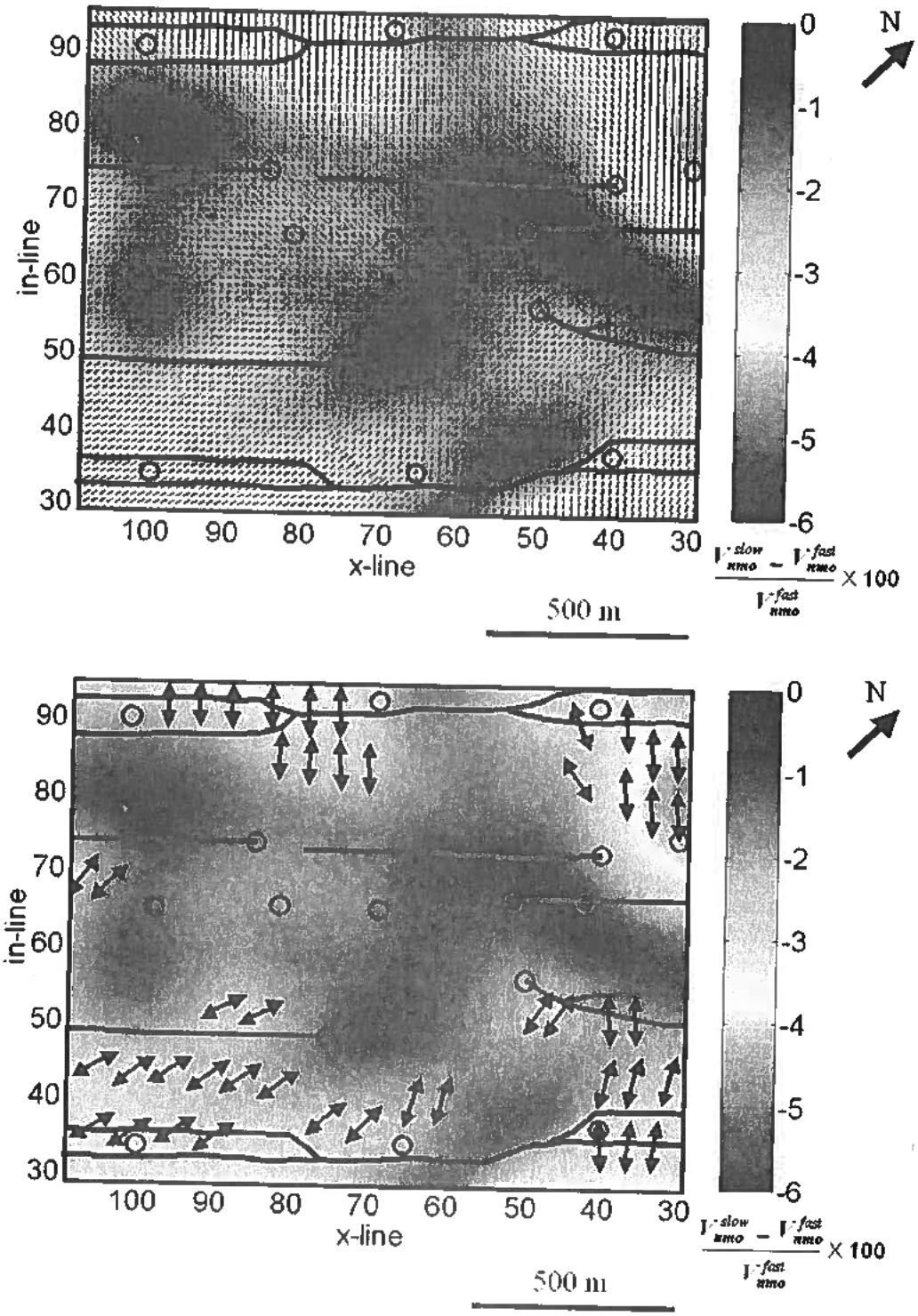

FIG. 7.4. Top: Fractional difference between fast and slow P-NMO velocity with fast NMO azimuth at every CDP. Bottom: map with average fast azimuth directions indicated by large black arrows

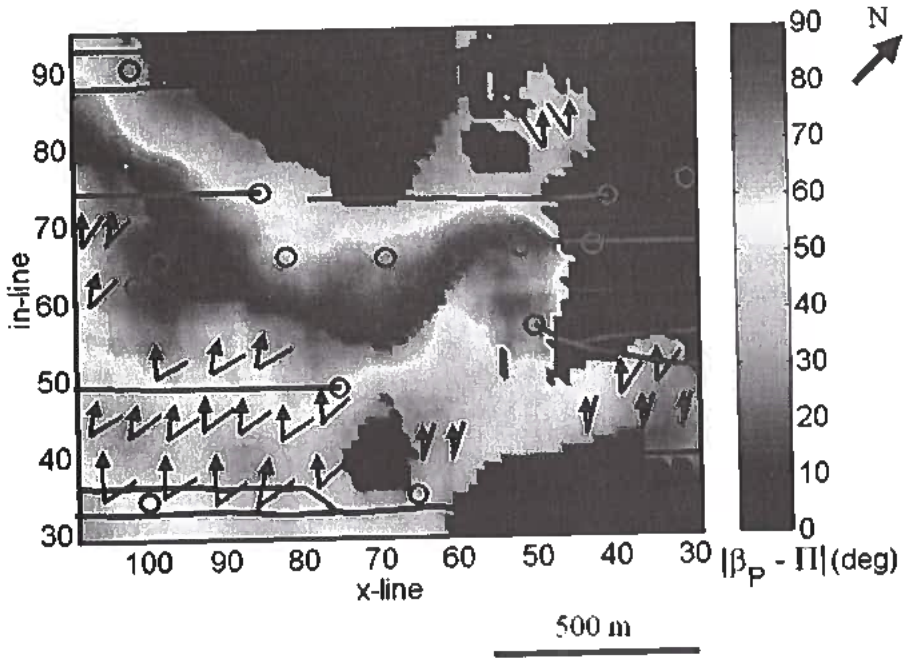

FIG. 7.5. Differences above one standard deviation between the fast P-NMO azimuth (β_P) and the fast shear polarization (Π) in degrees. Areas in dark blue have been zeroed because they are within one standard deviation of zero. In areas where $|\beta_P - \Pi|$ is significant the orientation of the P-NMO fast azimuth and fast S-wave polarization are indicated by line segments and arrows respectively.

shear polarization direction, we can infer that a more complex fracture model is required to explain the data in the lower portion of the survey. The next three subsections will introduce models of increasing complexity to explain the different features observed in the P- and S-wave data.

7.2.2 Interpretation under the HTI symmetry assumption

The model of a single set of rotationally invariant fractures in an isotropic background results in a rock with HTI (transversely isotropic with a horizontal symmetry axis) symmetry (see Chapter 3). Using the linear-slip theory, the elastic compliance matrix (**S**) of the HTI fractured rock can be written as shown in equation (3.8). Inverting the compliance matrix, the stiffness matrix can be obtained as:

$$\mathbf{C} = \begin{pmatrix} M(1-\Delta_N) & \lambda(1-\Delta_N) & \lambda(1-\Delta_N) & 0 & 0 & 0 \\ \lambda(1-\Delta_N) & M(1-l^2\Delta_N) & \lambda(1-l\Delta_N) & 0 & 0 & 0 \\ \lambda(1-\Delta_N) & \lambda(1-l\Delta_N) & M(1-l^2\Delta_N) & 0 & 0 & 0 \\ 0 & 0 & 0 & G & 0 & 0 \\ 0 & 0 & 0 & 0 & G(1-\Delta_T) & 0 \\ 0 & 0 & 0 & 0 & 0 & G(1-\Delta_T) \end{pmatrix},$$

where $M = \lambda + 2G$, $l = \lambda/M$, and λ and G are the Lamé parameter and shear modulus of the isotropic background rock, respectively (Schoenberg and Sayers, 1995). The parameters Δ_N and Δ_T are defined as

$$0 \leq \Delta_N \equiv \frac{Z_N M}{1 + Z_N M} \leq 1, \tag{7.1}$$

and

$$0 \leq \Delta_T \equiv \frac{Z_T G}{1 + Z_T G} \leq 1, \tag{7.2}$$

where Z_N and Z_T are the normal and tangential compliances defined in Chapter 3.

The parameters Δ_N and Δ_T are the normal and tangential weakness of the fracture system (respectively), and represent a reduction in the stiffness of the rock due to the presence of the fractures. If there are no fractures in the rock ($Z_N = Z_T = 0$) the weaknesses (7.1) and (3.7) are zero. If the rock is infinitely fractured ($Z_N, Z_T \to \infty$), the weaknesses tend towards unity.

Using the linear slip parameterization of the stiffness matrix, Bakulin et al. (2000a) obtained the exact expressions for the anisotropic parameters of the HTI rock as a function of the fracture weaknesses (7.1) and (3.7). In the limit of weak anisotropy, the expressions for the anisotropic parameters take the linearized forms:

$$\epsilon^{(V)} = -2g(1-g)\Delta_N, \tag{7.3}$$

$$\delta^{(V)} = -2g[(1-2g)\Delta_N + \Delta_T], \tag{7.4}$$

and

$$\gamma^{(V)} = -\frac{\Delta_T}{2}, \tag{7.5}$$

where $g = V_S^2/V_P^2$ is the ratio of the squared S- and P-wave velocities in the isotropic background (the "anellipticity" parameter $\eta^{(V)}$ has also been defined for HTI rocks by Tsvankin (1997b), however, it will not be used in this Chapter).

The linearized $\gamma^{(V)}$ parameter can be estimated from the difference of the fast and slow velocities of vertically propagating S-waves as

$$\gamma^{(V)} \approx \frac{V_S^{slow} - V_S^{fast}}{V_S^{fast}}, \tag{7.6}$$

whereas the linearized parameter $\delta^{(V)}$ can be obtained from the difference of the fast and slow NMO velocity directions as

$$\delta^{(V)} \approx \frac{V_{P,nmo}^{slow} - V_{P,nmo}^{fast}}{V_{P,nmo}^{fast}}, \tag{7.7}$$

The advantage of expressions (7.3)-(7.5) (and the equivalent for arbitrary strength anisotropy) is that they provide a way of calculating the range of possible values of the anisotropic parameters based on the physically realizable ranges of Δ_N, Δ_T and V_P/V_S. Furthermore, from equations (7.3)-(7.5) it is straightforward to prove that in the weak anisotropy limit the anisotropic parameters are related by the constraint:

$$\gamma^{(V)} = \frac{1}{4g}\left(\delta^{(V)} - \epsilon^{(V)}\frac{1-2g}{1-g}\right). \tag{7.8}$$

The previous constraint indicates that if this fracture model is adequate for the Weyburn reservoir rocks and an estimate of V_P/V_S is available, the $\epsilon^{(V)}$ parameter can be calculated from the $\gamma^{(V)}$ parameter, estimated from the split shear-waves, and the $\delta^{(V)}$ parameter, estimated from the P-wave NMO ellipse.

Figure 7.6 shows the range of physically possible HTI anisotropic parameters (black dots) overlain by the corresponding parameters estimated from the P-wave NMO and vertical S-wave velocities of Weyburn data (colored circles). The red circles in the $\gamma^{(V)} - \delta^{(V)}$ plane are values of $\gamma^{(V)}$ and $\delta^{(V)}$ taken directly from the maps in Figures 7.3 and 7.4, respectively (all selected values are above one standard deviation from zero). The colored circles in the $\epsilon^{(V)} - \delta^{(V)}$ plane are obtained by calculating $\epsilon^{(V)}$ from the $\gamma^{(V)}$ and $\delta^{(V)}$ estimates using equation (7.8). The cyan circles are the values of $\epsilon^{(V)}$ calculated assuming $V_P/V_S = 2.58$, and the blue and green circles result

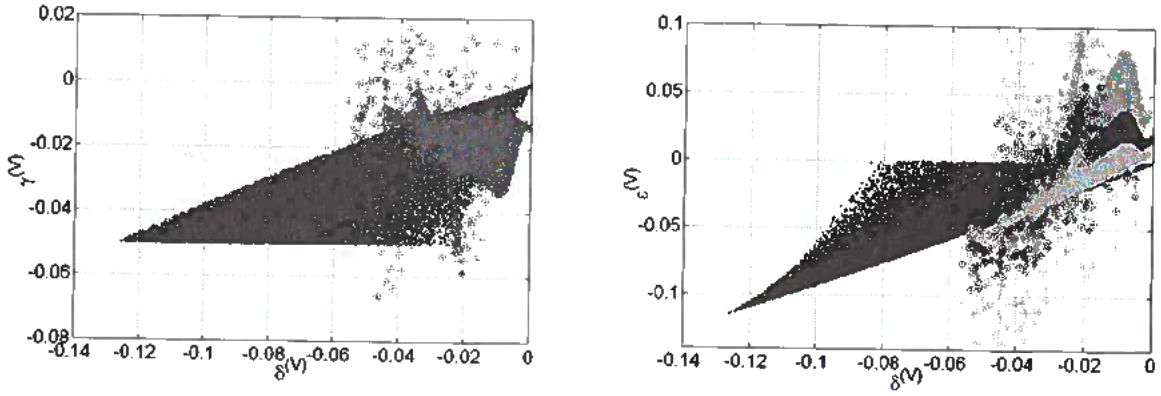

FIG. 7.6. Possible ranges of HTI models (black dots) overlain by the parameters estimated from the P-wave NMO and S-wave velocities of Weyburn data. Red circles in the $\gamma^{(V)} - \delta^{(V)}$ plane are taken directly from the maps of shear splitting and fractional difference between fast and slow P-NMO velocity. The cyan, blue and green circles in the $\epsilon^{(V)} - \delta^{(V)}$ correspond to values of $\epsilon^{(V)}$ calculated from equation (7.8) assuming $V_P/V_S = 2.58$, $V_P/V_S = 2.00$ and $V_P/V_S = 1.69$, respectively.

from calculating $\epsilon^{(V)}$ assuming $V_P/V_S = 2.00$ and $V_P/V_S = 1.69$, respectively.

The black dots in Figure 7.6 are 200,000 realizations of $\epsilon^{(V)}$, $\delta^{(V)}$ and $\gamma^{(V)}$ resulting from uncorrelated, random draws of Δ_N, Δ_T and V_P/V_S. Each combination of the fracture weaknesses and the $V_P - V_S$ ratio is drawn from the ranges: $0 < \Delta_T < 0.1$, $0 < \Delta_N < 1$ and $1.5 < V_P/V_S < 2.9$, and then substituted into the expressions for arbitrary anisotropy strength to calculate the anisotropic parameters. It is important to note that although Chapter 3 proves that the use of the linear slip parameterization some times results in errors when predicting the changes of the anisotropic parameters with saturation, it can still be used to predict the coarse bounds of possible HTI models.

The significance of Figure 7.6 is that it shows there are a large number of points in the data that do not fall within the bounds of possible HTI models. This should be expected because the non-HTI consistent zones in the survey area, in which the fast S-wave polarization the fast P-NMO azimuth do not coincide, have been included in the plots. Figure 7.7 shows that if all the points from zones with different fast P-NMO azimuth and S-wave polarization are removed, the points outside the HTI range decreases.

To estimate the spatial distribution of HTI-consistent zones, the survey area location of those points that fall within the bounds of feasible HTI models is plotted in red in the map shown in Figure 7.8. Hence, within the HTI context it can be interpreted that the zones marked in red there is a single set of fractures oriented in

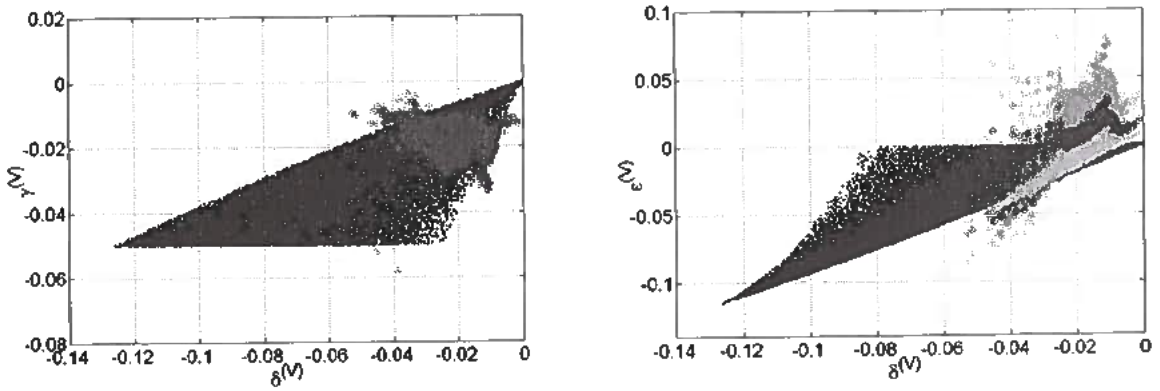

FIG. 7.7. $\gamma^{(V)} - \delta^{(V)}$ and $\epsilon^{(V)} - \delta^{(V)}$ planes calculated under the same conditions as Figure 7.6, but removing points in which the fast S-wave polarization the fast P-NMO azimuth do not coincide.

the off-trend direction. Figure 7.9 shows how two of the fracture trends observed in the borehole imager and core data trend nearly parallel to the fast-shear polarization direction in the HTI-consistent zones indicated in Figure 7.8. The red trend is the one that best matches the fast-polarization direction and would be the best candidate to model the data using the HTI assumption.

7.2.3 Interpretation under the orthorhombic symmetry assumption

After considering the case of a single set of aligned fractures, this section investigates which zones in the reservoir area are consistent with orthorhombic symmetry models that contain more than one of fracture set. The procedure to characterize the orthorhombic zones will be the same as the one applied for the HTI case. However, a larger number of anisotropic parameters have to be calculated to estimate all the feasible fracture models.

In the orthorhombic models considered here, the rock is composed of two orthogonal sets of rotationally invariant fractures embedded in an elastically isotropic background. Because the fractures are vertical the model is assumed to be non-tilted orthorhombic.

Tsvankin (1997a) introduced a parameterization for orthorhombic media that includes seven anisotropic parameters. For the specific case of a rock composed of two orthogonal fracture sets, Bakulin et al. (2000b) obtained the exact expressions for the Tsvankin parameters as a function of the fracture weaknesses of set "1"(Δ_{N1}, Δ_{T1}) and set "2" (Δ_{N2}, Δ_{T2}). In the limit of weak anisotropy, the anisotropic parameters that control wave propagation in the vertical plane orthogonal to set "2"

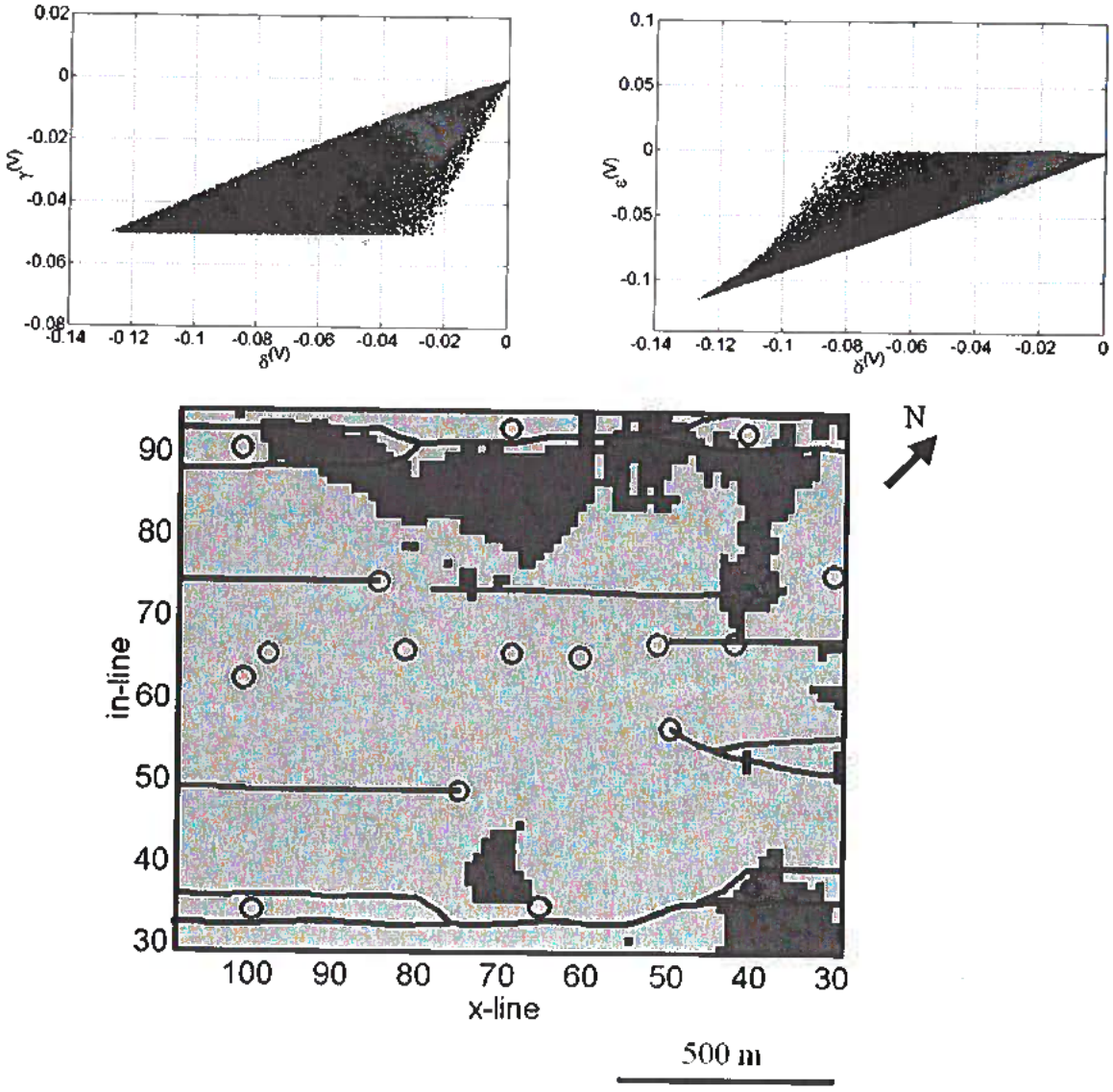

FIG. 7.8. Top: Weyburn data-derived values of $\epsilon^{(V)}$, $\delta^{(V)}$ and $\gamma^{(V)}$ that fall within the range of possible HTI models. $\epsilon^{(V)}$ is estimated from V_P/V_S values measured from vertical P- and S-wave travel times. Bottom: Survey map indicating HTI-consistent zones in red.

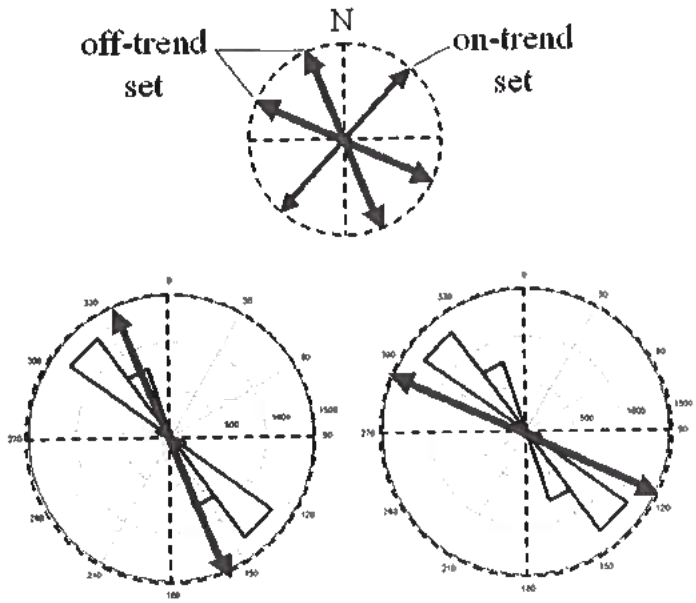

FIG. 7.9. Orientations of hypothetical single sets of fractures (arrows) that are consistent with the some of the fracture orientations observed on cores and borehole imagers. The bottom rose plots compare the orientation of the blue and red fracture sets with the fast-shear polarization direction in the HTI-consistent zones.

are

$$\epsilon^{(1)} = -2g(1-g)\Delta_{N2}, \tag{7.9}$$

$$\delta^{(1)} = -2g[(1-2g)\Delta_{N2} + \Delta_{T2}], \tag{7.10}$$

and

$$\gamma^{(1)} = -\frac{\Delta_{T2}}{2}, \tag{7.11}$$

where $g = V_S^2/V_P^2$ is the ratio of the squared S- and P-wave velocities in the isotropic background. In the vertical plane orthogonal to set "1" the anisotropic parameters are:

$$\epsilon^{(2)} = -2g(1-g)\Delta_{N1}, \tag{7.12}$$

$$\delta^{(2)} = -2g[(1-2g)\Delta_{N1} + \Delta_{T1}], \tag{7.13}$$

and

$$\gamma^{(2)} = -\frac{\Delta_{T1}}{2}. \tag{7.14}$$

The seventh parameter ($\delta^{(3)}$) is defined in the horizontal plane and will not be used in the analysis presented below.

For weak anisotropy, the difference between the $\gamma^{(2)}$ and $\gamma^{(1)}$ parameter is equal to the shear-wave splitting parameter at vertical incidence (Tsvankin, 2001), and can be estimated from the S-wave velocities as

$$\gamma^{(2)} - \gamma^{(1)} \approx \frac{V_S^{slow} - V_S^{fast}}{V_S^{fast}}. \tag{7.15}$$

The difference $\delta^{(2)} - \delta^{(1)}$ can be obtained from the difference of the fast and slow NMO velocity directions as

$$\delta^{(2)} - \delta^{(1)} \approx \frac{V_{P,nmo}^{slow} - V_{P,nmo}^{fast}}{V_{P,nmo}^{slow} + V_{P,nmo}^{fast}}. \tag{7.16}$$

From equations (7.9)-(7.14) it is straightforward to prove that in the weak anisotropy limit the six anisotropic parameters presented above are related by the constraint (Bakulin et al., 2000a):

$$\gamma^{(2)} - \gamma^{(2)} = \frac{1}{4g}\left[\left(\delta^{(2)} - \delta^{(1)}\right) - \left(\epsilon^{(2)} - \epsilon^{(1)}\right)\frac{1-2g}{1-g}\right]. \tag{7.17}$$

Hence, the difference $\epsilon^{(2)} - \epsilon^{(1)}$ can be calculated from the values of $\gamma^{(2)} - \gamma^{(1)}$ estimated from the split shear-waves, and from the values of $\delta^{(2)} - \delta^{(1)}$ estimated from the P-wave NMO ellipse. With equations (7.9)-(7.14) it is possible to calculate the range of

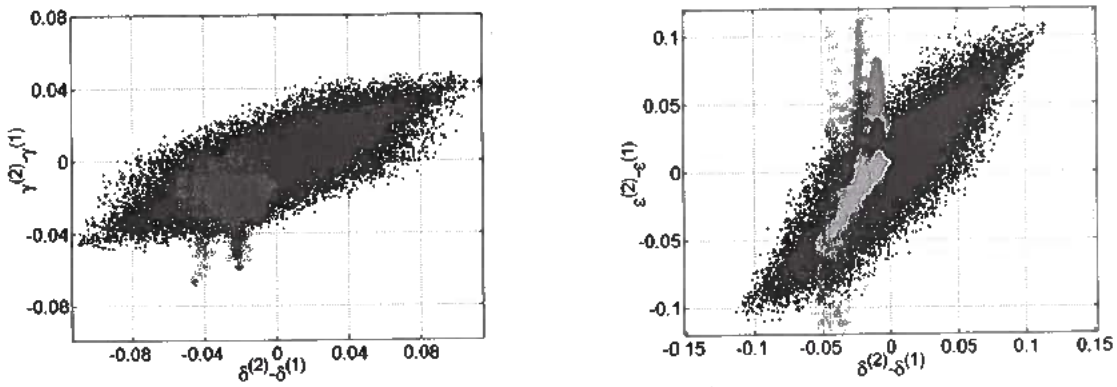

FIG. 7.10. Possible ranges of orthorhombic models (black dots) overlain by the parameters estimated from the P-wave NMO and S-wave velocities of Weyburn data. Red circles in the "$\gamma - \delta$" plane are taken directly from the shear splitting and fractional difference between fast and slow P-NMO velocity. The cyan, blue and green circles in the "$\epsilon - \delta$" plane correspond to values of $\epsilon^{(2)} - \epsilon^{(1)}$ calculated from equation (7.17) assuming $V_P/V_S = 2.58$, $V_P/V_S = 2.00$ and $V_P/V_S = 1.69$, respectively.

feasible orthorhombic parameters and compare them with the predictions obtained from the seismic data in the same way that was done for the HTI model above.

Figure 7.10 shows the range of physically possible orthorhombic anisotropic parameters (black dots) overlain by the corresponding parameters estimated from the P-wave NMO and vertical S-wave velocities (colored circles). The cyan, blue and green circles in the "$\epsilon - \delta$" plane correspond to values of $\epsilon^{(2)} - \epsilon^{(1)}$ calculated with equation (7.8) assuming $V_P/V_S = 2.58$, $V_P/V_S = 2.00$ and $V_P/V_S = 1.69$, respectively.

Note that Figure 7.10 has a larger model space than the HTI case due to the larger number of degrees of freedom in the orthorhombic model. The lower left quadrant in the '$\gamma - \delta$" and "$\epsilon - \delta$" planes represents the region in which the fracture set "1" (with weaknesses Δ_{N1} and Δ_{T1}) dominates over fracture set "2". In the Weyburn data set the dominant fracture set is the one oriented in the off-trend direction that connects the injectors and producers.

The top part of Figure 7.11 shows plots calculated with the V_P/V_S values measured from vertical P- and S-wave travel times, and after removing all points in which the fast P-NMO and S-wave polarization direction do not coincide. The map in the bottom part of Figure 7.11 shows in red color the regions in the survey area that are consistent with the orthorhombic assumption. Note that the "orthorhombic map" contains all the HTI zones presented in Figure 7.8. This should be expected since the HTI model is a special orthorhombic case in which the weaknesses of one of the

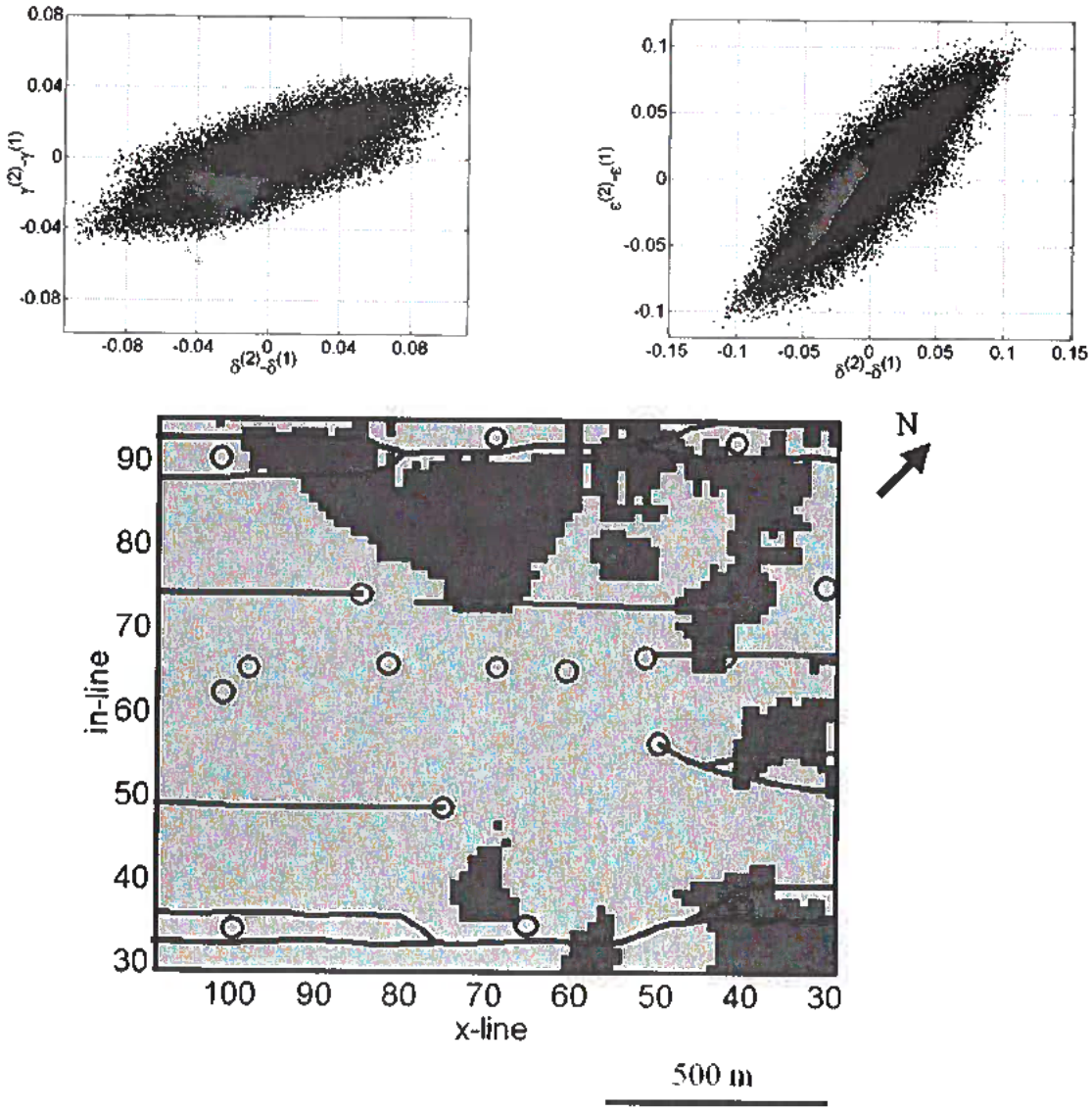

FIG. 7.11. Top: Weyburn data-derived values of the anisotropic parameters that fall within the range of possible orthorhombic models. $\epsilon^{(2)} - \epsilon^{(1)}$ is estimated from V_P/V_S values measured from vertical P- and S-wave travel times. Bottom: Survey map indicating orthorhombic-consistent zones in red.

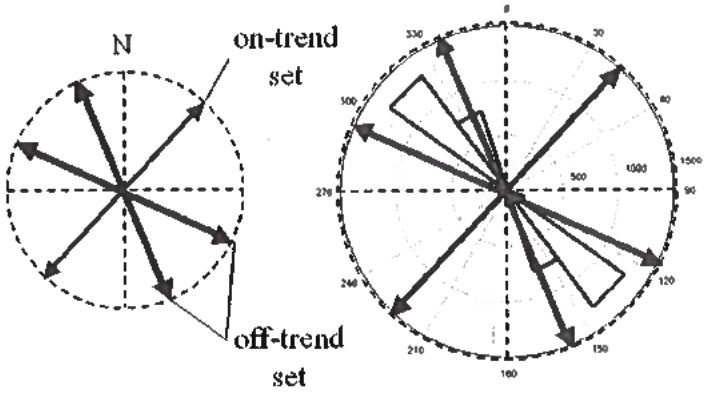

FIG. 7.12. Orientations of fracture sets (arrows) that are consistent with observations on cores and borehole imagers and that could result in an orthorhombic symmetry rock. The sets with red arrows are assumed to have identical fracture densities and compliances.

fracture sets are set to zero.

Figure 7.12 shows how the fracture orientations observed from core and borehole imager data can be consistent with the orthorhombic symmetry assumption. If the fractures shown in red are rotationally invariant and have the same fracture density and compliances, they will behave as an average fracture set in the off-trend direction and the rock will have orthorhombic symmetry with a vertical symmetry plane that bisects the two red fracture sets. Adding a perpendicular fracture set (black) will not change the symmetry of the rock further. Hence, the model shown in figure 7.12 is indistinguishable from two orthogonal fracture sets. The direction of the fast S-wave polarization and fast P-NMO velocity will be determined by the dominant fracture set shown in red.

7.2.4 Considerations about symmetries lower than orthorhombic

As it was shown in Chapter 4 two or more sets of rotationally invariant fractures that are not perpendicular to each other and have different fracture compliances, will result in a rock with a symmetry lower than orthorhombic. If all the fractures are rotationally invariant and *vertical*, a horizontal symmetry plane will always exist for any number of fracture sets, and the model will have monoclinic symmetry. However, a complete characterization of the rock's elastic parameters from seismic data is *not*

possible for more than two *vertical* fracture sets (Grechka and Tsvankin, 2002).

Despite the complexity of models with two or more fracture sets, they can explain the different orientations of the fast S-wave polarization and fast P-NMO azimuth observed in the lower section of the survey. Grechka et al. (2000) have introduced a parameterization for monoclinic media with a horizontal symmetry plane that extends Tsvankin's orthorhombic parameterization. The monoclinic parameterization is convenient because it preserves the parameters defined in equations (7.9)-(7.14) and adds three more anisotropic parameters: $\zeta^{(1)}$, $\zeta^{(2)}$ and $\zeta^{(3)}$, which are responsible for the rotation of the S_1-, S_2- and P-wave NMO ellipses with respect to the fast shear polarization direction.

In the weak anisotropy approximation, the angle of the semi-axes of the P-NMO ellipse with respect to the S-wave polarization directions is given by:

$$\beta_P = \frac{2\zeta^{(3)}}{\delta^{(2)} - \delta^{(1)}}, \tag{7.18}$$

where $\delta^{(2)}$ and $\delta^{(1)}$ are defined in the same way as in the orthorhombic parameterization. Hence, for orthorhombic and HTI symmetries, in which $\zeta^{(3)} = 0$, the NMO ellipse coincides with the S-wave polarization directions as stated previously.

The Figures 4.10-4.12 presented in Chapter 4 showed the rotation angle of the NMO ellipses for the S_1-, S_2- and P-wave modes, for a rock model with two sets of non-orthogonal, vertical penny-shaped cracks. The modeling was done for a fluid saturated rock under conditions of *equilibrated pore pressures*, for several lithologies, different values of isotropic porosity, different angles of separation between fracture sets, and different ratios of the crack densities of the two sets. Since in *all* cases the value of β_P was less than two degrees, the modeling suggests that the large differences between fast P-NMO and S-wave polarization directions observed on Weyburn data (Figure 7.5), *cannot* be explained with two sets of rotationally invariant fractures under conditions of equilibrated pore pressures.

Larger differences between the fast P-NMO and S-wave polarization directions can be obtained considering all the possible combinations of the normal and tangential weaknesses, as it was done previously for the HTI and orthorhombic cases. Figure 7.13 shows the results of using the linearized expressions of $\zeta^{(3)}$, $\delta^{(1)}$ and $\delta^{(2)}$ as a function of the fracture weaknesses (Bakulin et al., 2000c), to model the fast S-wave polarization and P-NMO directions for a rock model with two fracture sets with 60° of separation. The plot shows the polarizations (red line) and fast P-NMO azimuths (black dots) measured with respect to the dominant fracture set (set 1) as a function of the ratio of the tangential compliances, Z_{T1}/Z_{T2}.

The fast shear polarization tends rapidly towards the more compliant fracture set (set 1) as Z_{T1}/Z_{T2} increases. Most of the models with $Z_{N1}/Z_{N2} > 1$, lie above the white dotted line and have fast P-NMO directions that tend towards the dominant

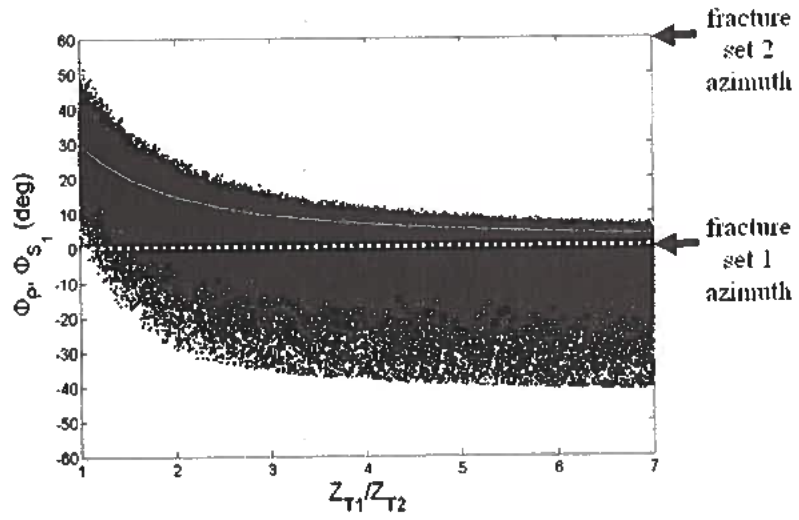

FIG. 7.13. Plot of modeled fast S-wave polarization (red line) and fast P-NMO azimuths (black dots) measured with respect to the dominant fracture set (set 1), as a function of Z_{T1}/Z_{T2}.

fracture direction as Z_{T1}/Z_{T2} increases. The large number of models below the dotted line correspond to cases in which $Z_{N1}/Z_{N2} < 1$. These models, however, may not be physically realizable when the tangential fracture compliance of the first set is much larger than the second set ($Z_{T1}/Z_{T2} >> 1$).

Note that when the two fracture sets have equal tangential compliances ($Z_{T1}/Z_{T2} = 1$) the fast S-wave polarization bisects the angle between the two fractures. If the normal compliances are also equal, the rock becomes orthorhombic and the fast P-NMO azimuth is no longer rotated with respect to the shear polarization directions. Hence, as mentioned above in the "orthorhombic section", the two non-orthogonal fracture sets can be reconciled with observations in the upper part of the survey assuming equal normal and tangential compliances of the fracture sets.

The relevance of Figure 7.13 for interpreting Weyburn data is that it shows that most of the models with $Z_{T1}/Z_{T2} > 1$ and $Z_{N1}/Z_{N2} > 1$ (above the dotted line) have S-wave polarization directions and fast P-NMO azimuths that lie *between* the strikes of the two fracture sets where the angle between them is less than 90°. Only models with $Z_{N1}/Z_{N2} < 1$, which are probably the less realizable, allow the fast P-NMO and fast shear polarization to fall on opposite sides of the dominant fracture set.

Based on the results from Figure 7.13, Figure 7.14 compares, by pairs, the orientations of the fracture sets observed in core and borhole imager data (arrows) with

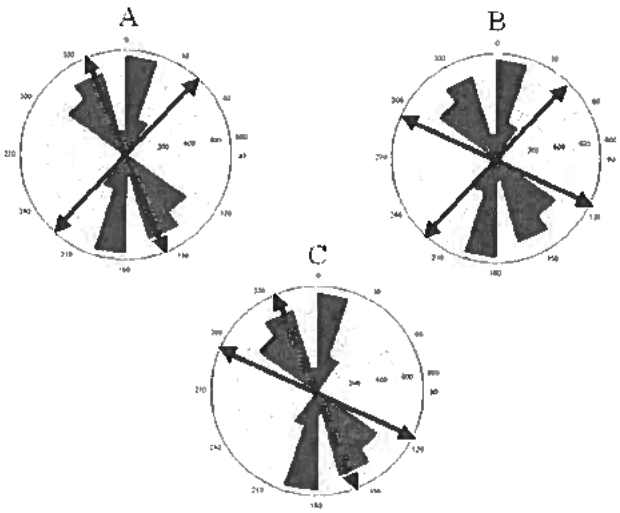

FIG. 7.14. Rose plots of S-wave polarization (red) and P-NMO azimuth (blue).

the fast S-wave polarization (red) and P-NMO azimuth (blue) in the zones where they are not parallel. In none of the three combinations do the fast S-wave polarization and P-NMO azimuth fall within the fracture strikes where the angle between them is less than 90°. Combination (C) is consistent with the data if one assumes one of the models in which the fast polarization and the P-NMO azimuth fall on opposite sides of a dominant fracture set (dashed arrow). However, the question remains if such models are realizable.

The results for two non-orthogonal fracture sets presented so far suggest that, with the exception of model (C) in Figure 7.14, it is necessary to include a third rotationally invariant set or consider a more complex fracture rheology to explain the zones in which the fast S-wave polarization does not match the fast P-NMO azimuth. Instead of attempting to parameterize a more complicated model we can interpret, by exclusion of the simpler models, that the zones in the lower section of the survey area correspond to three rotationally invariant fracture sets or a smaller number of sets that have a more complex rheology.

Grechka et al. (2001) have shown that a single set of fractures with the most general rheology according to linear slip theory, in general may induce differences in the fast P-NMO azimuth and the fast shear polarization. These fractures are more complicated than the "monoclinic" micro-corrugated fractures described in Chapter 4, because their micro-structure couples vertical stresses to both normal *and* horizontal displacements.

The theory developed in Chapter 4 proved that fractures with microstructure that couples normal and vertical displacements will induce changes with saturation

in the splitting of vertically propagating S-waves. Therefore, the shear-wave time lapse analysis presented below can be used to constrain the fracture types found in the reservoir.

7.3 Shear-wave Time-lapse Analysis

The CO_2 injection processes performed at Weyburn field provides an excellent opportunity to apply the concepts developed in Chapter 4 regarding the variations of shear splitting with fluid saturation. Furthermore, because the fluid sensitivity of the shear-waves depends on the symmetry of the fractured rock, knowing which areas present fluid-sensitive shear-waves can help constrain the fracture types in the reservoir.

As shown in Chapter 7, estimates of the shear-wave splitting were performed from both travel-times and amplitudes. Because the travel-time estimates were obtained from a coarse vertical interval that is at least 10 times the thickness of the reservoir it is not possible to analyze the influence of the changes in saturation in the reservoir on the travel-time derived shear splitting. However, the amplitude estimates may be used because they sample changes in the shear splitting at the interface between the reservoir and the overburden.

As can be seen from Figures I.1-I.4, the monitor survey is noisier than the baseline. In order to assess the significance of any variations observed in the time-lapse experiment two measures of uncertainty were used. First, time-lapse variations in the amplitude of the reflectors in the overburden (where no changes should occur) were taken as a lower bound on the "background" noise level above which any changes must be interpreted. Second, the standard deviation of the shear-splitting estimated on each survey was used to calculate the standard deviation of the difference in the shear splitting, $\gamma_{monitor} - \gamma_{baseline}$. The latter estimate was almost always the largest of the two uncertainty measures, and was the one used to guide the interpretation of the time-lapse variations.

When the chosen standard deviation was compared to the magnitude of the "anomalies", it was found that all time-lapse variations in the shear splitting were smaller than one standard deviation in the difference. Had no other information about the injection process been available, it would have not made much sense to interpret the time-lapse data below the uncertainty level. However, data from production rates suggested that the lower section of the survey, which was interpreted earlier as the zone with lowest symmetry, was subject to an extensive fluid substitution process. This motivated the analysis of the largest anomalies in the shear splitting difference map to corroborate any correlation with zones in which large volumes of CO_2 were injected.

The top plot in Figure 7.15 shows the water (blue) and oil (green) production

rates at four horizontal producers in a three year period including the CO_2 injection interval that started on October 2000. The bold lines in each graph indicate the times of the baseline and monitor surveys. Note that the two producers in the lower part of the survey show a sharp increase in the oil production at mid year 2001, which indicates that the CO_2 is sweeping oil into the wells. In contrast, the horizontal wells in the upper part of the survey show no response at all.

The bottom map in Figure 7.15 shows the change in shear splitting calculated as (monitor-baseline). All values smaller than half a standard deviation are set to zero and not interpreted (cyan colored). Notice that the largest and more continuous anomalies are located in the lower part of the survey and correlate with the zones in which the S-wave polarization and fast P-NMO azimuth do not match. Furthermore, Figure 7.16 indicates that the largest volume of CO_2 has been injected into the lower portion of the survey.

If the zones with shear splitting time-lapse variation are interpreted as resulting from a fluid substitution processes, then Figure 7.15 suggests that the increase in oil production in the two horizontal wells is due to the migration of the CO_2 along the off-trend fracture direction. This interpretation is consistent with the observations done by Brown (2002) and Herawati (2001) on the P-wave volumes, in which time-lapse amplitude anomalies suggest a connection between the lower horizontal injectors and producers that show increased production (Figure 7.17).

The theory developed in Chapter 4 predicted that a single set of "monoclinic" fractures would be enough to induce an increase in the shear splitting when the compressibility of the saturating fluid increases. Because we know from the production data that the zones in the lower part of the survey have been saturated with CO_2, we can assume that the fluid substitution process has reduced the compressibility of the effective fluid mixture in the zone where the large splitting anomalies are observed in Figure 7.15. Because the splitting parameter was defined as negative, and the time-lapse map was calculated as monitor - baseline, the mechanism described in Chapter 4 predicts that negative anomalies should occur in the map shown in figure 7.15. Two of the largest anomalies in the map, located near x-line 100 and x-line 75 have a negative sign, whereas the anomaly located near x-line 40 has a positive sign.

The anomalies with negative sign are consistent with the mechanism of the "monoclinic" fracture described in Chapter 4, since the reflectivity of the S_1 mode remains largely unchanged while the S_2 amplitude decreases. However, the time-lapse change in the zone near x-line 40 cannot be explained by the "monoclinic" model.

Duranti (2001) also reported shear splitting values that decreased after an injection process due to an increase of the S_2 velocity. Duranti speculated that a pressure decrease in that zone would result in fracture closure and reduction of the anisotropy. However, the anomaly near x-line 40 at Weyburn field is too close to the injector to assume that a pressure decrease may be responsible for the sign of the anomaly.

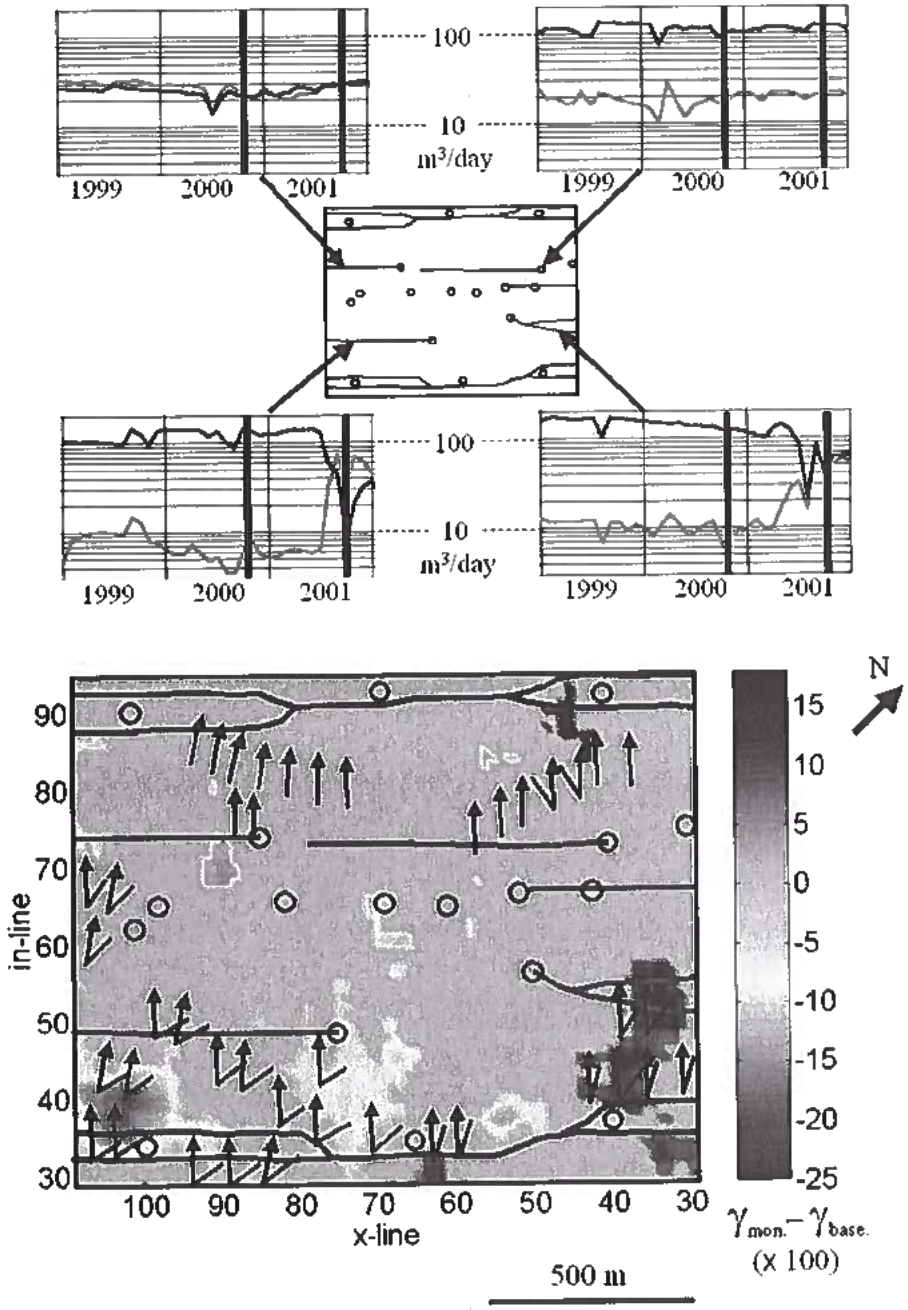

FIG. 7.15. Top: Water (blue) and oil (green) production at four horizontal wells in a three year period. The bold lines in each plot indicate the times of the baseline and repeat. Bottom: time-lapse change in the amplitude-derived shear splitting, calculated as Repeat-Baseline. Zones in cyan correspond to changes that are below half a standard deviation on the difference.Arrows and line segments indicate the fast S-wave polarization and fast P-NMO azimuth, respectively.

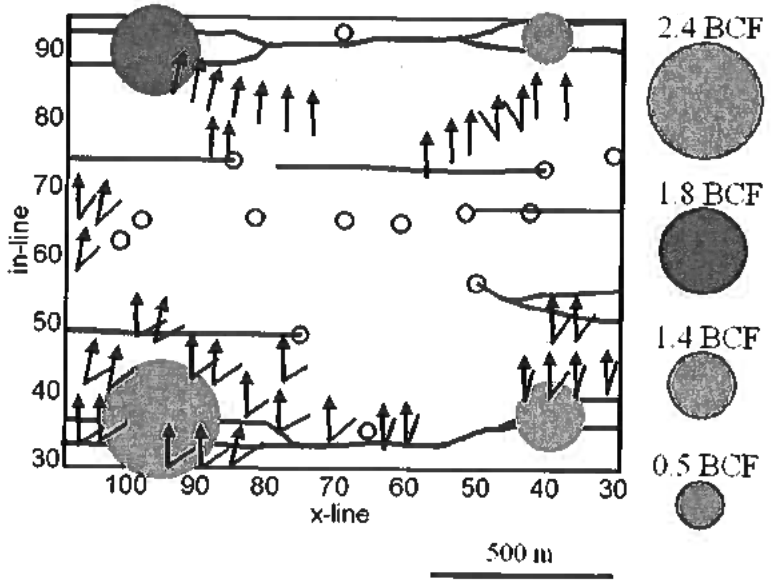

FIG. 7.16. Volume of CO_2 injected by each horizontal well in billion cubic feet. Arrows and line segments indicate the fast S-wave polarization and fast P-NMO azimuth, respectively.

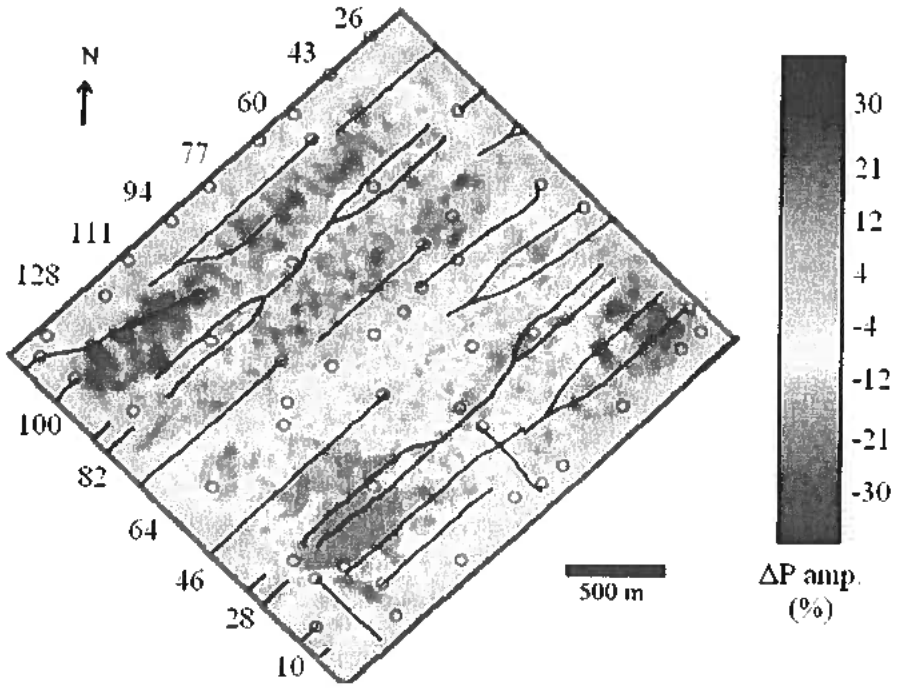

FIG. 7.17. P-wave amplitude time-lapse anomalies from Herawati (2001).

Due to the three possible fracture sets present at Weyburn, adding more structure to the model by complicating at will the rheology of the fractures allows enough free parameters to match the sign of any anomaly, following the modeling process described in Chapter 4. In order to avoid over-interpreting the data, the most conservative interpretation is to recognize that the zones with largest anomalies in the S-wave time-lapse analysis coincide with the areas that in the baseline analysis *could not* be explained using HTI or orthorhombic symmetry models. This observation is consistent with the predictions of Brown and Korringa's theory that the symmetry of the rock has to be lower than orthorhombic or should at least have tilted symmetry planes to have fluid-sensitive shear-waves.

It is important to note that the monoclinic model resulting from two, three or more vertical non-orthogonal, rotationally invariant fractures, does not allow fluid-sensitive shear-waves (see Chapter 4). This results from the fact that such a model has a horizontal symmetry plane that does not allow the fracture-normal to vertical coupling necessary to have fluid-dependent shear compliances. On the other hand, a single set of "monoclinic" fractures will explain the S-wave splitting changes with saturation, but it cannot explain the difference between the fast P-NMO and the S-wave polarization direction because the model has a vertical symmetry plane that coincides with both orientations. Therefore, when all the evidence from the baseline and time-lapse analysis is merged, I conclude that the simplest models that is consistent with the data in the *lower* section of the survey is two sets of "monoclinic" fractures or one set of the "general" fractures introduced by Grechka et al. (2001).

7.4 Discussion and Conclusions

The work presented in this chapter has provided a semi-quantitative interpretation of the post-stack S-waves and pre-stack P-waves acquired over Weyburn field. The interpretation is based on a model-driven classification of the estimates obtained from the seismic data aided by information from borehole imagers, cores and production data.

The analysis shows that the HTI model of a single set of fractures is consistent with only a portion of the data mostly located in the upper section of the survey above in-line 70. The zones consistent with orthorhombic fracture models are also constrained mostly to the upper section of the survey and include all the HTI areas as special cases of orthorhombic symmetry. Based on the evidence of three possible fracture sets, the preferred model for the orthorhombic areas is one with three rotationally invariant fractures in which the two off-trend fracture sets have equal compliances (see Figure 7.12). This model would be indistinguishable from the simpler case of two orthogonal fracture sets with the off-trend set being the dominant one.

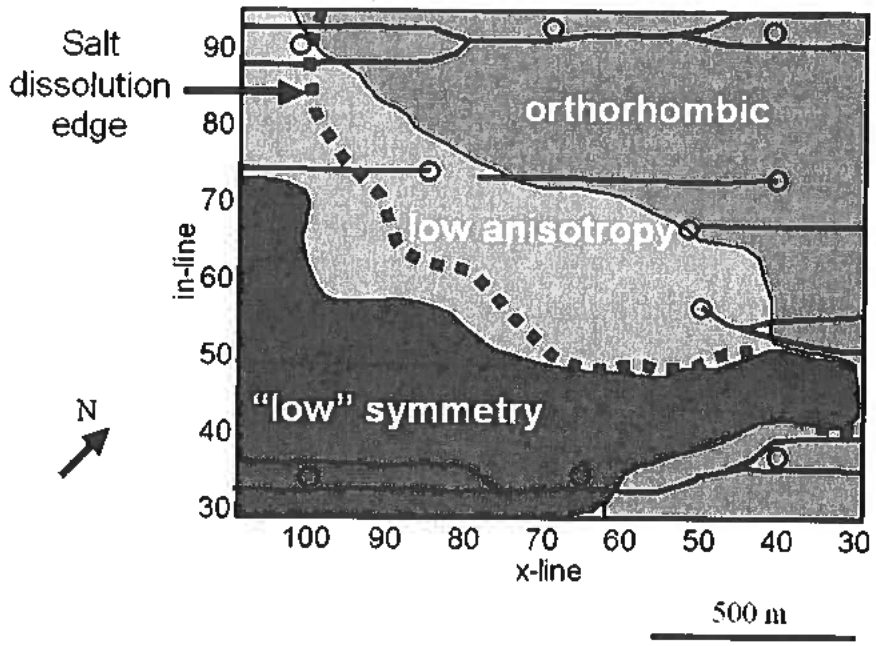

FIG. 7.18. Survey area classification indicating the location of the salt dissolution edge interpreted by Reasnor (2001) at the Prairie Evaporite.

Most of the zones in the lower portion of the survey show evidence that the rocks are elastically more complex than in the upper survey area. The existence of time-lapse variations in the shear splitting suggests the rheology of the fractures is more complicated than that of rotationally invariant fractures. Furthermore, the correlation of the time-lapse anomalies with areas that are not orthorhombic-consistent gives support to the theoretical prediction that the shear-wave sensitivity to fluids is tied to lower-than-orthorhombic symmetry models.

Based on the available data, a classification of the reservoir in the survey area can be done as shown in Figure 7.18. Reasnor (2001) has provided evidence that salt dissolution has occured below the reservoir, at the Devonian age Prairie Evaporite. The edge of the salt dissolution zone interpreted by Reasnor on the P-wave data is overlain in the classification map shown in Figure 7.18, where the salt-withdrawal area is located south of the salt-dissolution edge.

Notice that the "low"-symmetry areas coincide with the zones of salt withdrawal, whereas the orthorhombic area coincides with areas where salt remains in the Prairie Evaporite. This correlation suggests that the salt withdrawal modified the stress state in reservoir, resulting in different fracturing regimes south and north of the salt dissolution edge.

Chapter 8

SUMMARY AND RECOMMENDATIONS

8.1 Summary

This thesis has addressed several theoretical and applied topics on the characterization of fractured reservoirs. On the theoretical side I have presented work on fluid substitution theories and on the integration of pressure-transient experiments into seismic reservoir characterization. The lessons from the fluid substitution theories have been applied to the characterization from seismic of the fractured reservoir at Weyburn Field, Canada.

The analysis done on the fluid substitution theories has two major implications. The first one is that the shear-wave modulus of vertically propagating S-waves may be sensitive to changes in fluid saturation for certain models of fractured rock. Although it is well known that S-waves traveling at oblique angles from the fracture plane may have fluid-dependent moduli, this research indicates that fractures that couple vertical, tangential tractions to normal displacements will induce fluid-dependent shear moduli even for propagation *parallel* to the fractures. Because this fluid sensitivity will not occur for vertical rotationally invariant fractures or vertical fractures that induce orthorhombic symmetry, monitoring the changes of shear-wave velocities with saturation may help constrain the rheology of the fractures.

The second result obtained from the fluid substitution analysis indicates that the elastic parameterization of fractured rocks using linear slip theory (Schoenberg and Douma, 1988; Schoenberg and Muir, 1989; Schoenberg and Sayers, 1995), is not valid for rocks with large non-fracture porosity under conditions of equilibrated pore pressures. This result suggests that the best way of modeling the elastic properties of fractured rocks under conditions of equilibrated pore pressures is to calculate the dry compliances from the linear-slip theory and then use Brown and Korringa's (1975) theory to calculate the fluid-saturated values.

The fluid substitution analysis highlighted the influence the rock's *storage capacity* has on the magnitude of the changes with saturation of the rock's compliances. When stresses are applied to a fractured rock with a large storage capacity it can accommodate fluids displaced from the fractures with a small fluid pressure increase. Since, the fluid pressure increase is what stiffens the fractures, rocks with large storage capacities will be more compliant to applied stresses than rocks with small storage capacities.

The storage capacity is also a parameter that well test engineers estimate routinely from pressure-transient analysis. This link between the "geophysical" fluid substitution problem and the engineering data motivated the work presented on the integration of pressure-transient data into seismic reservoir characterization. The results suggest that the engineering estimates of the ratio of fracture storage to total rock storage, are related to the normal compliance of the fracture system, which is a parameter geophycisists try to estimate from seismic data. This quantitative link between the engineering and geophysical measurements provides a method to cross-validate the results obtained independently by the engineer and the geophycisist.

The Weyburn field case study provided the opportunity of applying some of the knowledge acquired from the fluid substitution study. The analysis of the azimuthal variation of the P-wave NMO and the analysis of the S-wave polarizations from the baseline survey, suggests that the reservoir in the survey area is divided into two main sections with different fracture properties. One section of the survey area has seismic signatures consistent with orthorhombic or HTI symmetry while the other section is consistent with a symmetry lower than orthorhombic. When this zonation is compared to the areas with the largest time-lapse anomalies on the shear-wave splitting, one observes that the time-lapse anomalies occur mostly in the areas where the symmetry is interpreted as lower than orthorhombic. This observation coincides with the expectations of the theory of fluid sensitive shear-waves developed in Chapter 4, in which the variation in shear splitting with saturation occurs for symmetries lower than orthorhombic when the fractures are vertical.

8.2 Recommendations

Avenues for further research can be derived from both the theoretical and applied aspects of the work presented in this thesis. In the paragraphs below suggestions are made for future work on testing the validity of the linear-slip parameterization, measuring the fluid sensitivity of shear-waves and improving the seismic characterization of Weyburn field.

8.2.1 Synthetic rock experiments

The magnitude of the errors the linear-slip parameterization incurs when predicting the compliance tensor of a fluid-saturated rock, has yet to be tested experimentally. One suggestion is to measure the *static* bulk compressibility of a fractured rock and compare it against the predictions of the linear-slip/Thomsen (1995) formulation and Brown and Korringa's (1975) theory. Because the bulk compressibility c_{sat} of a fluid-saturated fractured rock is derived from the compliance tensor as

$$c_{sat} = S^{sat}_{\alpha\alpha\beta\beta}, \tag{8.1}$$

different predictions of the compliance tensor will result in different predictions of the bulk compressibility.

Since it is difficult to determine the fracture parameters of natural rocks, the measurements suggested above are more convenient to conduct on synthetic rocks for which all the parameters are well known. Rathore et al. (1994) manufactured a synthetic sandstone with epoxy-cemented sand in which metallic discs of known shape were embedded in successive layers. The discs were then leached out chemically leaving cracks of known geometry and volume density that generated a rock with transversely isotropic symmetry. This type of synthetic rock is ideal to compare the predictions of the linear-slip/Thomsen (1995) formulation and Brown and Korringa's (1975) theory, because the dry rock parameters needed as input values for the fluid substitution calculations are better constrained than in naturally fractured rocks.

In order to test the shear-wave sensitivity to fluids the same technique used by Rathore et al. (1994) could be applied to build a monoclinic rock with two sets of non-orthogonal penny-shaped cracks. In this case the metal discs could be placed at a fixed angle in thin slabs of synthetic sandstone. Then the rock could be built by compressing several slabs together. Ultrasonic velocity measurements can be done for propagation parallel to the symmetry plane and out of the symmetry plane. Out-of-plane velocity measurements should give NMO ellipses whose orientation depend on saturation, whereas the velocity of the shear-waves propagating in the plane of symmetry should be fluid dependent.

8.2.2 Weyburn field seismic characterization

The analysis of the azimuthal variation of the S-wave normal moveout would be beneficial for the characterization of the elastic symmetry of the reservoir rocks and fracture network geometry at Weyburn field. The work presented in Chapter 7 indicated that the P-wave azimuthal NMO and the post-stack S-wave data were not enough to constrain the number of fracture sets in the southern section of the survey. Information about the fast azimuth of the S-wave NMO could help constrain the number of fracture sets and the rheology of the fractures.

The polarization analysis presented in Chapter 6 was done on S-wave data stacked with a single NMO velocity for all azimuths at each CDP. Jenner (2001) has shown that, in the presence of azimuthal anisotropy, stacking with a single "average" NMO velocity acts as a low-pass filter that degrades the character of the stacked volumes. Hence, the question arises if the polarization results will vary if azimuthal NMO corrections are applied to the data before stacking.

A possible way of assessing the influence of the azimuthal NMO analysis on the post-stack polarization angles is to proceed according to the following steps:

1. Obtain S-wave stacked volumes with an "average" NMO velocity for all azimuths.
2. Estimate polarization angles from the stacked volumes.

3. Apply polarization angles to the pre-stack gathers (now the gathers are oriented into local coordinate axes).
4. Perform azimuthal NMO analysis and stack data again.
5. Repeat estimation of polarization angles and compare with original estimates.

In the previous procedure, polarizations are estimated from post-stack volumes under the assumption that the estimates would be more stable after stack due to the larger signal to noise ratio.

With regards to the time-lapse analysis, the work presented on the time-lapse variations of the zero incidence reflectivity of the shear-waves, should be extended to a study of the AVO signatures at the top of the reservoir. Furthermore, the analysis presented in Chapter 7 has not included the potential attenuation effects that the fluid substitution process may have on the waves propagating through the reservoir. Duranti (2001) observed time-lapse variations in the frequency content of the multicomponent data acquired at Vacuum field, New Mexico, that could be related to changes in the attenuation due to the CO_2 injection process. Attenuation analyses performed below the reservoir zone at Weyburn field could aid in monitoring the movement of fluids in the reservoir.

REFERENCES

Alford, R., 1986, Shear data in the presence of azimuthal anisotropy: 56th Ann. Internat. Mtg., Soc. of Expl. Geophys., **53**, 476–479.

Bakulin, A., Grechka, V., and Tsvankin, I., 2000a, Estimation of fracture parameters from reflection seismic data – part i: Hti model due to a single fracture set: Geophysics, **65**, 1788–1802.

—, 2000b, Estimation of fracture parameters from reflection seismic data – part ii: Fractured models with orthorhombic symmetry: Geophysics, **65**, 1803–1817.

—, 2000c, Estimation of fracture parameters from reflection seismic data – part iii: Fractured models with monoclinic symmetry: Geophysics, **65**, 1818–1830.

Brown, J., and Korringa, J., 1975, On the dependence of the elastic properties of a porous rock on the compressibility of the pore fluid: Geophysics, **40**, 608–616.

Brown, L., 2002, Integration of Rock Physics and Reservoir Simulation for the Interpretation of Time-Lapse Seismic Data at Weyburn Field, Saskatchewan, Canada: CSM M.S. Thesis, CSM.

Bunge, R., 2000, Midale Reservoir Fracture Characterization Using Integrated Well and Seismic Data, Weyburn Field, Saskatchewan, Canada: CSM M.S. Thesis, CSM.

Da Prat, G., 1990, Well test analysis for fractured reservoir evaluation: Elsevier.

Duranti, L., 2001, Time-lapse, multicomponent seismic analysis of reservoir dynamics: CSM Ph.D. Thesis, CSM.

Duranti, L., Davis, T., and Benson, R., 2000, Time-lapse vertical seismic profile in vacuum field, new mexico: 70th Ann. Internat. Mtg, Soc. of Expl. Geophys., 1528–1531.

Gassmann, F., 1951, On the elasticity of porous media: Vier. der Natur. Gesllschft in Zurich, **96**, 1–23.

Grechka, V., Bakulin, A., and Tsvankin, I., 2001, Seismic characterization of vertical fractures described as general linear-slip interfaces: Center for Wave Phenomena Project Review, **CWP-384**, 79–92.

Grechka, V., Contreras, P., and Tsvankin, I., 2000, Inversion of normal moveout for monoclinic media: Geophys. Prosp., **48**, 577–602.

Grechka, V., and Tsvankin, I., 2001, Characterization of dipping fractures in transversely isotropic background: Center for Wave Phenomena Project Review, **CWP-384**, 93–102.

—, 2002, Seismic characterization of multiple fracture sets: Center for Wave Phenomena Project Review, **CWP-425**, 195–206.

Guest, S., van der Kolk, C., and Potters, H., 1998, The effect of fracture filling fluids on shear-wave propagation: 68th Ann. Internat. Mtg, Soc. of Expl. Geophys., 948–951.

Herawati, I., 2001, The use of time-lapse P-wave impedance inversion to monitor a CO2 flood at Weyburn field, Saskatchewan, Canada: CSM M.S Thesis, CSM.

Hudson, J., 1981, Wave speeds and attenuation of elastic waves in materials containing cracks: Geophys. J. Royal Astronom. Soc., **64**, 133–150.

Jenner, E., 2001, Azimuthal Anisotropy of 3-D Compressional Wave Seismic Data, Weyburn field, Saskatchewan, Canada: CSM Ph.D. Thesis, CSM.

Kachanov, M., 1992, Effective elastic properties of cracked solids: critical review of some basic concepts: Appl. Mech. Rev., **45**, 304–335.

Lee, J., 1982, Well testing: Society of Petroleum Engineers of AIME.

Mavko, G., Mukerji, T., and Dvorkin, J., 1999, The rock physics handbook: Cambridge University Press.

Mukerji, T., and Mavko, G., 1994, Pore fluid effects on seismic velocity in anisotropic rocks: Geophysics, **59**, 233–244.

Nakagawa, S., Nihei, K., and Myer, L., 1999, Shear-induced conversion of seismic waves across single fractures: Int. J. of Rock Mech. and Min. Sci., **00**, 1–16.

Nelson, R., 1985, Geologic Analysis of Naturally Fractured Reservoirs: Houston: Gulf Pub. Co.

O'Connell, R., and Budiansky, B., 1974, Seismic velocities in dry and saturated cracked solids: J. Geophys. Research, **79**, 4626–4627.

Raghavan, R., 1993, Well test analysis: Prentice Hall.

Rathore, J., Fjaer, E., Holt, R., and Renlie, L., 1994, P- and s-wave anisotropy of a shunthetic sandstone with controled crack geometry: Geophys. Prosp., **43**, 711–728.

Reasnor, M., 2001, Forward Modeling and Interpretation of Multicomponent Seismic Data for Fracture Characterization, Weyburn field, Saskatchewan, Canada: CSM M.S Thesis, CSM.

Sayers, C. M., 2002, Fluid-dependent shear-wave splitting in fractured media: Geophys. Prosp., **50**, 1–9.

Schoenberg, M., and Douma, J., 1988, Elastic-wave propagation in media with parallel fractures and aligned cracks: Geophys. Prosp., **36**, 571–590.

Schoenberg, M., and Muir, F., 1989, A calculus for finely layered anisotropic media: Geophysics, **54**, 581–589.

Schoenberg, M., and Sayers, C. M., 1995, Seismic anisotropy of fractured rock: Geophysics, **60**, 204–211.

Thomsen, L., 1988, Reflection seismology over azimuthally anisotropic media: Geophysics, **53**, 304–313.

—, 1995, Elastic anisotropy due to aligned cracks on porous rock: Geophys. Prosp., **43**, 805–829.

Thomsen, L., I., T., and Mueller, M. C., 1999, Coarse-layer stripping of vertically variable azimuthal anisotropy from shear-wave data: Geophysics, **64**, 1126–1138.

Tsvankin, I., 1997a, Anisotropic parameters and p-wave velocity for orthorhombic media: Geophysics, **62**, 1292–1309.

—, 1997b, Reflection moveout and parameter estimation for horizontal transverse isotropy: Geophysics, **62**, 614–629.

—, 2001, Seismic Signatures and Analysis of Reflection Data in Anisotropic Media: Pergamon.

Walsh, J., 1965, The effect of cracks on the compressibility of rocks: J. Geophys. Res., **70**, 381–389.

Zimmerman, R., 1991, Compressibility of Sandstones: Elsevier.

APPENDIX A

FLUID SUBSTITUTION IN THOMSEN'S MODEL

Appendix A of Thomsen's (1995) paper gives expressions for the elements of the compliance matrix of the fluid-saturated cracked rock for the case of aligned cracks with normals in the X_3 direction. If the cracks are vertical with normals in the X_1 direction, the crack-normal compliance element corresponds to S^s_{11} and the crack-tangential compliance element corresponds to $S^s_{55} = S^s_{66}$. Therefore, S^s_{11}, S^s_{55} and S^s_{66} are given by

$$S^s_{11} = \frac{1}{E_s} + \left(1 - \frac{K_f}{K_0}\right) \frac{A_c \eta_c}{K_d} D_{cp}, \tag{A.1}$$

and

$$S^s_{55} = S^s_{66} = \frac{1}{\mu} + \frac{B_c \eta_c}{\mu}, \tag{A.2}$$

where K_f, K_d and K_0 are the the bulk moduli of the fluid, dry isotropic background rock and mineral, respectively. E_s and μ are the Young's modulus and shear modulus of the saturated isotropic background rock, respectively, and η_c is the crack density. The constants A_c and B_c are

$$A_c = \frac{16}{9}\left(\frac{1 - \nu_d^2}{1 - 2\nu_d}\right), \tag{A.3}$$

and

$$B_c = \frac{16}{3}\left(\frac{1 - \nu_d}{2 - \nu_d}\right), \tag{A.4}$$

where ν_d is the Poisson's ratio of the dry isotropic background rock.

Since the second term in equations (A.1) and (A.2) are crack-dependent terms added to the background compliances $\frac{1}{E_s}$ and $\frac{1}{\mu}$, by definition they are the normal and tangential excess fracture compliances. Therefore, expressing K_d as a function of E_d and ν_d, and substituting it in equation (A.1) we obtain:

$$Z^s_N = Z^d_N \left(1 - \frac{K_f}{K_0}\right) D_{cp}, \tag{A.5}$$

and

$$Z^s_T = \frac{16}{3}\frac{1}{\mu_d}\left(\frac{1 - \nu_d}{2 - \nu_d}\right)\eta_c = Z^d_T, \tag{A.6}$$

where Z_N^d is the fracture compliance when $K_f = 0$ defined as:

$$Z_N^d = \frac{16}{3}\frac{1}{E_d}\left(1 - \nu_d^2\right)\eta_c. \tag{A.7}$$

APPENDIX B

THE ROLE OF STORAGE CAPACITY

The storage capacity can be defined from the equation of continuity for fluid flow in a porous medium. Due to mass conservation, the change in mass per unit time between the in-going flow and out-going flow has to be equal to the amount of fluid stored per unit time in the pores. This condition can be written as:

$$\nabla(\rho\vec{v}) = \frac{\partial(\rho\phi_t)}{\partial t}, \tag{B.1}$$

where ρ is the fluid density, $\vec{v}$ is the fluid flow velocity, and ϕ_t is the total porosity. Because fluid pressure variations are easier to monitor than fluid mass variations, the right side of equation (B.1) can be written as

$$\frac{\partial(\rho\phi_t)}{\partial t} = \rho\left[\frac{1}{\rho}\frac{\partial(\rho\phi_t)}{\partial p_f}\right]\frac{\partial p_f}{\partial t}, \tag{B.2}$$

where the term in the brackets is defined as the storage capacity of the rock. Evaluating the term in the brackets, it can be shown that

$$\frac{1}{\rho}\frac{\partial(\rho\phi_t)}{\partial p_f} = \phi_t\underbrace{(c_f + c_{pp})}_{c_t}, \tag{B.3}$$

where c_f is the fluid compressibility, c_t is the total pore system compressibility and c_{pp} is the pore space compressibility at a constant confining pressure defined as:

$$c_{pp} = \frac{1}{V_p}\left(\frac{\partial V_p}{\partial p_f}\right). \tag{B.4}$$

Zimmerman (1991) proved that

$$c_{pp} = \left(\frac{1}{\hat{K}_d} - \frac{1+\phi_t}{K_0}\right)\frac{1}{\phi_t}, \tag{B.5}$$

where $\frac{1}{\hat{K}_d}$ is the bulk compressibility of the dry rock (this applies to any monomineralic rock in which the mineral material is isotropic). In the case of the HTI symmetry rock it can be proven, using the dry compliance matrix (3.8) and the definition of

the bulk compressibility ($\frac{1}{\hat{K}_d} = S^d_{\alpha\alpha\beta\beta}$), that the bulk compressibility of the fractured rock is given by:

$$\frac{1}{\hat{K}_d} = Z^d_N + \frac{1}{K_d}, \tag{B.6}$$

where $\frac{1}{K_d}$ is the compressibility of the dry isotropic background. Substitution of equation (B.5) into equation (B.3) proves that the total storage capacity of the rock can be written as:

$$\phi_t c_t = \left(\frac{1}{\hat{K}_d} - \frac{1}{K_0}\right) + \left(\frac{1}{K_f} - \frac{1}{K_0}\right)\phi_t, \tag{B.7}$$

which is equal to the denominator on the right side of Brown and Korringa's equation (4.2).

Substituting equation (B.6) into equation (B.7) results in:

$$\phi_t c_t = \underbrace{\left(\frac{1}{K_d} - \frac{1}{K_0}\right) + \left(\frac{1}{K_f} - \frac{1}{K_0}\right)\phi_p}_{\equiv \phi_p c_p} +$$

$$\underbrace{Z^d_N + \left(\frac{1}{K_f} - \frac{1}{K_0}\right)\phi_c}_{\equiv \phi_c c_c}, \tag{B.8}$$

where the first term is the storage capacity of the isotropic background pores ($\phi_p c_p$) and the second term is the storage capacity of the crack pores ($\phi_c c_c$).

APPENDIX C

COMPLIANCE CHANGE WITH SATURATION

The change with saturation of the compliance matrix can be calculated from the B&K equation in two-index notation:

$$S^d_{IJ} - S^s_{IJ} = \frac{(\psi^d_I - \psi^0_I)(\psi^d_J - \psi^0_J)}{(C_d - C_0) + (C_f - C_0)\phi_t}. \tag{C.1}$$

Using the dry compliance matrix (3.8) of the fractured rock and the compliance matrix of the isotropic mineral material, the terms in the numerator of the right side of equation (C.1) are given by

$$(\psi^d_1 - \psi^0_1) = Z^d_N + \frac{1}{3}\left(\frac{1}{K_d} - \frac{1}{K_0}\right), \tag{C.2}$$

$$(\psi^d_2 - \psi^0_2) = (\psi^d_3 - \psi^0_3) = \frac{1}{3}\left(\frac{1}{K_d} - \frac{1}{K_0}\right), \tag{C.3}$$

and

$$(\psi^d_4 - \psi^0_4) = (\psi^d_5 - \psi^0_5) = (\psi^d_6 - \psi^0_6) = 0, \tag{C.4}$$

where the elements ψ_I's are defined in the main text. From equations (C.2)-(C.4) it is clear that the only compliance elements that will change with saturation are S^s_{11}, $S^s_{22} = S^s_{33}$, $S^s_{12} = S^s_{13}$, and S^s_{23}.

From equations (C.2)-(C.4) and noting that the denominator on the right side of equation (C.1) is the total storage capacity of the rock (Appendix B), the saturated compliances can be written as

$$S^s_{11} = \underbrace{\frac{1}{E_d} - \frac{\frac{1}{9}\left(\frac{\phi_p}{K_{\phi_p}}\right)^2}{\phi_t C_t}} + \frac{\left(1 - \frac{K_f}{K_0} + \frac{K_f}{3K_{\phi_p}}\frac{\phi_p}{\phi_t}\right) Z^d_N}{\frac{K_f}{\phi_t}(\phi_t C_t)}, \tag{C.5}$$

$$S^s_{22} = S^s_{33} = \underbrace{\frac{1}{E_d} - \frac{\frac{1}{9}\left(\frac{\phi_p}{K_{\phi_p}}\right)^2}{\phi_t C_t}}, \tag{C.6}$$

$$S^s_{12} = S^s_{13} = \underbrace{-\frac{\nu_d}{E_d} - \frac{\frac{1}{9}\left(\frac{\phi_p}{K_{\phi_p}}\right)^2}{\phi_t C_t}} - \frac{\frac{K_f}{3K_{\phi_p}}\frac{\phi_p}{\phi_t}Z^d_N}{\frac{K_f}{\phi_t}(\phi_t C_t)}, \tag{C.7}$$

$$S^s_{23} = \underbrace{-\frac{\nu_d}{E_d} - \frac{\frac{1}{9}\left(\frac{\phi_p}{K_{\phi_p}}\right)^2}{\phi_t C_t}}. \tag{C.8}$$

Here $\frac{1}{K_{\phi_p}}$ is the compaction compressibility of the isotropic background pores that relates the dry isotropic compressibility and the mineral compressibility according to

$$\frac{1}{K_{\phi_p}} = \frac{1}{\phi_p}\left(\frac{1}{K_d} - \frac{1}{K_0}\right). \tag{C.9}$$

From equations (C.5)-(C.8) it can be seen that if the rock has no isotropic porosity ($\phi_p = 0$), then S^s_{22}, S^s_{33}, S^s_{12}, S^s_{13}, S^s_{23} will take the value of the isotropic background mineral and only S^s_{11} will change with saturation. In this case B&K's equations are *identical* to Thomsen's (1995) formulation, as explained in the main text.

When the storage capacity of the cracks is negligible, the total storage capacity is approximately equal to the storage capacity of the isotropic background pores, i.e. $\phi_t C_t \approx \phi_p C_p$. Under this approximation, the terms marked underneath in equations (C.5) and (C.6) are approximately equal to $\frac{1}{E_s}$, and the terms in equations (C.7) and (C.8) are approximately equal to $-\frac{\nu_s}{E_s}$. This results from the application of B&K's theory to a dry isotropic rock in which $\frac{1}{E_d}$ and $-\frac{\nu_d}{E_d}$ vary with saturation as

$$\frac{1}{E_s} = \frac{1}{E_d} - \frac{\frac{1}{9}\left(\frac{\phi_p}{K_{\phi_p}}\right)^2}{\phi_p C_p}, \tag{C.10}$$

and

$$-\frac{\nu_s}{E_s} = -\frac{\nu_d}{E_d} - \frac{\frac{1}{9}\left(\frac{\phi_p}{K_{\phi_p}}\right)^2}{\phi_p C_p}. \tag{C.11}$$

Therefore, in the approximation of negligible crack storage capacity, the compliance of the saturated fractured rock can be written as the sum of a background isotropic compliance and an excess fracture compliance. However, due to the extra fracture term in the S^s_{12} and S^s_{13} elements, the saturated compliance predicted by B&K's theory is not *analytically* identical to Thomsen's (1995) formulation

APPENDIX D

FLUID SENSITIVITY OF Z_V AND Z_{NV}

The compliance of the rock with one system of dry micro-corrugated fractures can be written as the sum of the background isotropic rock compliance and the excess fracture system compliance matrix:

$$S_{rock} = \begin{pmatrix} Z_N + \frac{1}{E} & -\frac{\nu}{E} & -\frac{\nu}{E} & 0 & Z_{NV} & 0 \\ -\frac{\nu}{E} & \frac{1}{E} & -\frac{\nu}{E} & 0 & 0 & 0 \\ -\frac{\nu}{E} & -\frac{\nu}{E} & \frac{1}{E} & 0 & 0 & 0 \\ 0 & 0 & 0 & \frac{1}{G} & 0 & 0 \\ Z_{NV} & 0 & 0 & 0 & Z_V + \frac{1}{G} & 0 \\ 0 & 0 & 0 & 0 & 0 & Z_H + \frac{1}{G} \end{pmatrix}, \tag{D.1}$$

where E, G and ν are the Young's modulus, shear modulus and Poisson's ratio of the background rock, respectively. Z_N is the normal fracture compliance, Z_V and Z_H are tangential compliances, and Z_{NV} is the compliance element responsible for the normal-to-vertical coupling.

In Chapter 3 it was proven that the linear slip decomposition of the compliance matrix (D.1) was not always applicable to fluid saturated rocks under conditions of equilibrated pore pressures. However, for low values of the isotropic porosity the form (D.1) is approximately equivalent to the formal prediction by Brown and Korringa. Therefore, assuming that the fluid-saturated rock has a compliance matrix of the same form as (D.1) it is easy to see that the difference between the values of S_{15} for the dry and saturated rock is:

$$S_{15}^d - S_{15}^s = \frac{(\psi_1^d - \psi_1^m)(\psi_5^d - \psi_5^m)}{(c_d - c_m) + (c_f - c_m)\phi_t}, \tag{D.2}$$

where ψ_1 and ψ_5 are defined in equation (4.2).

From the compliance matrix (D.1) it is clear that $\psi_5^d = Z_{NV}^d$ and $\psi_1^d - \psi_1^m = Z_N^d + \frac{1}{3}(\frac{1}{K_d} - \frac{1}{K_m})$, where K_d and K_m are the background dry-rock and mineral bulk moduli. Since the mineral material is assumed to be isotropic, $\psi_5^m = 0$. Finally, since the fracture compliances are added to the background isotropic compliance, the difference between the dry and mineral compressibility is $c_d - c_m = Z_N^d + (\frac{1}{K_f} - \frac{1}{K_m})$, where K_f is the fluid bulk modulus. From these relations and equation (D.2) we find

the difference between the dry and saturated values of the compliance term Z_{NV}:

$$Z^d_{NV} - Z^s_{NV} = \frac{\{Z^d_N + \frac{1}{3}(\frac{1}{K_d} - \frac{1}{K_m})\} Z^d_{NV}}{Z^d_N + (\frac{1}{K_d} - \frac{1}{K_m}) + (\frac{1}{K_f} - \frac{1}{K_m})(\phi_c + \phi_i)}, \tag{D.3}$$

where the total porosity (ϕ_t) of the rock is written as the sum of the "crack" and "isotropic" porosities $\phi_t = \phi_c + \phi_i$.

The difference between the dry compressibility ($\frac{1}{K_d}$) of the background rock and the compressibility of the mineral ($\frac{1}{K_m}$) can be written as Mavko et al. (1999):

$$\frac{1}{K_d} - \frac{1}{K_m} = \frac{\phi_i}{K_{\phi_i}}, \tag{D.4}$$

where $1/K_{\phi_i}$ is the isotropic pore space compressibility. If the isotropic pore space can be modeled as a dilute collection of spherical pores ($\phi_i < 0.1$),

$$\frac{1}{K_{\phi_i}} = \frac{1}{K_m} \frac{3(1-\nu)}{2(1-2\nu)} \equiv \frac{F_m}{K_m}. \tag{D.5}$$

Substituting equations (D.4) and (D.5) into equation (D.3), we obtain the change with saturation of the compliance Z_{NV} for a fractured rock with an isotropic background composed of a dilute collection of spherical pores:

$$Z^d_{NV} - Z^s_{NV} = Z^d_{NV} \frac{1 + \frac{1}{3}\frac{F_m}{K_m}\{\frac{\phi_i}{Z^d_N}\}}{1 + \frac{F_m}{K_m}\{\frac{\phi_i}{Z^d_N}\} + (\frac{1}{K_f} - \frac{1}{K_m})\{\frac{\phi_c + \phi_i}{Z^d_N}\}}. \tag{D.6}$$

In a similar way change in the compliance Z_V with saturation is calculated by solving for the S_{55} component in Brown and Korringa's equation (4.2). For a background rock composed of spherical pores,

$$Z^d_V - Z^s_V = \frac{{Z^d_{NV}}^2}{Z^d_N} \frac{1}{1 + \frac{F_m}{K_m}\{\frac{\phi_i}{Z^d_N}\} + (\frac{1}{K_f} - \frac{1}{K_m})\{\frac{\phi_c + \phi_i}{Z^d_N}\}}. \tag{D.7}$$

Note that in the limit in which $\phi_i \to 0$, equations (D.6) and (D.7) become:

$$Z^d_{NV} - Z^s_{NV} = Z^d_{NV} \frac{1}{1 + \frac{(\frac{1}{K_f} - \frac{1}{K_m})\phi_c}{Z^d_N}}, \tag{D.8}$$

and

$$Z_V^d - Z_V^s = \frac{{Z_{NV}^d}^2}{Z_N^d} \frac{1}{1 + \frac{(\frac{1}{K_f} - \frac{1}{K_m})\phi_c}{Z_N^d}}. \tag{D.9}$$

Since the fluid compressibility is much larger than the mineral compressibility, in this limit the change with saturation is largely dependent on the value of $\frac{\phi_c}{K_f Z_N^d}$. If this combination of parameters is small, changes in Z_N are large.

APPENDIX E

Z_N FOR NEGLIGIBLE POROSITY

For two sets of non-orthogonal fractures in an isotropic, porous background, the rotation angles of the NMO ellipses are a function of the normal fracture compliance (Z_N) of each fracture set. If the changes in Z_N with saturation are large then the NMO ellipses' rotation angles are strongly dependent on saturation as well. Here, we prove that in the limit of vanishing background "isotropic" porosity (ϕ_i), the parameter $\frac{\phi_c}{K_f Z_N^d}$ determines how significantly Z_N changes with saturation (ϕ_c is the crack porosity and K_f is the fluid's bulk modulus).

According to equation (4.2), the difference between the values of the component S_{11} for the dry and saturated rocks is:

$$S_{11}^d - S_{11}^s = \frac{(\psi_1^d - \psi_1^m)^2}{(c_d - c_m) + (c_f - c_m)\phi_t}, \tag{E.1}$$

Since the fracture compliances are added to the isotropic background compliance, $\psi_1^d - \psi_1^m = Z_N^d + \frac{1}{3}(\frac{1}{K_d} - \frac{1}{K_m})$, where K_d and K_m are the background dry rock and mineral moduli. Similarly, the difference between the dry and mineral compressibility is $c_d - c_m = Z_N^d + (\frac{1}{K_f} - \frac{1}{K_m})$. Using these relations and noting that $S_{11} = Z_N + \frac{1}{9K}$, where K is the bulk modulus of the background rock, equation (E.1) can be represented as:

$$Z_N^d - Z_N^s = \frac{\{Z_N^d + \frac{1}{3}(\frac{1}{K_d} - \frac{1}{K_m})\}^2}{Z_N^d + (\frac{1}{K_d} - \frac{1}{K_m}) + (\frac{1}{K_f} - \frac{1}{K_m})(\phi_c + \phi_i)} - \frac{1}{9}\{\frac{1}{K_d} - \frac{1}{K_s}\}, \tag{E.2}$$

where the total porosity is expressed as the sum of background "isotropic" porosity (ϕ_i) and fracture porosity (ϕ_c).

When the "isotropic" porosity of the background rock ϕ_i approaches zero, the compressibility of the dry background rock approaches the compressibility of the mineral ($\{\frac{1}{K_d} - \frac{1}{K_m}\} \to 0$). Also, since $\phi_i \to 0$, there is no difference between the dry and saturated background compressibility ($\{\frac{1}{K_d} - \frac{1}{K_s}\} \to 0$). Therefore, in the limit $\phi_i \to 0$, equation (E.2) becomes

$$\frac{Z_N^d - Z_N^s}{Z_N^d} = \frac{1}{1 + \frac{(\frac{1}{K_f} - \frac{1}{K_m})\phi_c}{Z_N^d}}. \tag{E.3}$$

Since for most fluids $\frac{1}{K_f} \gg \frac{1}{K_m}$, in this limit the magnitude of change in Z_N is determined by $\frac{\phi_c}{K_f Z_N^d}$. If this combination of parameters is small, changes in Z_N are large.

APPENDIX F

STORAGE CAPACITY IN THE ISP ROCK

The solution to equation (5.1) will depend on the inner and outer boundary conditions of the system. If the pressure disturbance does not reach the reservoir boundaries during the time used for data analysis, the outer boundary condition corresponds to an infinite reservoir (transient flow solution). The inner boundary condition depends on the borehole damage or skin effect, and borehole storage. The skin effect reflects a small region around the wellbore with altered permeability values due to damage done during drilling and completion. The borehole storage effect results from fluids that are stored in the wellbore volume and are produced before the formation fluids at the beginning of the well test Raghavan (1993).

The late-time response of the infinite reservoir solution to equation (5.1) is

$$p_D(t_D) = \frac{1}{2} ln \left(\frac{4t_D}{e^{\gamma}} \right) + S, \tag{F.1}$$

where S is the skin factor, γ is Euler's number and p_D and t_D are dimensionless pressure and time, defined as

$$p_D = \frac{2\pi\kappa_I h}{q\mu} \Delta p,$$

$$t_D = \frac{\kappa_I}{\phi_I c_{TI} \mu r_w^2} \Delta t, \tag{F.2}$$

where r_w is the wellbore radius, h is the formation thickness and Δp and Δt are the measured pressure change and time.

From equation (F.1), the combination of parameters $\phi_i c_i h$ and $\kappa_i h$ can be inverted from the data through a type curve-matching procedure Lee (1982). If the thickness of the producing interval is known, the reservoir storage capacity ($\phi_i c_i$) and reservoir permeability (κ_i) are obtained.

APPENDIX G

PRESSURE ANALYSIS IN THE ADP ROCK

The differential equations (5.14) and (5.15) are solved in Laplace space after defining dimensionless pressures and times as in equations (F.2) (Da Prat, 1990). The pressure response of the double-porosity rock presents three regimes: early, transitional and late, which are shown in Figure G.1. In the early period the pressure solution is

$$P(t)_{early} = \frac{q\mu^{1/2}}{hr_w\kappa_f^{1/2}\pi^{3/2}}\sqrt{\frac{t}{\phi_f c_f}}, \tag{G.1}$$

where q is the flow rate, μ is the fluid viscosity, h is the formation thickens and r_w is the wellbore radius. Note that at early times the pressure response is dominated by the fracture storage capacity which means that the fracture system does not "sense" the presence of the isotropic porosity. In the late period the pressure solution is

$$P(t)_{late} = \frac{q\mu}{4\pi hr_w\kappa_f} ln\left(\frac{4\kappa_f t}{\mu r_w^2(\phi_f c_f + \phi_i c_i)}\right) - \gamma, \tag{G.2}$$

where γ is Euler's number. In the late-time period the response is identical to that of a single-porosity rock with a storage capacity equal to $(\phi_f c_f + \phi_i c_i)$, which means that the fracture system "senses" the presence of the isotropic porosity.

The transition between the fracture and total rock system regimes is determined by the parameter λ defined as

$$\lambda = \frac{\kappa_i}{\kappa_f}\frac{r_w^2}{L}, \tag{G.3}$$

where L is the characteristic length of an isotropic rock block. If the permeability of the isotropic pores is small, the transition will occur later because it will take longer to transfer fluids from the low-permeability isotropic rock into the fracture system.

The value of the ω parameter is always between zero and one. If the rock has no isotropic porosity (e.g. anisotropic, fractured granite), $\omega = 1$ and the pressure response will be identical to that of a single porosity rock at all times. If ω is small but non-zero, the λ parameter determines at which time the pressure response converges to the single porosity limit (see Figure G.1). If the rock has no fracture porosity

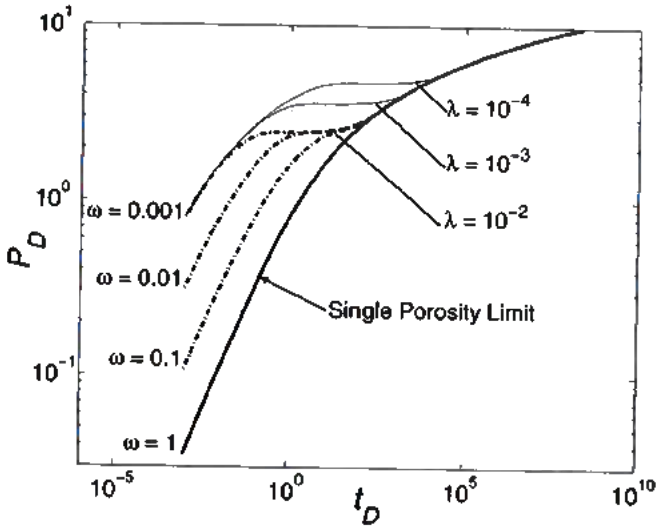

FIG. G.1. Double porosity pressure response indicating the three regimes and the influence of λ in determining the transition between the early and late periods.

(e.g. unfractured, tight carbonate) $\omega = 0$. In this limit, the rock model becomes impermeable because of the lack of fractures, and no pressure drop occurs.

APPENDIX H

ω AND THE ROCK COMPRESSIBILITY

To find an equation that relates ω to the normal fracture compressibility (Z_{Nf}) it is necessary to expand the numerator and denominator of equation (5.13). The denominator is the total rock-storage capacity, which can be written as

$$(\phi_f c_f + \phi_i c_i) = \phi_T \left(\frac{1}{K_F} + c_{pp,(i+f)} \right), \tag{H.1}$$

where $\phi_T = \phi_i + \phi_f$ and $c_{pp,(i+f)}$ is the total pore space compressibility defined in equation (5.6), which includes fracture pores and isotropic pores. Note that the only difference between the compressibility defined for the single porosity rock ($c_{pp,i}$) and $c_{pp,(i+f)}$ is that the latter must take into account the fracture pores.

From the relations between compressibilities presented in chapter 2, $c_{pp,(i+f)}$ can be expressed as a function of the dry rock compressibility, mineral compressibility, and total porosity as

$$c_{pp,(i+f)} = \left(\frac{1}{K_{d,(i+f)}} - \frac{1+\phi_T}{K_m} \right) \frac{1}{\phi_T}, \tag{H.2}$$

which is similar to equation (B.5) except that $K_{d,(i+f)}$ is the dry bulk modulus of a fractured, anisotropic rock.

Substituting (H.2) into (H.1), the denominator of the ω parameter is

$$(\phi_f c_f + \phi_i c_i) =$$

$$\left(\frac{1}{K_F} - \frac{1}{K_m} \right) \phi_T + \left(\frac{1}{K_{d,(i+f)}} - \frac{1}{K_m} \right). \tag{H.3}$$

Since the isotropic pores of the **ADP** model are identical to the pores in the **ISP** rock, equation (5.8) can be substituted into equation (H.3) to solve for $\phi_f c_f$ as

$$\phi_f c_f = \left(\frac{1}{K_F} - \frac{1}{K_m} \right) \phi_f + \left(\frac{1}{K_{d,(i+f)}} - \frac{1}{K_{d,i}} \right). \tag{H.4}$$

Finally, from equations (H.3) and (H.4) we can write the ω parameter as

$$\omega = \frac{\left(\frac{1}{K_F} - \frac{1}{K_m}\right)\phi_f + \left(\frac{1}{K_{d,(i+f)}} - \frac{1}{K_{d,i}}\right)}{\left(\frac{1}{K_F} - \frac{1}{K_m}\right)\phi_T + \left(\frac{1}{K_{d,(i+f)}} - \frac{1}{K_m}\right)}. \tag{H.5}$$

APPENDIX I

RAW SHEAR SPLITTING MAPS

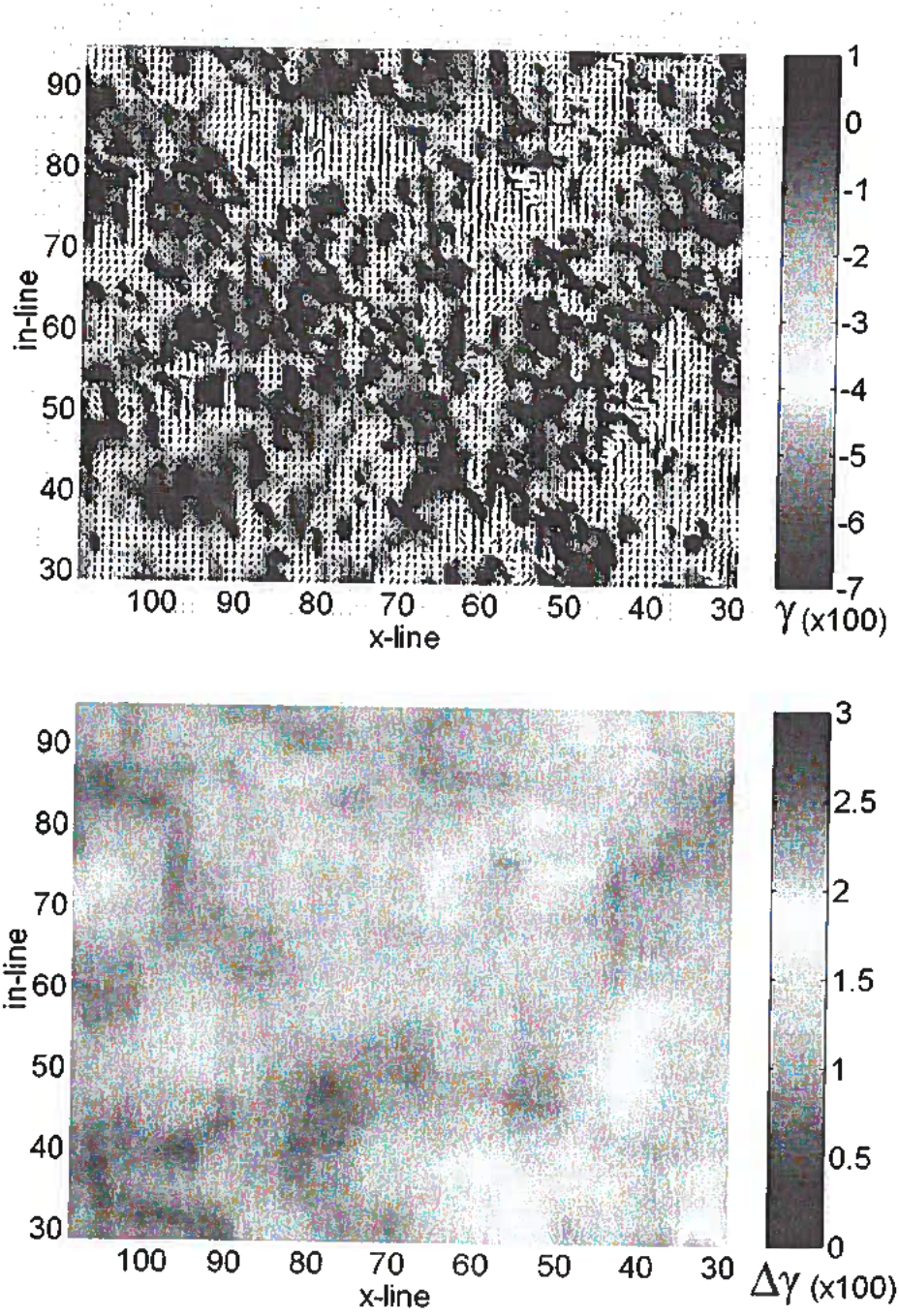

FIG. I.1. Top: "raw" shear-splitting map from travel-times for the baseline survey. Bottom: standard deviation calculated from overlaping bins of 9 x-lines by 9 in-lines.

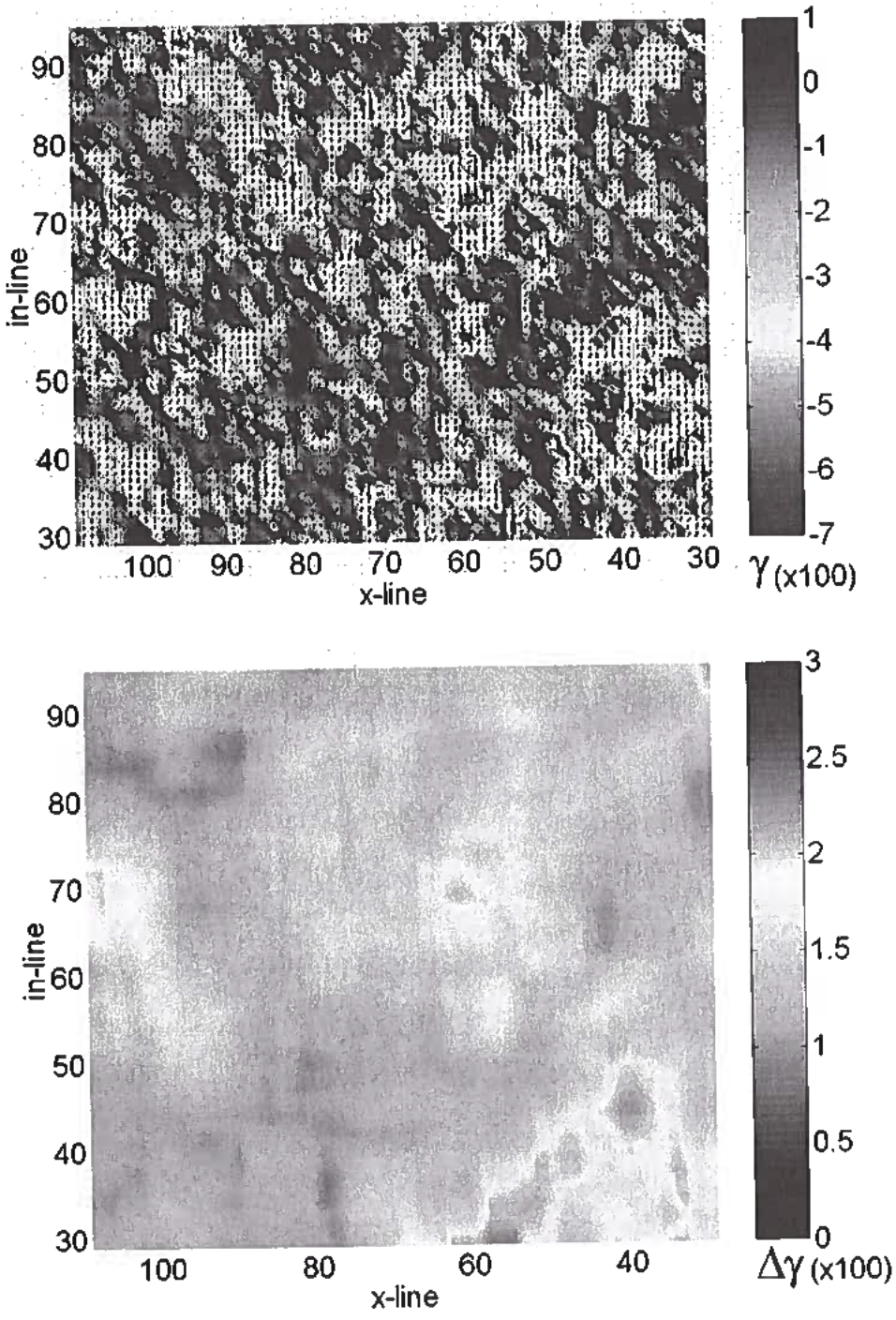

FIG. I.2. Top: "raw" shear-splitting map from travel-times for the repeat survey. Bottom: standard deviation calculated from overlaping bins of 9 x-lines by 9 in-lines.

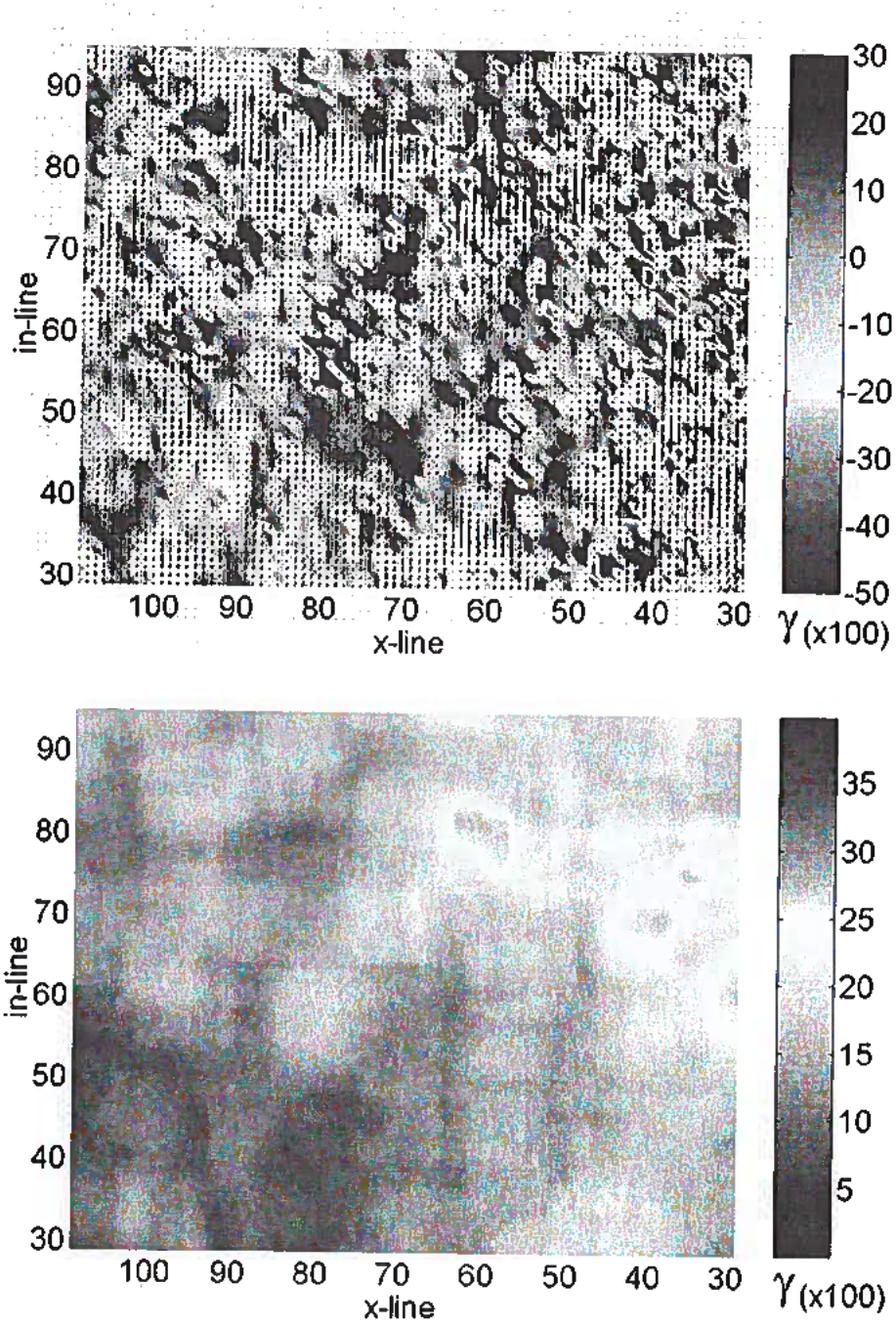

FIG. I.3. Top: "raw" shear-splitting map from amplitudes for the baseline survey. Bottom: standard deviation calculated from overlaping bins of 9 x-lines by 9 in-lines.

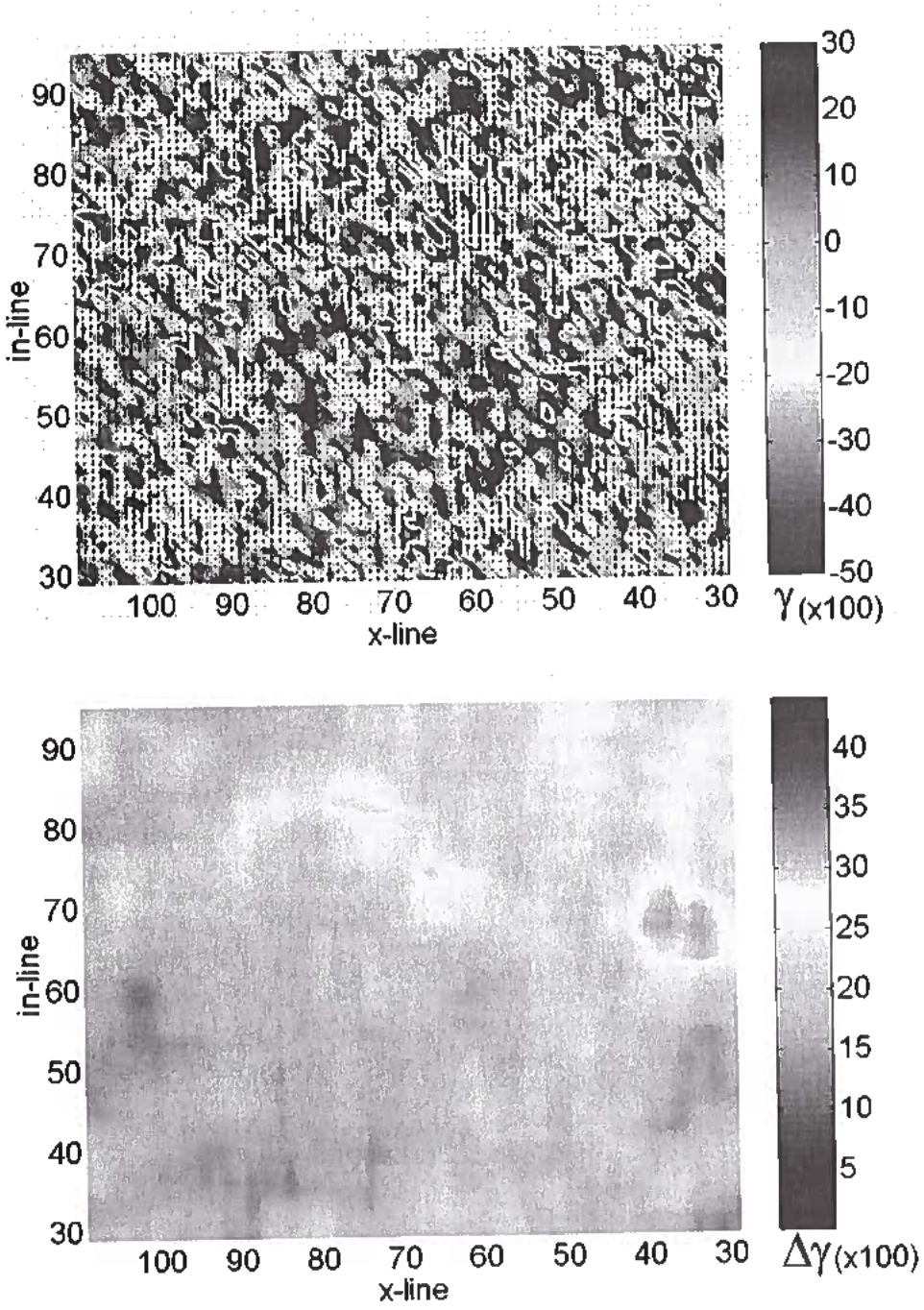

FIG. I.4. Top: "raw" shear-splitting map from amplitudes for the repeat survey. Bottom: standard deviation calculated from overlaping bins of 9 x-lines by 9 in-lines.